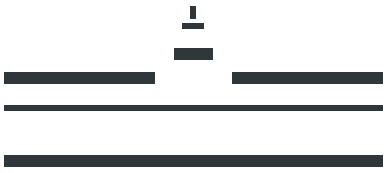

Westfälische
Wilhelms-Universität
Münster

>Patient Specific Multiscale Modelling of Glioma Growth.

Markus Knappitsch

- 2014 -

wissen.leben
WWUMünster

Angewandte
Mathematik
Münster

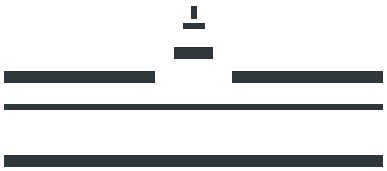

Westfälische
Wilhelms-Universität
Münster

Fach: Mathematik

Patient Specific Multiscale Modelling of Glioma Growth.

Inaugural Dissertation

zur Erlangung des Doktorgrades der Naturwissenschaften

– Dr. rer. nat. –

im Fachbereich Mathematik und Informatik

der Mathematisch-Naturwissenschaftlichen Fakultät

der Westfälischen Wilhelms-Universität Münster

eingereicht von

Markus Knappitsch

aus Herne

– 2014 –

Dekan:	Prof. Dr. Martin Stein
Erste Gutachterin:	Prof. Dr. Christina Surulescu (Technische Universität Kaiserslautern)
Zweiter Gutachter:	Prof. Dr. Christian Engwer (Universität Münster)
Tag der mündlichen Prüfung:	21.05.2014
Tag der Promotion:	21.05.2014

Contents

Abstract

Gliomas are rarely curable brain tumors arising from abnormal glial cells in the human brain which usually have a poor prognosis with a median survival rate that is less than one year. Complex therapy approaches including surgical resection of cancerous tissue, radio- and chemotherapy can still not ensure a complete healing of the patient and are part of ongoing research.

Modern methods as *diffusion tensor imaging* (DTI) are the preferred radiological diagnostic instruments and allow also to reveal the specific architecture of a human brain in a noninvasive way. Particulary for surgical treatment this is valuable information. The physical basis of modern imaging methods is the diffusion behaviour of water molecules within structured tissue. Water molecules diffuse faster along fibre tracts than perpendicular to them. The anisotropy of water diffusion is hence related to the anisotropy of neural tissue, especially brain white matter. Technically, DTI measures the spatial diffusion of water molecules by MRI per volume element (voxel). This leads to a symmetric diffusion tensor for each voxel, containing the full (apparent) diffusion information along six directions. Detailed knowledge of the tissue structure can be used for mesoscopic modelling of cellular movement. This leads to kinetic partial differential equations, which provide an appropriate framework for a motion description directly on the cell scale. Hence, it is possible to include patient specific DTI data into a class of multiscale models for glioma growth.

This thesis focuses on multiscale modelling of glioma growth in the human brain as well as on usage of DTI data for patient specific simulations. Starting point on the microscale is a differential equation for the binding dynamics of cell surface receptors to the underlying tissue network, which is coupled to a kinetic transport equation for the cell density on the mesoscale. Scaling techniques for the kinetic equation lead to approximating macroscopic partial differential equations of advection-diffusion type, where the coefficients contain the information from the mesoscale. The binding dynamics on the microscale leads to a haptotactic transport term on the macroscale. Numerical simulations show that haptotactic transport is responsible for the emergence of anisotropic, fingerlike spread patterns of the tumor. The modelling of proliferative effects on the mesoscale is based on transport equations with resting phases, which corresponds to the go-or-grow hypothesis, which states that cells can either move or proliferate. The corresponding macroscopic approximating equations are of advection-diffusion-reaction type, and again the coefficients contain the tissue information from the mesoscale.

Curriculum vitae

Personal information

Birth	29.07.1984, Herne (NRW)
Nationality	German
Family status	Married

Education

2011-2014	Ph.D. student, Institute for Numerical and Applied Mathematics, University of Münster
2005 - 2011	Studies in mathematics, philosophy and biology, University of Bonn
2004	Abitur, Hans-Thomas Gymnasium, Neustadt (Schw.)

Experience

2011-2014	Research assistant, Institute for Numerical and Applied Mathematics, University of Münster
2010-2011	Student research assistant, Institute for cellular and molecular botanics, University of Bonn
2006-2010	Student assistant, Mathematical Institute, University of Bonn
2004-2005	Civilian service, Lenzkirch (Schw.)

Part I.

Introduction

1. Introduction

τὰ πάντα ῥεῖ. (Everything flows.)

(Heraclitus of Ephesus)

Contents

1.1. Introduction

Mathematical modelling can help to understand our complex environment and may give insight into processes which are not accessible to our human sensorium. During the last decades particularly the emerging field of mathematical biology enhanced our perception of biological processes and systems with the aid of sophisticated mathematical models. Especially on the molecular level modelling and simulation tools can help to understand the complex reality and to test explanatory hypotheses, despite all difficulties in classical experiments. The interdisciplinary field of mathematical biology aims to combine methods from different sciences as mathematics, biology, medicine, physics and informatics to push forward human knowledge.

The term cancer summarizes a large group of diseases, which have in common that they are complex phenomenona involving endless biochemical and biophysical processes and subsystems. Even nowadays, our understanding of these diseases is still very limited. Mathematical cancer modelling aims to use the above mentioned interdisciplinary approach and tries to bring together equations from mathematics, experiments from biology and insights from clinical practice in medicine to shed light on cancer diseases.

In this thesis I will focus on a specific type of cancer, namely neoplasms within the brain called *gliomas*. Gliomas are primary tumors within the brain and originate typically from the mutation of glia cells (Ware et al., 2003) and usually have a poor prognosis (more than 97% of *glioblastoma multiforme* patiens die within 5 years after diagnosis (Ohgaki and Kleihues, 2005)). Despite a long history of research these tumors are still not certainly curable. At present the three major treatment approaches are surgery, radiotherapy and chemotherapy, which are usually combined in a long-term treatment

Figure 1.1.: Painting by Hieronymus Bosch depicting trepanation (c.1488-1516)

(Wang and Jiang, 2013).

One of the first documented and successfully performed surgical resections of a brain tumor goes back to William Macewen, who performed a brain tumor removal in 1879 in a young woman (Preul, 2005) by craniotomy. While the history of brain surgery goes back up to the late middle ages (see the painting by the dutch artist Hieronymos Bosch, figure 1.1[1]) or even to neolithic, only nowadays modern imaging techniques enable reliable diagnosis. In this thesis I will focus on a magnetic resonance imaging based method called**D***iffusion* **T***ensor* **I***maging* (DTI) (Hagman et al., 2006; Descoteaux, 2008), which gives information about the diffusion behavior of water molecules in biological tissue. T1 pictures, obtained from DTI which provides information about the tissue density but also allows to detect malignant tissue alterations by the 'eye-norm'. Figure 1.2(a) shows such a T1 weighted picture for a horizontal slice of a male student's brain. The bright areas correspond to white matter, surrounding grey areas to grey matter (indeed, the terms *grey* and *white* matter are due to their intensities on such medical images).

[1]source: http://upload.wikimedia.org/wikipedia/commons/5/55/Hieronymus_Bosch_053_detail.jpg

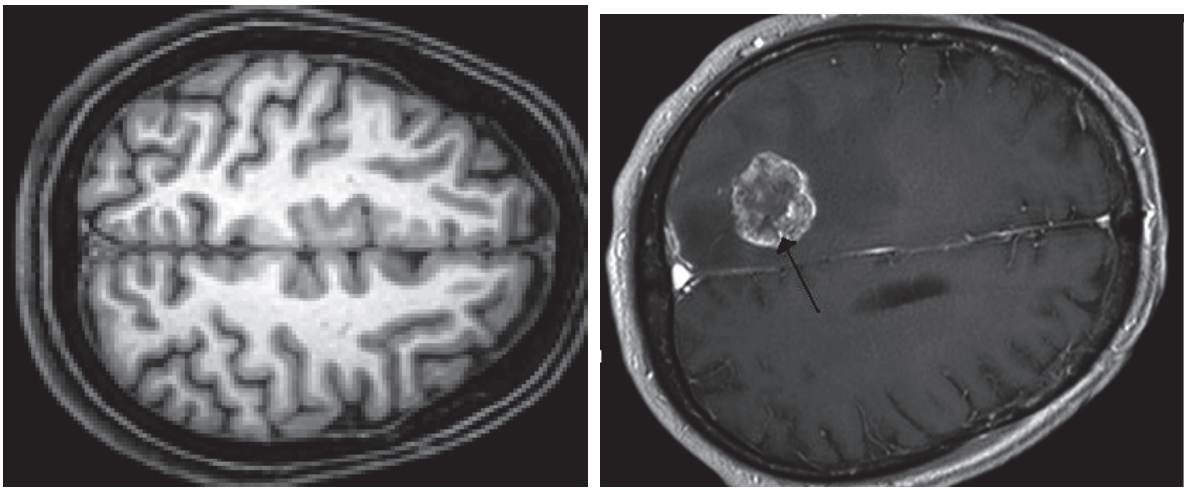

(a) T1 weighted picture showing a horizontal slice of a human male's brain.

(b) CT scan showing a neoplasm within human brain.

Figure 1.2.: T1 weighted pictures in medical diagnosis.

The dark domains inside the scull are mostly *cerebrospinal fluid*, which acts as a buffer for the brain and provides mechanical protection. Figure 1.2(b)[2] shows a CT scan of a brain tumor which altered the tissue structure and is hence detectable by its high intensity. Moreover, diffusion tensor imaging can provide detailed information about the local tissue structure. This will be a key point in the subsequent modelling. I will come back to this point in chapter 3.

Besides an early detection, reliable treatment strategies for brain tumors are of high importance for the patient. As already mentioned, surgical removal plays a key role. Despite the usage of both medical imaging and chemical markers allowing a visual identification of cancerous tissue during surgery, the exact borderline between cancerous and healthy tissue is hard to detect due to the invasive character of cancer cells. However, detailed knowledge of the exact shape, extension and position of a tumor and its boundary would be a great benefit in surgery planning. Personalized mathematical models can provide complementary information about the spatiotemporal evolution of the tumor, but embedding patient specific information into such models is not a trivial task and still part of intensive research.

Recently, multiscale approaches for the modelling of cancer attracted more and more interest (Deisboeck and Stamatakos, 2010; Lowengrub., 2010). Since tumor progression is highly complex and involves processes on multiple temporal and spatial scales it is desirable to reflect this complexity also in modelling. From a philosophical point of view a *bottom up* approach is desirable, where, starting from simple biophysical principles, mathematical linkage of the scales carries information from one level of description to

[2]source: http://upload.wikimedia.org/wikipedia/commons/5/5f/Hirnmetastase_MRT-T1_KM.jpg

the next. Typically, three levels called *micro-*, *meso-* and *macroscale* are involved, but the terminology is not uniform in the literature and differs from model to model. In this thesis, we will assign processes happening on the subcellular spatial scale as *microscopic*, processes on the scale of single cells as *mesoscopic* and processes on the population level as *macroscopic*.

Starting point on the microscale will be a simple model for the binding of cell surface receptors. Moving cells have to attach to fibres or other cells to generate mechanical forces. Transmembrane adhesion molecules as, for instance, integrins and cadherins, connect the cellular actin cytoskeleton to components in the extracellular matrix and to other cells to generate these forces. For more information see section 2.4, wich is concerned with the molecular mechanisms of glioma invasion.

An appropriate tool for the description of cellular motion on the mesoscale are kinetic transport equations. Starting with a seminal work by Wolfgang Alt in 1980 (Alt, 1980), kinetic models have been studied for now more than three decades. A basic assumptions for this description is, that small particles move on straight lines, then stop their movement, reorientate and choose a new direction, then continue their movement. Velocity changes are modelled by a *turning operator* describing how cells with velocity $\mathbf{v}'$ switch to another velocity $\mathbf{v}$. However, these results apply to the special case of bacterial chemotaxis, and there is noattachment to a fibrous structure or to other particles. In chapter 4 we will present some basic modelling aspects of kinetic equations.

An interesting point in multiscale modelling in general is the question, how processes happening on the microscale affect the system's behaviour on the macroscale. As a first step, classical kinetic models have been extended by an additional drift term with respect to variables on the microscale. Under appropriate mathematical conditions one can derive approximating macroscopic equations. In the case of the cell surface receptor dynamics we will use a *parabolic scaling* technique which leads to an additional haptotactic[3] drift term for the whole population on the macroscale.

Multiscale approaches using kinetic theory provide an explanatory advantage compared to direct macroscopic modelling by partial differential equations. Typically, former models used reaction-diffusion equations and relied on an educated guess for the diffusion coefficient, which has often been assumed to be isotropic and hence independent from the direction, or even spatially constant (see section 2.6 for a review of the corresponding models). These models encompass some significant shortcomings, which can be faced by more complex multiscale models. Diffusion limits of kinetic equations are typically partial differential equations of the diffusion-advection-reaction type, and provide explicit forms for the diffusion tensor and drift velocity which conserve the information of the underlying modelling levels (micro- and meso-level). However, the derivation of macroscopic limits of kinetic equations, particulary with additional drift

[3] Haptotaxis refers to the directed movement towards the gradient of a non soluble substance.

terms and non-constant turning rates, is not trivial.

The major goal of this thesis is hence to bring together

- biological relevant information about both cellular movement in oriented tissue structures as well as biophyscial and molecular aspects of glioma spread,
- patient specific data about the brain architecture obtained by DTI measurements,
- mathematical multiscale modelling starting from kinetic partial differential equations

as building blocks of personalized glioma spread models.

I will propose two models for the spread of glioma cells. The first one neglects proliferative effects and focuses on the impact of receptor occupancy on the macroscopic cell density. For this model I will show that a momentum expansion combined with a parabolic scaling yields an advection-diffusion equation with an additional haptotactic drift term on the macroscale. Numerical simulations will indicate that haptotaxis is responsible for the emergence of anisotropic spread patterns.
A more complex model based on a go-or-grow assumption for glioma cells will lead to an advection-diffusion-reaction equation on the macroscale. Again, a haptotactic term resulting from cell receptor dynamics on the microscale will cause anisotropic spread. Numerical simulations will show qualitatively similar behaviour to the former model, but proliferation conserves steepness of the gradients and hence produces patterns which are more 'localized'. Also, proliferation obviously increases the propagation speed of gliomas significantly.
However, these models lead to a bundle of unsolved questions rendering a lot of future work necessary which will be adressed in the discussion.

1.2. Organization of this thesis

Figure 1.3 visualizes the organization of this thesis. Part II starts with some background information about brain anatomy as well as brain tumors and the underlying molecular mechanisms in chapter 2, basic concepts of diffusion tensor imaging in chapter 3 and a brief overview on kinetic models for cellular movement in chapter 4.
Chapters 2 and 4 serve as basis for the subsequent modelling chapters 5 and 6, which provide multiscale models for glioma spread with and without proliferation in part III. Numerical aspects will be treated in part IV. Starting with a short chapter on the discretization of the the macroscopic evolution equations obtained analytically in chapters 5 and 6, the extraction of model parameters from DTI data will be explained in chapter 8, which uses some facts from the background chapter 3. Chapter 9 presents the simulation results for the evolution equations.
Concluding, chapter 10 discusses the results and particulary draws conclusions about

modelling aspects and the biological background. Some ideas for future work will also be discussed.

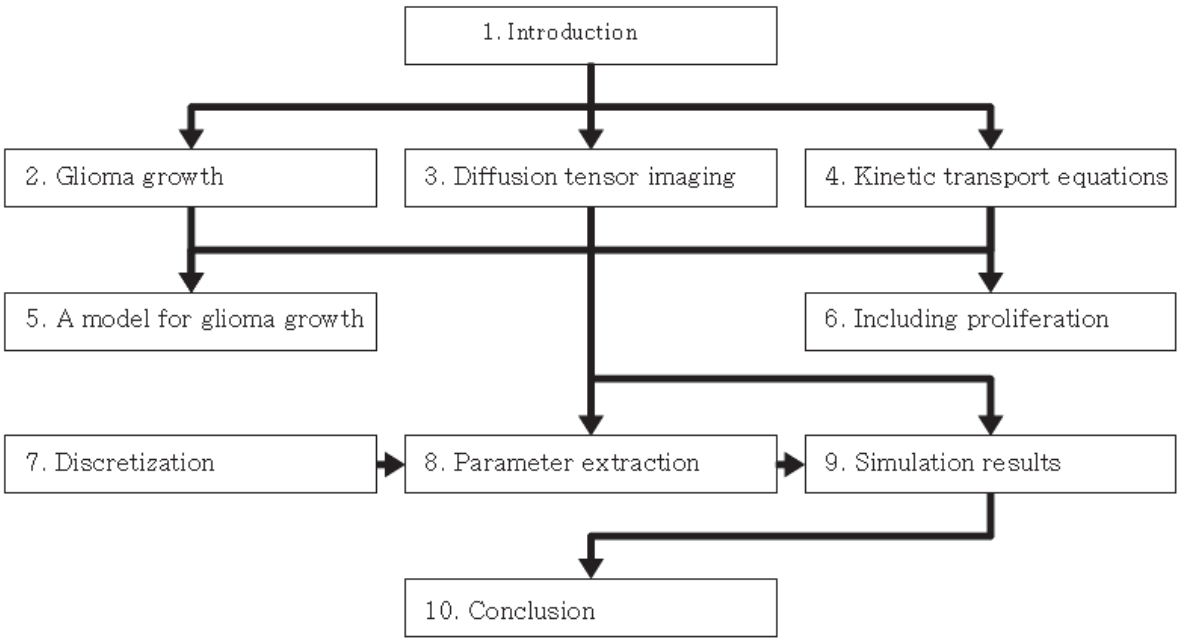

Figure 1.3.: Organization of this thesis.

1.3. Acknowledgements

I would like to express my gratitude to the following persons.

- I thank my supervisor Prof.Dr. Christina Surulescu for her patience and the introduction into the field of mathematical multiscale modelling of cancer. Without her expertise in cancer modelling and analysis of kinetic partial differential equations this thesis would not have been possible.
- Special thanks to Prof.Dr. Christian Engwer for a lot of discussions and advice in several fields. He introduced me to the field of numerics and software design concepts and really extended my modelling perspectives. Without his patient advice I would never have finished this thesis.
- Many thanks to Prof.Dr. Mario Ohlberger for the friendly financial support and the possibility to collect solid experience in teaching.
- I thank PD Dr. Carsten Wolters and Dipl.Math. Felix Lucka for providing a lot of preprocesses DTI data and an introduction to the scientific visualization tool SciRun.

Part II.

Background

2. Glioma growth in the human brain

If only we could pull out our brain and use only our eyes.

(Pablo Picasso)

Contents

2.1. Grey and white matter in the human brain

The human brain is a complex and highly dynamic biological system. Billions of neurons control the central nervous system and the peripheral nervous system, and thus all of our activities. It can be estimated that a typical human brain consists of approximately 10^{11} neurons. Each neuron itself has a central part (soma), cellular extensions with many branches (dendrites), a structure called axon and an axon terminal (see fig (2.2)). Axons are often called *nerve fibres*, and bundles of myelinated axons are called *fibre tracts* (Descoteaux, 2008).

Main components of the human brain are white matter, grey matter, blood and cerebrospinal fluid (CSF) (see figure (2.1(a)) and (2.1(b))). White matter is the main component of the central nervous system and is composed of glia cells and axonal nerve fibres. Since these are often myelinated, we see the distinctive color. Bundles of myelinated axons connect different grey matter areas of the brain and are hence important for all brain functions. It has been found that humans have a total myelinated fiber length of more than $150,000$km at the age of 20 (Marner et al., 2003).

In contrast to white matter, grey matter mostly consists of neural cell bodies and can be found at the surface of both cerebral hemispheres. Grey matter is involved in nearly all higher brain functions and usually an injury of this tissue leads to severe functional damage (Blumenfeld, 2010). Besides neurons, glia cells are the second major component of human nervous tissue. Glia cells are responsible for the electrical isolation of nerve

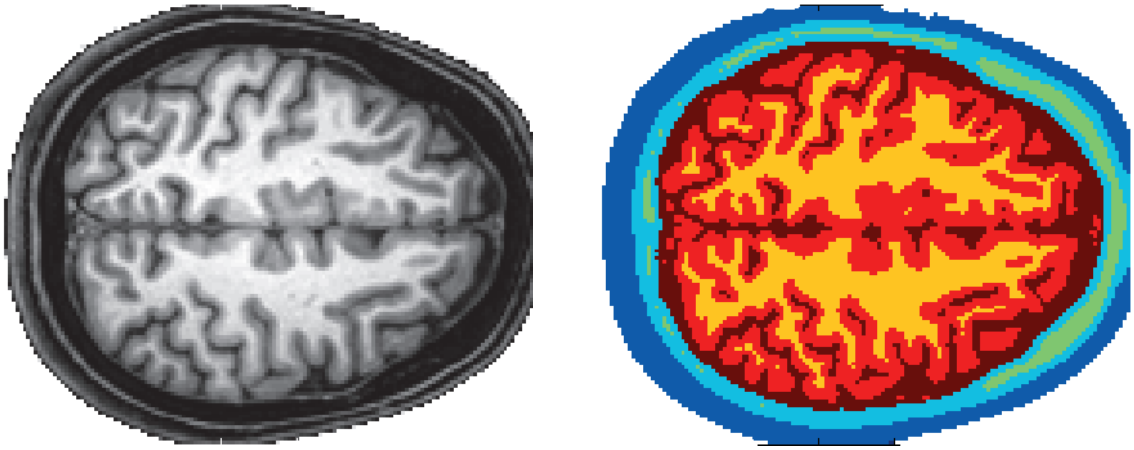

(a) T1 picture of a human brain slice. (b) Segmentation of the slice.

Figure 2.1.: Visualization of a horizontal brain slice.

cells and stabilize them mechanically. We can distinguish several types of glia cells like astrocytes, the most abundant type of glial cells, oligodendrocytes, radial glia oder Schwann cells. At least half of all brain tumors arise from glia cells. These tumors are called *gliomas*. For more information see (Blumenfeld, 2010; Abrey, 2011).

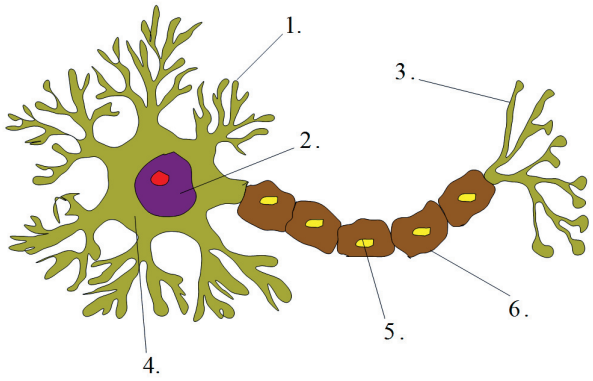

Figure 2.2.: Schematic of a neuron. 1. dendrites. 2. nucleus. 3. axon terminal. 4. soma. 5. Schwann cell. 6. myelin sheat.

2.2. Brain tumors

Brain tumors are neoplasms within the brain. Many different types of tumors can be distinguished, each of them with its own characteristics (DeAngelis, 2001), but originate in many cases from the mutation of glia cells (Ware et al., 2003). These tumors can be devasting for the patient, since they are difficult to treat and usually have a poor prognosis (for instance, more than 97% of glioblastoma multiforme patients die within

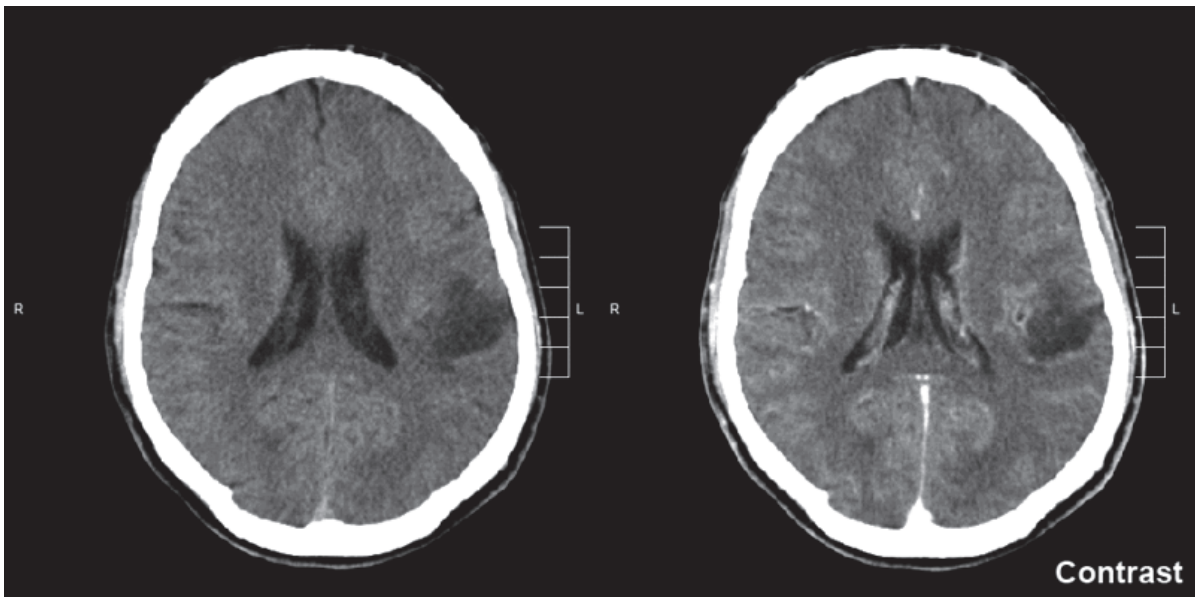

Figure 2.3.: CT scan of a WHO grade II glioma. Picture from wikimedia.org

5 years after diagnosis (Ohgaki and Kleihues, 2005)). Brain tumors can be primary or secondary tumors. In the first case, the tumor originates from a primary finding site in the brain itself. In the second case, the tumor is secondary because of metastasis. Cancer cells have the capability of invading blood or lymph vessels and circulate trough the whole lymphatic or blood vessel system. After extravasation they continue to grow, proliferate and build up secondary tumors (Geho et al., 2005). The most frequent types of brain tumors are gliomas (65% incidence (Ohgaki and Kleihues, 2005)) and meningiomas (20% incidence (Park et al., 2009)).

Most brain tumors are symptomatic, hence in most cases alterations in the patient's behaviour and perception give a hint to a brain tumor. Frequent symptoms are headache, caused by a higher intracranial pressure, vomiting and altered state of consciousness. As part of the diagnosis modern imaging methods play a central role in the detection of brain tumors.

Common high-resolution methods like computed tomography (CT) or especially magnetic resonance imaging (MRI) based methods like diffusion tensor imaging (DTI) provide powerful noninvasive tools in the detection of brain tumors (Sundgren et al., 2004). Despite the progression of those methods, the definitive diagnosis of a tumor can only be confirmed by histological tissue examination. This can be obtained by brain biopsy, for instance, and is necessary for an optimal treatment strategy. Epidemiological studies help to understand the worldwide occurrence and spread of brain tumors. It has been shown that in the western world (including North America, Europe and Australia) the overall mortality rates from nervous system tumors are approximately 4-7 deaths per 100.000 per year for men and 3-5 per 100.000 per year for women (Ohgaki and Kleihues, 2005).

The causes and risk factors for primary brain tumors are still part of ongoing research, and there is little agreement about their nature and magnitude (Wrensch et al., 2002). Many factors have been studied in relation to the risk of primary brain tumors, starting with environmental factors as tobacco smoke exposure, drugs and medications, the ionizing radiation of cell phones up to family history of brain tumors and genetic factors.

2.3. Therapy and treatment

Once a high grade glioma has been diagnosed, an efficient therapy is crucial. At present there are three major treatment approaches: surgery, radiotherapy and chemotherapy, which are usually combined in a long-term treatment (Wang and Jiang, 2013).
Surgery refers to the full or partial resection of cancerous tissue, where detailed knowledge of position, shape and extent of a tumor is essential for a successful resection. Despite enormous advances in neurosurgery during the last decades, this method encompasses some significant shortcomings. Destruction of healthy tissue or the recurrence of tumor growth at the resection boundary are, for instance, problems which are still.
In radiotherapy (Laperriere et al., 2002) the tumor is irradiated by beta oder gamma rays leading to the full or partial destruction of the DNA of cancer cells. This typically suppresses mitosis (cell division), and often leads to apoptosis (programmed cell death) of tumor cells. The impact on normal tissue is not as grave as on cancerous tissue. Hence, with an optimal dose it is possible to destroy more than 90% of cancer cells with minimal side effects.
Chemotherapy refers to cancer treatment by special drugs which destroy cancer cells but do not damage healthy cells (Kaufmann and Earnshaw, 2000). It has been shown that additional chemotherapy significantly improves the median survival rates of patients compared to patients which are treated by radiotherapy alone (Stupp et al., 2005).
However, virtually all high grade gliomas recur sooner or later (Wang and Jiang, 2013). Nevertheless, modern treatment strategies improve the median lifespan of patients and make an almost normal life possible.

2.4. Molecular mechanisms of glioma invasion

Cancer is a complex phenomenon involving many intra-, inter- and extracellular processes. Most of them are still not completely understood yet and are part of ongoing research (Geho et al., 2005; Ware et al., 2003; Visted et al., 2003; Hatzikirou et al., 2012; Hanahan and Weinberg, 2011). Since this work is concerned with glioma growth in the human brain, we will focus on the interactions of cancer cells with the underlying fibre network and on the binding dynamics of transmembrane receptors on the cell surface, which have both been shown to be key factors in glioma invasion (Visted et al., 2003). Proliferative effects will also be taken into account. Subsequently, we will briefly sum-

marize some important molecular mechanisms which are important for modelling.

Cellular movement is a complex process involving modification of the cell's shape by reorganization of its actin cytoskeleton, attachment to the surrounding fibre structure in the extracellular matrix in order to generate forces, as well as binding processes on the cell surface which trigger different signal cascades leading, inter alia, to polarization of the cell (Demuth and Berens, 2004; Friedl and Broecker, 2000). The extracellular matrix (ECM) is a part of animal tissue which provides mechanical stability to the cells. The ECM is composed of fibrous proteins, proteoglycans and adhesive glycoproteins as soluble matter. Moving cells bind to protein fibres in the ECM in order to generate traction forces to pull themselves forward (Demuth and Berens, 2004; Goldbrunner et al., 1999). This happens via *focal adhesions*, which connect the ECM proteins to the actin cytoskeleton in the cell interior. Furthermore, it has been shown in experiments, that glioma cells follow myelinated white matter fibre tracts for the invasion (Giese and Westphal, 1996).

The cytoskeletal model for cellular movement states that in the front of the cell rapid actin polymerization is responsible for the generation of a motile force. In this process soluble *globular actin* (G-actin) is transported to the front end of the cell where it is polymerized to the *filamentous actin* (F-actin) which builds up the rigid structure called *cytoskeleton*. Transmembrane glykoproteins called *integrins* attach to the surface on which the cell is crawling, hence besides internal processes like actin cytoskeleton dynamics and signaling, the dynamics of cell surface receptors is of high relevance (Geho et al., 2005; Ware et al., 2003). We focus on the integrin superfamily which is closely related to cancer invasion (Moschos et al., 2007) and is responsible for cell-matrix interactions as well as cell-cell interactions (Desgrosellier and Cheresh, 2010).

Integrins are heterodimeric proteins, consisting of two subunit chains (called α and

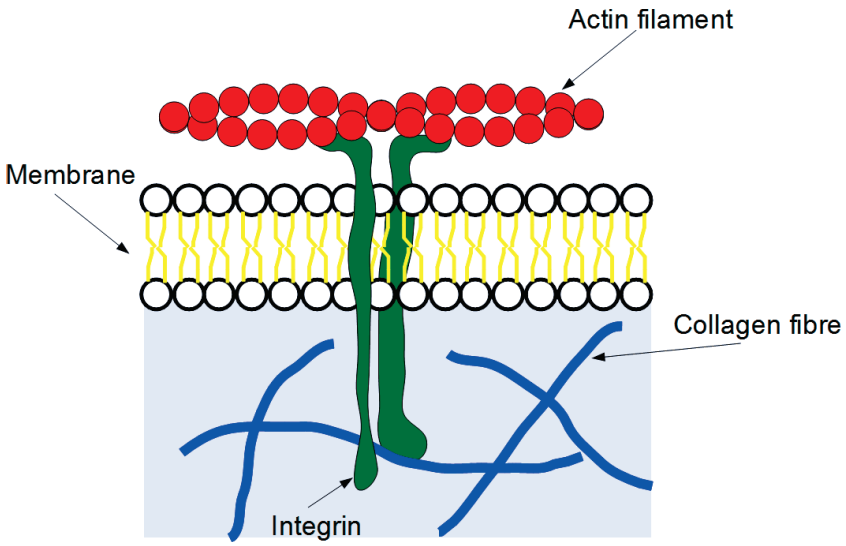

Figure 2.4.: Integrins (green) binding to collagen fibres (blue) in the extracellular matrix.

β chain). Currently, 18 different α and eight β subunits are known, which can build up 24 different integrins (Hynes, 2002). The interaction of these molecules with several ECM molecules enable cells to adhere, to spread and to migrate since they connect all interior components of the cell to their extracellular environment. Since integrins are also responsible for the transduction of extracellular information into the cell interior they also influence cell proliferation. Uncontrolled proliferation is one of the main characteristics of tumor growth, hence mathematical modelling has to take this process into account. In experiments with cultures of glioma cells it has been shown that cells either move or proliferate, which means that movement and proliferation are mutally exclusive processes (Giese et al., 2003). This is known as the migration/proliferation dichotomy or *go or grow* mechanism (Hatzikirou et al., 2012). We will take this paradigm into account in our modelling.

Of course there are many other processes which are assumed to be important for glioma invasion, which have been neglected in this work but have been investigated in other studies. The following processes will *not* be taken into account in this work, but would be interesting for future investigations:

- a class of enzymes called *proteases* which degrade the ECM in a proteolytic process have been shown to play a crucial role in glioma invasion (Rao, 2003; Binder and Berger, 2002).
- Intracranial tumors lead to a mechanical deformation of adjacent tissue.
- Metastasis leads to the formation of secondary tumors.
- Angiogenesis and vascular growth should be taken into account if one observes a tumor over a long period of time.

This list is, of course, not complete but only reflects just some interesting further issues. However, since mathematical modelling is limited and cannot represent the whole complexity of the biological real world one has to focus on some key aspects.

2.5. What mathematics can do

Commonly, modern imaging methods are used for both diagnosis of brain tumors as well as for treatment planning. So, is there a need for complex mathematical models at all? There is. A significant shortcoming of imaging methods is that they cannot reveal the highly invasive borderline of the tumor. This often leads to an incomplete removal of the cancerous tissue, and the tumor will start growing again after surgical treatment. Detailed knowledge about position, shape and extent of the invasive borderlines of the tumor could solve this problem. Resection of the tumor according to that exact information would avoid regrowth and would help to destroy just a minimal amount of healthy tissue at the same time. Mathematical multiscale modelling in combination with the use of modern imaging data can help to provide such detailed information. Patient specific models including personalized information about the neuronal tissue structure could be

used as a supplementary tool besides imaging methods to plan surgical removal of the tumor as well as radiotherapy.

Sometimes the question arises, what we would call a 'good' model for gliomas. This question is hard to answer and is also a question of viewpoint (that means, for instance, if one is interested in a deeper understanding of the involved biochemical and biomechanical processes or just in the visual reproduction of patters which look similar to 'real' brain tumors). Nevertheless, we can collect some characteristics which a useful model should achieve.

- **Physical principles**
  Good biomathematical modelling relies on appropriate physical principles. Most phenomenologically motivated macroscopic models rely on an educated guess for some important expressions as, for instance, the choice of coefficients in advection-diffusion-reaction equations although these terms could be derived from more basic biophysical principles.

- **Multiscale approach**
  Cancer is a complex phenomenon. Mathematical models should take this circumstance into account and need to be capable to represent a sufficient level of complexity. Multiscale approaches are promising, since they can address multiple biologically relevant processes on different spatial and temporal scales.

- **Personalized modelling**
  It is important to take the patient's tissue structure into account. If mathematical modelling aims at providing models and methods which should be able to find their way to clinical applications it is necessary to find ways to use patient specific data efficiently.

- **Model validation**
  The impossibility of validation is often a weak point of mathematical models. It is usually hard to get access to suitable data, and it is often harder to compare simulation results of the model to those data. Nevertheless, a good model should offer (at least in principle) the possibility of validation.

However, this list is not complete, but shows that modelling has to be more than writing down an equation and perform some numerical simulations. Instead, one has to focus back on the biological problem if mathematics really wants to be useful for applications. In the following section we review some existing models for glioma growth.

2.6. Review of mathematical models for glioma

During the last years a large variety of models for various aspects of cancer has been proposed and analyzed. We will not review the full spectrum here but focus on work

concerned with brain tumors and survey the most popular model classes including differential equation models as well as descriptions based on cellular automata.
Early works concerned with glioma spread proposed macroscopic models which employ reaction-diffusion equations for a tumor cell density $\rho(t, x)$ of the form

$$\partial_t \rho = \nabla \cdot \big(D_T \nabla \rho\big) + g(\rho), \tag{2.1}$$

where the diffusion coefficient D_T can be a constant, a space-dependent scalar function or a tensor and g is a function describing the proliferation behaviour[1]. Models of this type focusing on diffusion and proliferation have been studied extensively during the last years (Cruywagen et al., 1995; Tracqui, 1995; Tracqui et al., 1995; Swanson et al., 2003).

A significant shortcoming of these approaches is that they do not fit tumor growth patterns observed in biology. There are two key points. The first one is that diffusion is assumed to be constant, which is quite unrealistic with respect to the high spatial inhomogeneity within the brain. The second one is that it is questionable if the transport of cells is purely diffusive, and active transport processes like advection can be neglected. However, these models appear not sufficiently realistic with a view on the complex neural fibre structure in human brains which lead to anisotropic, finger-like spread patterns.
The usage of more complicated reaction-diffusion-advection equations of the form

$$\partial_t \rho = \nabla \cdot \big(D_T(\mathbf{x}) \nabla \rho + u_T(\mathbf{x}) \rho\big) + g(\rho), \tag{2.2}$$

with nonconstant diffusion coefficient D_T and drift velocity u_T was the next step in modelling brain tumors.

Obviously, the architecture of the underlying tissue structure cannot be neglected. This leads to the idea of personalizing tumor growth models by using patient specific DTI data. As shown in section 3.5, DTI data can provide information about the orientation of neuronal fibre tracts for each voxel, and it seems adequate to use this fact in mathematical modelling.
Among the first, Swanson et al. studied the impact of imaging data on glioma modelling (Swanson, 1999; Swanson et al., 2000). There, the authors used two different diffusion coefficients $D(\mathbf{x})_{\text{white}}$ and $D(\mathbf{x})_{\text{grey}}$ in equation (2.1) for brain white, respectively brain grey matter, but assumed diffusion to be constant within each regime. Since it has been observed that cells diffuse faster in white matter, they related $D(\mathbf{x})_{\text{white}}$ and $D(\mathbf{x})_{\text{grey}}$ by $D(\mathbf{x})_{\text{white}} = 5D(\mathbf{x})_{\text{grey}}$. They used horizontal slices of T1 weighted images in order to obtain patient specific domains for the numerical treatment. However, numerical simulations showed slightly anisotropic growth patterns, but obviously the anisotropy was predominantly caused by the geometry of the simulation domain. Similar results have been obtained by Suarez et al. from a more clinical point of view (Suarez et al., 2012).

[1] typically, logistic growth is employed.

As a next step, one could introduce diffusion constants which do not just depend on the spatial position, but are tensor valued functions which are capable to represent directional dependence of diffusivity. Jbabdi et al. introduced tensor-valued diffusion coefficients for the modelling of glioma spread (Jbabdi et al., 2005). Starting with a reaction diffusion equation of the form (2.1) multiples of the water diffusion tensor obtained from DTI measurements have been used as tumor diffusion tensor in their calculations to address the anisotropy. The resulting numerical simulations showed slightly anisotropic behaviour in comparison with the former mentioned simpler models. However, this choice of the diffusion constant corresponds, more or less, to an educated guess, and deeper insight into derivation of appropriate forms for the coefficient would be favourable. Similar macroscopic models have been also proposed by (Clatz et al., 2005; Bondiau et al., 2008; Konukoglu et al., 2010).

Kinetic models (see chapter 4) are powerful tools for the derivation of advection-diffusion equations from simple biophysical principles. Hillen proposed in (Hillen, 2006) a kinetic model which is capable to include local tissue information on the mesoscale and yields an approximating advection-diffusion equation for the tumor cell density on the macroscale. The diffusion and advection constants depend on the local tissue structure, and can be computed explicitly. In (Painter and Hillen, 2013), the authors combine this mesoscale approach with the usage of DTI data for a personalized simulation of glioma growth. It becomes apparent, that the anisotropy of neural tissue influences the anisotropic spread of tumor cells, which is visible in their numerical simulations. Though, the anisotropy did not show the characteristics which were known from clinical practice.

In the previous models it has been assumed that cellular movement can be described as predominantly diffusive process, despite the fact that cells move biased towards preferred directions. More complex multiscale models extended existing kinetic models, and introduced another scale into the modelling. In (Kelkel and Surulescu, 2011, 2012) the authors start on the level of cellular receptor binding, and describe the movement of cancer cells in tissue networks. A macroscopic limit of a simplified model has been derived in (Engwer et al., 2013), and numerical simulations indeed showed highly anisotropic growth patterns, which occured due to an additional drift term resulting from the cell surface receptor dynamics.

Another modelling point of view focuses on cellular automata based descriptions, which are widely used for the modelling of biological pattern formation (Deutsch and Dormann, 2005). Basically, a cellular automaton is characterized by four elements: a lattice of cells or nodes, a set of states for each element of the lattice, a characterization of the neighborhood of each lattice element as well as a transformation rule which regulates the transitions in the state space for each time step. In this discrete approach, cancerous cells can invade their neighbours with a certain probability in each time step, leading to the spatial spread, where the emerging patterns are determined by the transition rules. A typical cellular automata model for glioma growth has been proposed in

(Aubert et al., 2006), where the authors presented simulation results for a 2d automaton on a hexagonal lattice. However, although this individual based approach can be accessed relatively easy and enables the implementation of cellular behaviour via simply transition rules, it is not clear how to use personalized data in this context.

Glioma models still face a lot of open problems, and modelling will become more and more complex. Although multiscale approaches are promising, recent models still neglect plenty of biologically relevant processes. A good review of glioma models can also be found in (Hatzikirou et al., 2005). Some ideas for future work in this field will be discussed in chapter 10.

3. Diffusion tensor imaging

If your pictures aren't good enough, you aren't close enough.

(Robert Capa)

Contents

3.1. Medical imaging

Medical imaging helps to provide images of the human body in a noninvasive way. These techniques play a crucial role in diagnosis and treatment of many human diseases and provide detailed information about anatomical and physiological characteristics of a patient. A large spectrum of methods is available, from radiography over tomography and ultrasound up to magnetic resonance imaging, each with its own specialization. In this work we will focus on *diffusion tensor imaging* (DTI) which we will outline below.The following sections are partially adapted from (Engwer et al., 2013).

3.2. Diffusion tensor imaging

A diffusion constant does not contain any directional information, and is hence not fully appropriate for the description of diffusion in directed biological tissues. This led to the development of diffusion weighted imaging (DWI). Around 1985, Wesbey et al. (Wesbey et al., 1984a,b) made the first DWI acquisitions, but these were not appropriate for clinical practice. LeBihan et al. (LeBihan et al., 1986) were the first performing a brain DWI acquisition in vivo. Moseley later improved DWI by taking multiple gradient directions into account (Moseley et al., 1990).
This led to *Diffusion tensor imaging* (DTI), which is nowadays the preferred radiological method to get information about the cerebral tissue structure of the human brain in a noninvasive way and has several applications in clinical practice (Sundgren et al., 2004).

Figure 3.1.: MRI device. Picture by courtesy of Carsten Wolters, Institute for Biomagnetism and Biosignalanalysis, University of Münster.

DTI is a variant of *diffusion weighted magnetic resonance imaging* (DW-MRI). Moseley observed that the apparent diffusion of water molecules within brain white matter is highly anisotropic and assumed that the diffusion behaviour of water molecules within structured tissue also contains information about the tissue architecture itself. Hence, these methods relate the anisotropy of water diffusion to the anisotropy of neural tissue, particulary of brain white matter (Jellison et al., 2004).

In the early 1990ies, Basser et al. proposed a tensor model that is capable to represent anisotropic aspects of diffusion (Basser et al., 1992, 1993; Matiello and LeBihan, 1994a,b). Here, the diffusion pdf of water is approximated by a tensor model, where the tensor is assumed to be symmetric and positive definite. The model is still Gaussian but it has six degrees of freedom instead of one. The diffusion of water molecules is assumed to be Brownian in an isotropic medium, that means there is no directional dependence of diffusion. In contrast, in a fibrous or structured environment water molecules diffuse faster along the structure. This directional preference causes the anisotropy, and is hence the physical basis for DTI. These ideas led to diffusion tensor imaging in its contemporary form which is capable to measure the anisotropic diffusion properties of biological tissues.
For more details about the physical and historical background background of diffusion see chapter 4.2 of (Descoteaux, 2008; Hagman et al., 2006), for a review of mathematical aspects see (Lenglet et al., 2009)

Technically, DTI measures the spatial diffusion of water molecules by magnetic res-

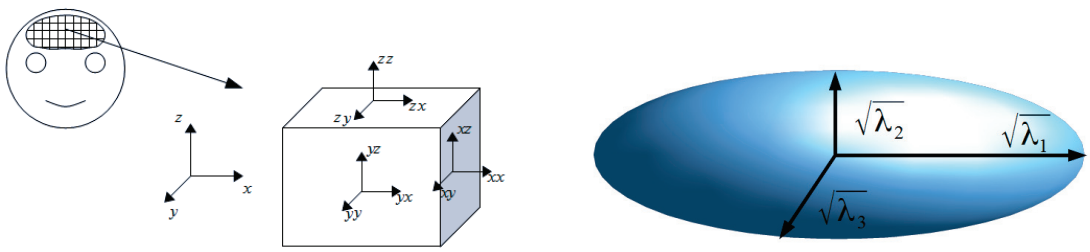

(a) Diffusion behaviour per volume element (voxel).

(b) Representation of diffusion tensor data by an ellipsoid.

Figure 3.2.: Diffusion tensor imaging measures the spatial diffusion of water molecules by MRI per volume element. This yields a symmetric apparent water diffusion tensor which represents the directional dependent diffusivity of water molecules (a). Since there is no direct intuitive access to data in tensor form, ellipsoids can be used to visualize data in tensor form. Fig. (b) shows the representation of the tensor by an ellipsoid whose axes are scaled with the tensor eigenvalues $\lambda_1(\mathbf{x}), \lambda_2(\mathbf{x})$ and $\lambda_3(\mathbf{x})$.

onance imaging per volume element (**vo**lumetric pi**xel**). This leads to a symmetric diffusion tensor

$$D(\mathbf{x}) = \begin{pmatrix} d_{xx}(\mathbf{x}) & d_{xy}(\mathbf{x}) & d_{xz}(\mathbf{x}) \\ d_{yx}(\mathbf{x}) & d_{yy}(\mathbf{x}) & d_{yz}(\mathbf{x}) \\ d_{zx}(\mathbf{x}) & d_{zy}(\mathbf{x}) & d_{zz}(\mathbf{x}) \end{pmatrix}$$

for each voxel (see figure 3.2(a)), containing the full (apparent) diffusion information along six directions (Hagman et al., 2006). For each voxel, the orientation of neural fibre tracts is of great interest. In this discrete and Cartesian view of the brain each voxel has a volume of less than one mm^3, hence a typical size of a DTI data set is of order 10^6 - meaning we need millions of tensors to represent the tissue architecture of a human brain. Since we assumed that the diffusion is Gaussian this approach is not capable to resolve multiple fibre crossings in a voxel and is hence still not optimal. Recently, improved high angular resolution imaging techniques tried to solve this problem. We will come back to this issue later.

3.3. Data used in this thesis

DTI data used in this thesis has been provided by courtesy of Carsten Wolters [1]. The data comprises apparent diffusion tensor values for a Cartesian head grid of size $117 \times 124 \times 142$ voxels as well as a segmentation distinguishing white and grey matter regions from bones, cords and cerebrospinal fluid. The computational domain Ω used in the numerical simulations is given by the union of grey and white matter regions.

[1] Institute for Biomagnetism and Biosignalanalysis, University of Münster

In several preprocessing steps the data has already been cleaned up, including, for instance, removal of singular voxels. The data was provided in the proprietary `Matlab` format. The tensor glyph visualizations in this section have been produced with the visualization tool SciRun. I thank Felix Lucka[2] for the introduction into this software system.

3.4. Representation of DTI Data

DTI measurements lead to tensor data for each voxel of the observed human brain. Since we have no direct intuitive access to data in tensor form, it is necessary to visualize the contained information in some way. Several methods have been developed to uncover the anisotropy of a diffusion tensor. In general, there are two main approaches: either one uses scalar indices as a measure of anisotropy or geometric objects called *tensor glyphs* which encode the anisotropic structure of a tensor by, for instance, *ellipsoids* or *peanuts*. We will discuss these two major approaches in more detail in the following.

3.4.1. Scalar indices: fractional anisotropy

Fractional anisotropy (Pierpaoli and Basser, 1996; Beppu et al., 2003) is a scalar value between zero and one, calculated by the eigenvalues of the apparent diffusion tensor. A value close to one corresponds to a high anisotropy (that means, a strong preference of a specific direction), whereas a value close to zero correnspponds to the nearly isotropic case.
Since the diffusion tensor is assumed to be symmetric, it can be diagonalized. After the process of diagonalization we obtain a diagonal matrix containing the eigenvalues $\lambda_1(x), \lambda_2(x), \lambda_3(x)$ on its main diagonal. Since the diffusion tensor depends on the position x, the *fractional anisotropy index* (FA) is then defined per voxel by

$$FA(x) = \frac{\sqrt{3}}{\sqrt{2}} \frac{\sqrt{(\lambda_1 - \overline{\lambda})^2 + (\lambda_2 - \overline{\lambda})^2 + (\lambda_3 - \overline{\lambda})^2}}{\sqrt{\lambda_1^2 + \lambda_2^2 + \lambda_3^2}} \tag{3.1}$$

with $\overline{\lambda} = \frac{\lambda_1+\lambda_2+\lambda_3}{3}$. A typical fractional anisotropy map of a human brain can be seen in fig.(3.3(c)), where the FA-index has been plotted for a horizontal slice of a human male brain.
However, the fractional anisotropy index contains no directional information about the fibre tracts.

3.4.2. Tensor glyphs: ellipsoids and peanuts

Another visualization technique is the representation of a tensor by geometric objects called *tensor glyphs* (Kindlmann and Westin, 2006). These glyphs encode the information

[2] Institute for Biomagnetism and Biosignalanalysis, University of Münster

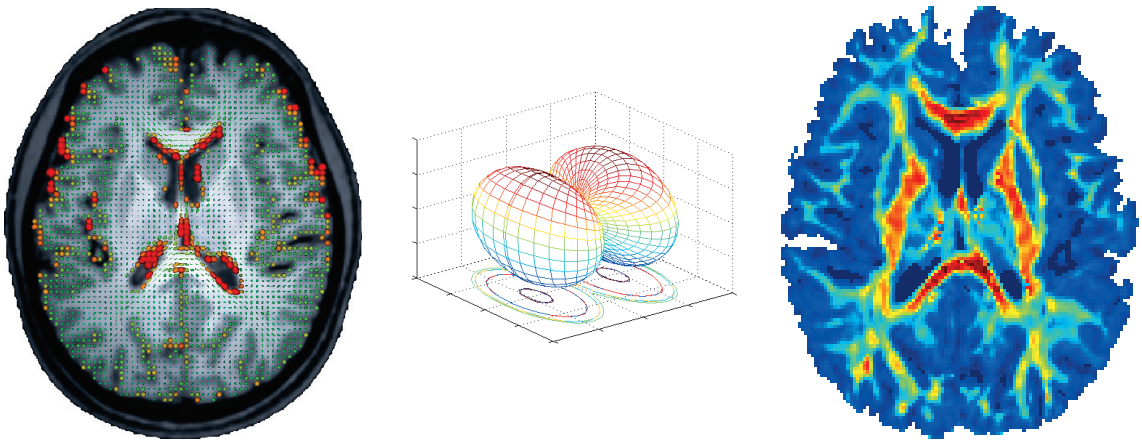

(a) Representation of diffusion anisotropy by ellipsoids.

(b) The directional distribution function $\theta \mapsto \theta D(x)\theta$.

(c) Fractional anisotropy index plotted for a horizontal slice of a human brain.

Figure 3.3.: Visualization of tensor imaging data.

of a tensor in more detail than a scalar index does. Common glyphs are *ellipsoids* and *peanuts*.
Let $\mathbf{v}_1, \mathbf{v}_2$ and $\mathbf{v}_3$ be eigenvectors and λ_1, λ_2 and λ_3 the corresponding eigenvalues. We can then write

$$\mathbb{D}(\mathbf{x}) = \begin{pmatrix} d_{xx}(\mathbf{x}) & d_{xy}(\mathbf{x}) & d_{xz}(\mathbf{x}) \\ d_{yx}(\mathbf{x}) & d_{yy}(\mathbf{x}) & d_{yz}(\mathbf{x}) \\ d_{zx}(\mathbf{x}) & d_{zy}(\mathbf{x}) & d_{zz}(\mathbf{x}) \end{pmatrix} = \begin{pmatrix} \vdots & \vdots & \vdots \\ \mathbf{v}_1 & \mathbf{v}_2 & \mathbf{v}_3 \\ \vdots & \vdots & \vdots \end{pmatrix} \begin{pmatrix} \lambda_1 & 0 & 0 \\ 0 & \lambda_2 & 0 \\ 0 & 0 & \lambda_3 \end{pmatrix} \begin{pmatrix} \dots & \mathbf{v}_1 & \dots \\ \dots & \mathbf{v}_2 & \dots \\ \dots & \mathbf{v}_3 & \dots \end{pmatrix}.$$

Let now $\tilde{D}$ denote the diagonal matrix on the right side. The diffusion ellipsoid is given by the 1-level sets of $\theta^t \tilde{\mathbb{D}}^{-1} \theta$, that means as the surface defined by

$$\frac{\theta_1^2}{\lambda_1} + \frac{\theta_2^2}{\lambda_2} + \frac{\theta_3^2}{\lambda_3} = 1.$$

Hence, the $\sqrt{\lambda_i}$ indicates the diffusivity in direction v_i. In the case of isotropic tissue, for instance, where no direction is preferred by the diffusing water molecules, the corresponding ellipsoid is just a ball, since in this case approximately $\lambda_1 = \lambda_2 = \lambda_3$ holds. If the tissue is strictly aligned, there is one mean direction of diffusion, and this information is also contained in the diffusion tensor. In this case, the corresponding ellipsoid is cigar-shaped. See also figures (3.4(a))-(3.4(i)) for the connection between tissue architecture and diffusion ellipsoids.

Instead of ellipsoids one can also use objects called *peanuts* for the visualization (see fig. 3.3(b)). These arise, when we look at the *directional distribution function* given by $\mathbb{S}^{n-1} \ni \theta \mapsto \theta^t \mathbb{D}(x)\theta \in \mathbb{R}$. The corresponding object contains not the same information as the ellipsoid. For each direction θ, given by a point on the unit-sphere $\mathbb{S}^{n-1}$, a peanut represents the diffusivity along this direction.

3.5. Diffusion tensor imaging and neuronal tissue structure

The orientation of neural fibre bundles within brain white matter is of great interest in the prognosis of glioma spread in the human brain. *Tractography* (Descoteaux, 2008; Descoteaux et al., 2009; Fernandez-Miranda et al., 2012) is concerned with the identification of crossing fibre bundles in a noninvasive way, using MRI based imaging data. Currently, most methods use a Gaussian tensor model to characterize the probability density function of water molecules in order to obtain the *orientation distribution function* of neural fibres. From the mathematical point of view one is interested in the ratio of fibres which have orientation θ, where θ can be any point on the unit sphere $\mathbb{S}^{n-1}$. The tensor model relates the principle diffusion direction of water molecules to the main orientation of fibres. Although this approach gives some rough information about the local tissue structure within a brain, the tensor model assumption encompasses some significant shortcomings. Particularly the fact that only one single fibre main direction per voxel can be represented is very limiting, since there can be crossing or splitting fibre bundles in each voxel as well. To examine the relation between water diffusion data and the actual fibre orientation distribution function is still challenging.

Personalized multiscale modelling of glioma growth requires information about the patients' local tissue structure. In this work I make the simplifying assumption that the relationship between water diffusion tensor data and the fibre orientation function can be represented by a simple mathematical expression, although this assumption has not been verified yet (otherwise the field of tractography would be obsolete). In section 5.4 possible choices for the relation of the water diffusion tensor $\mathbb{D}_W$ and the local fibre distribution q will be discussed. The most intuitive approach is, to use a directional distribution function of the form

$$q(\mathbf{x}, \theta) = \frac{n}{|\mathbb{S}^{n-1}| \operatorname{tr} \mathbb{D}_W(\mathbf{x})} \theta^t \mathbb{D}_W(\mathbf{x}) \theta, \tag{3.2}$$

which gives for each position $\mathbf{x}$ the ratio of fibres which have orientation θ. This expression involves for each space point the according values $\mathbb{D}_W(\mathbf{x})$ of the apparent water diffusion tensor. I will come back to this point later.

However, the tensor model has often been criticized for being too simple because of the small directional resolution. Recently developed methods in tractography provide more powerful methods for the evaluation of neural fibre tracts, and it could be promising for the future to investigate the impact of those methods to the multiscale models used in this work. So called *high angular resolution diffusion imaging*- techniques as, for instance, Q-ball imaging (Tuch, 2004, 1996; Tuch et al., 2003) or analytical Q-ball imaging (Descoteaux, 2008) make it possible to resolve multiple fibre crossings within one single voxel. Recently, probabilistic methods have also been investigated (Descoteaux et al., 2009).

(a) The isotropic case. Fibres are not aligned.

(b) One directional alignment of fibres. There is a higher diffusivity in the alignment direction.

(c) Two crossing fibre tracts. There are two main directions of diffusion.

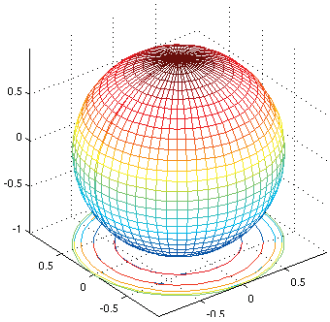

(d) The diffusion ellipsoid according to the isotropic case is a ball.

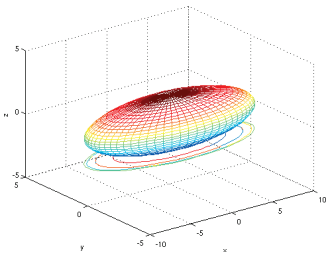

(e) The diffusion ellipsoid is cigar-shaped for strictly aligned fibre tracts. This is called *prolate diffusion*.

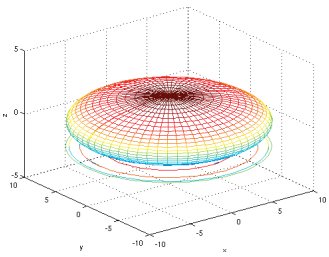

(f) In the case of two crossing fibre tracts we obtain a pancake. This is called *oblate diffusion*.

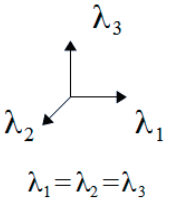

(g) All eigenvalues are of equal order in the isotropic case. There is no directional preference.

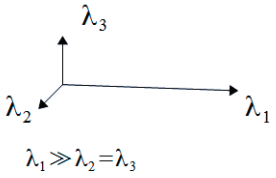

(h) There is one leading eigenvalue for one main direction of diffusion.

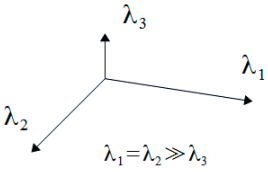

(i) In the case of crossing fibre tracts, we obtain two leading eigenvalues.

Figure 3.4.: Relation of local tissue orientation and water diffusion.

4. Cellular movement and kinetic transport equations

Inequality is the cause of all local movements.

(Leonardo Da Vinci)

Contents

4.1. Biomathematical modelling on multiple scales

Biology can be characterized as a natural science which is concerned with the study of life and living organisms. This involves a large variety of phenomena and systems, each of them with important features on multiple spatial and temporal scales. Biochemical processes inside a single cell happen within milliseconds in a spatial range of micrometers, whereas some organisms reach lifespans of more than one hundred years[1] or even thousands[2] of years or grow to a size of several square kilometers[3]. Mathematical modelling of those systems faces the challenge to address all involved scales at the same time. If we focus, for instance, on mathematical modelling of tumor growth, a large variety of processes is relevant from the biological point of view as shown in section 2.4. Naturally the question arises how to link these scales mathematically in order to obtain consistent models (see figure 4.1).
In the following sections we will describe some multiscale modellings aspects which are based on kinetic transport equations and focus on cellular movement.

[1] Like the Galapagos giant tortoise *Chelonoidis nigra*, see (Caccone et al., 2002).

[2] The oldest tree in the world is a specimen of the species Great Basin Bristlecone Pine *Pinus longaeva*, which is located in the White Mountains of California and has an age of more than 5000 years (Moore et al., 2008).

[3] Colonies of the fungus *Armillaria ostoyae* have a size of several square kilometers (Berube and Dessureault, 1988).

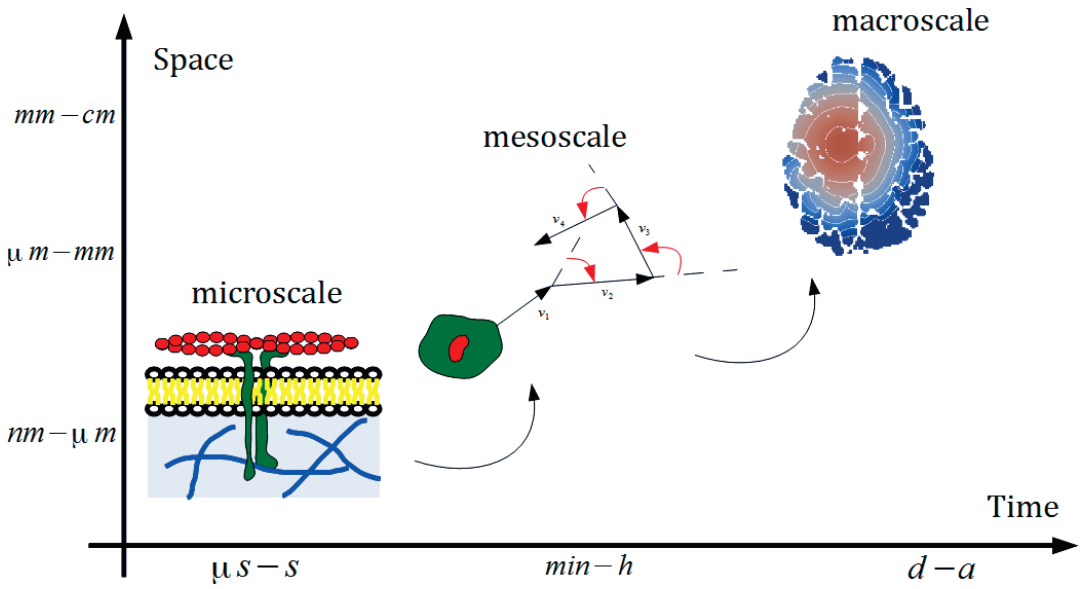

Figure 4.1.: Multiple scales in the modelling of cancer. Starting with molecular dynamics of cell surface receptors one also has to consider the behaviour of single cells up to properties of a tumor on the population scale. The aim is to link the different scales.

4.2. Mesoscopic and macroscopic descriptions of movement

If we observe systems of interacting biological entities, there are at least two possible major modelling approaches: one can either think on the *macroscopic* population level, or on the *mesoscopic* individual level. The first option gives a mean field view on a whole population, where we lose information about the single entity on the one hand but yield as a trade off a good overall description of the whole system on the other hand.

The second option offers the possibility to take individual behaviour of single entities into account. The corresponding (mesoscopic) models are in general more complex than (macroscopic) mean field models, but enable modelling in a more detailed fashion. In many cases it is possible to find a connection between the mesoscopic (individual based) view and the macroscopic (population based) view. If we know the behaviour of all single particles in our system, we can make some prediction about the whole populations' behaviour. In the following, we will model cellular behaviour by kinetic transport equations. The idea to use these equations for the modelling of biological systems arose in the 1980s, where it started with two seminal works by Wolfgang Alt (Alt, 1980, 1981). Further works during the next decades enlarged the theory and its applications (Othmer et al., 1988; Hillen and Othmer, 2000; Othmer and Hillen, 2002).

One main assumption in the kinetic framework is, that cells perform a velocity jump

process while moving. This means that cells move straightforward on a line for a certain time, then stop and change their direction, possibly due to environmental cues, turn and move forward again (see fig. 4.2). The rate λ which describes the frequency of velocity

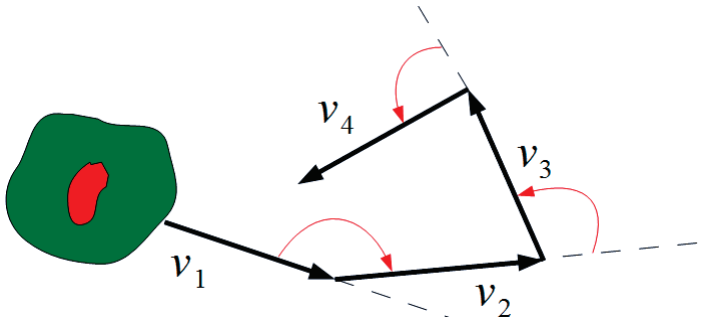

Figure 4.2.: Sketch of a cell performing a velocity jump process. The cell follows a straight line in the direction of its velocity v_1, then chooses a new direction of movement and continues its movement in direction v_2 and so on.

changes is called *turning rate* and is closely related to the *mean run time*, which is given by the inverse $\frac{1}{\lambda}$. Biological experiments have shown that turning rates of cells differ from cell type to cell type. It is also assumed that the time for the reorientation of the cell is short compared to the mean run time.
We hence assume that cellular movement can be described by a velocity jump process (Poisson process) and observe the density $p(t, \mathbf{x}, \mathbf{v}, \mathbf{y})$ of cells with velocity $\mathbf{v} \in V \subset \mathbb{R}^n$ and microscopic state $\mathbf{y} \in Y \subset \mathbb{R}^l$ at position $\mathbf{x} \in \mathbb{R}^n$ and time t.Typically, V is assumed to be symmetric of the form $V = [s_1, s_2] \times \mathbb{S}^{n-1}$. In the following we will assume without loss of generality that cell speed is constant and that hence V is of the form $V = s\mathbb{S}^{n-1}$. This leads to kinetic models with additional internal variables of the form

$$\partial_t p + \nabla_{\mathbf{x}} \cdot (\mathbf{v}p) + \nabla_{\mathbf{y}} \cdot (Gp) = -\lambda(\mathbf{y})p + \int_V \lambda(\mathbf{y}) K(\mathbf{x}, \mathbf{v}, \mathbf{v}') p(\mathbf{v}') d\mathbf{v}'. \tag{4.1}$$

Here, $\mathcal{L}p := -\lambda(\mathbf{y})p + \int_V \lambda(\mathbf{y}) K(\mathbf{x}, \mathbf{v}, \mathbf{v}') p(\mathbf{v}') d\mathbf{v}'$ is the *turning operator* which models the velocity changes of the cells due to contact guidance, environmental cues etc. $\lambda(\mathbf{y})$ is the *turning rate* which we assume to be dependent on the microscopic state $\mathbf{y}$ of a cell. Furthermore, $K(\mathbf{x}, \mathbf{v}, \mathbf{v}')$ is called *turning kernel* which should satisfy the distribution property

$$\int_V K(\mathbf{x}, \mathbf{v}, \mathbf{v}') d\mathbf{v} = 1.$$

The kernel K can be seen as the likelihood of a cell moving with velocity $\mathbf{v}'$ to switch to the new velocity $\mathbf{v}$ after its reorientation. The variable for microscale dynamics $\mathbf{y}$ (modelling, for instance, protein concentrations within the cell or receptor dynamics on the surface) is given by a system of ordinary differential equations

$$\frac{d}{dt}\mathbf{y} = G(\mathbf{y}, Q). \tag{4.2}$$

These processes depend usually on some macroscopic concentration of some substance $Q(\mathbf{x})$. This mesoscopic description of cellular movement is quite complex and in particular the high dimension (n dimensions for each space and velocity as well as p for the internal variables, hence $2n + l$) of the state space complicates the numerical treatment of these models significantly. Thus, it is desirable to reduce the dimension of the state space, and to find approximating equations for the macroscopic cell density

$$n(\mathbf{x}, t) := \int_Y \int_V p(t, \mathbf{x}, \mathbf{v}, \mathbf{y}) d\mathbf{v} d\mathbf{y}. \tag{4.3}$$

It has been shown that typically partial differential equations of the advection-diffusion type of the form

$$\partial_t n(\mathbf{x}, t) = \nabla \cdot \big(\mathbb{D}(x) \nabla n(\mathbf{x}, t)\big) + \nabla \cdot \big(u(x) n(\mathbf{x}, t)\big), \tag{4.4}$$

arise as macroscopic approximations of kinetic models. The coefficients $D(\mathbf{x})$ and $u(\mathbf{x})$ are derived from the mesoscopic level contrary to most macroscopic models where they are estimated by an educated guess.

The question of how complex a process is depends on how we look at it. A mesoscopic viewpoint leads to high dimensional problems, because in this case we are 'closer' to our biological model system. If we change our perspective and observe the same system from a distance, details disappear and one obtains a simplified mean field description of the process. From a mathematical point of view one has to change the scale of observation by rescaling the time and space variables of the system. Depending on this rescaling one obtains different macroscopic approximations each with its specific characteristics. Typical scalings used in kinetic modelling of cellular movement are *parabolic scaling* and *hyperbolic scaling*, which lead to diffusion dominated respectively advection dominated macroscopic equations.

4.3. Existence of a solution

To address the question of existence of a solution for kinetic equations with additional microscale dynamics of the form (4.1) we will use a result developed by Surulescu and Lorenz in (Lorenz and Surulescu, 2014) where the authors studied a class of related models. This article generalizes former works on cancer migration models which have been investigated by Surulescu and Kelkel in (Kelkel and Surulescu, 2011, 2012). Their framework is more complex and includes both interactions with an underlying fibre network as well as chemotactic response of the cells, and hence employs turning operators for both haptotaxis and chemotaxis. A kinetic transport equation for the cell density has been nonlinearly coupled both to an ordinary differential equation for a nonsoluble substance responsible for haptotaxis as well as to a reaction-diffusion equation for a soluble chemoattractant.
This result covers also the equations studied in the present work, which arise as a

simplified special case. Contrary to the modelling in (Lorenz and Surulescu, 2014), we neglect chemotactical aspects and hence our turning operator is made up just of just one term instead of two. Furthermore, the operator does not depend on any external fields and thus there is no nonlinear coupling to other evolution equations. Particulary, we do not use an evolution equation for Q, but assume that it is a prescribed function. This leads to the following

Theorem 1 (Existence and uniqueness (Lorenz and Surulescu, 2014))**.** *For $\mathbf{y} \in Y \subset \mathbb{R}^l$ and $v \in V \subset \mathbb{R}^n$ consider the equation*

$$\partial_t p + \nabla_{\mathbf{x}} \cdot (\mathbf{v}p) + \nabla_{\mathbf{y}} \cdot (Gp) = -\lambda(\mathbf{y})p + \int_V \lambda(\mathbf{y})K(\mathbf{v}, \mathbf{v}')p(\mathbf{v}')d\mathbf{v}', \tag{4.5}$$

with the coefficient function

$$G : L^2(\mathbb{R}^+) \to \{\mathbf{g} \in L^\infty(\mathbb{R}^l) \cap L^2 | \partial_{\mathbf{y}}\mathbf{g} \in L^\infty\}.$$

Then every initial value problem for the above equation has a unique solution $p : [0, T] \to L^2(\mathbb{R}^n \times V \times Y)$ for all $T < \infty$. Moreover, p is bounded with respect to the L^2 norm.

4.4. Cellular movement in tissue networks

Since cells choose new directions by contact guidance, their migratory behaviour is influenced by the underlying tissue network (Hillen, 2006). Especially the extracellular matrix provides adhesion points for cells (Friedl and Broecker, 2000), and so the fibre distribution influences also the distribution of newly chosen velocities. Kinetic transport equations provide an appropriate tool to describe those velocity changes in a general way. In the following we assume that the distribution of fibres with direction $\theta \in \mathbb{S}^{n-1}$ at position $\mathbf{x}$ is known from measurements and is denoted by $q(\mathbf{x}, \theta)$ and satisfies $\int_{\mathbb{S}^{n-1}} q(\mathbf{x}, \theta)d\theta = 1$. Note that since q is a distribution over $\mathbb{S}^{n-1}$ one can choose $\frac{q(\mathbf{x},\hat{\mathbf{v}})}{\omega}$ to obtain a distribution over V for $\omega = s^{n-1}$, where $\hat{\mathbf{v}} = \frac{\mathbf{v}}{\|\mathbf{v}\|}$. We futhermore assume that $q(\mathbf{x}, \theta) = q(\mathbf{x}, -\theta)$, which means that fibres are undirected (which means that front and rear end can not be distinguished) and that cells are more likely to align to parallel tissue fibres, as shown in figure 4.4 (this behaviour has also been observed in experiments, where it has been shown that invasive glioma cells migrate along white matter fibre tracts, see (Giese and Westphal, 1996)). Under the additional assumption that cells choose their new directions independently on their previous velocity, one can simplify the general turning operator

$$\mathcal{L}p := -\lambda(\mathbf{y})p + \int_V \lambda(\mathbf{y})K(\mathbf{x}, \mathbf{v}, \mathbf{v}')p(\mathbf{v}')d\mathbf{v}'.$$

K is a distribution over V as well as $\frac{q(\mathbf{x},\hat{\mathbf{v}})}{\omega}$, hence one can identify both distributions, and set $K(\mathbf{x}, \mathbf{v}, \mathbf{v}') = \frac{q(\mathbf{x},\hat{\mathbf{v}})}{\omega}$, which corresponds to the model assumption that cells choose

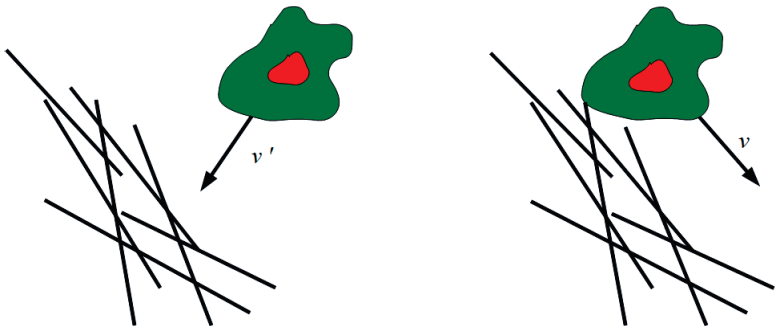

Figure 4.3.: A cell switches its velocity $\mathbf{v}'$ to its new velocity $\mathbf{v}$ due to contact guidance. The orientation of the underlying tissue structure influences the movement direction of single cells.

their new directions of movement corresponding to the underlying fibre structure. As a consequence, the operator $\mathcal{L}$ simplifies to

$$\mathcal{L}p = -\lambda(\mathbf{y})p + \lambda(\mathbf{y})\frac{q(\mathbf{x},\hat{\mathbf{v}})}{\omega}\int_V p(\mathbf{v}')d\mathbf{v}' \tag{4.6}$$

$$= -\lambda(\mathbf{y})p + \lambda(\mathbf{y})\frac{q(\mathbf{x},\hat{\mathbf{v}})}{\omega}\overline{p}. \tag{4.7}$$

This turning operator has been investigated for constant turning rates by Hillen. For more details, see (Hillen, 2006). We will now collect some properties of this operator which will be used in chapters 5 and 6.

Definition 1 (Turning operator)**.** *For each point* $(\mathbf{x},\mathbf{y})$ *the turnig operator*

$$\mathcal{L}p = -\lambda(\mathbf{y})p + \lambda(\mathbf{y})\frac{q(\mathbf{x},\hat{\mathbf{v}})}{\omega}\overline{p} \tag{4.8}$$

is a linear, compact Hilbert-Schmidt operator on $L^2_q(V)$*. Thereby,* $L^2_q(V)$ *denotes a weighted* L^2 *space with weight function* q^{-1}*.* $V = s\mathbb{S}^{n-1}$ *is the set of admissible velocities,* s *the speed of the cells.*

Lemma 1 (Kernel of the turning operator)**.** *For each point* $(t,\mathbf{x},\mathbf{y})$ *the kernel of the operator* (4.8) *can directly be computed via*

$$\mathcal{L}\psi = 0 \Leftrightarrow -\lambda(\mathbf{y})\psi + \lambda(\mathbf{y})\frac{q(\mathbf{x},\hat{\mathbf{v}})}{\omega}\overline{\psi} = 0 \tag{4.9}$$

and is hence given by

$$\psi = \frac{q(\mathbf{x},\hat{\mathbf{v}})}{\omega}\overline{\psi}, \tag{4.10}$$

where $\overline{\psi} = \int_V \psi dv$*.*

Since $\mathcal{L}$ is a compact Hilbert-Schmidt operator one can split the space $L^2_q(V)$ acording to

$$L^2_q(V) = \langle q(\mathbf{x}, \hat{\mathbf{v}}) \rangle \oplus \langle q(\mathbf{x}, \hat{\mathbf{v}}) \rangle^{\perp}, \tag{4.11}$$

where $\langle q \rangle$ denotes the span of q. On the subspace $\langle q \rangle^{\perp}$ the operator $\mathcal{L}$ is invertible, as the next lemma shows.

Lemma 2 (Inverse of the turning operator)**.** *The operator* (4.8) *is invertible on* $\langle q \rangle^{\perp}$ *and the inverse* $\mathcal{F} = \left(\mathcal{L}|_{\langle q \rangle^{\perp}} \right)^{-1}$ *is given by multiplication with factor* $-\frac{1}{\lambda}$.

More details about cellular movement can be found in the text (Hillen and Painter, 2013).

4.5. Previous work in the field

In the following we will give a brief overview on some previous important works in the field of kinetic equations. For the sake of clarity we will concentrate on the most relevant papers and will not review the full spectrum of available literature.
Kinetic models have been introduced into the field of theoretical biology around 30 years ago during the 1980s. In (Alt, 1980) Alt considered stochastic models for biased random walks of chemosensitive particles like e.g. bacteria in chemical gradient fields. He could show that under certain conditions the underlying kinetic integro-differential equation can be related to the well known Patlak-Keller-Segel model coupling an advection-diffusion-reaction equation for the density of moving cells with a parabolic reaction-diffusion equation for a chemoattractant and has originally been proposed by Patlak in 1953 (Patlak, 1953). In (Othmer et al., 1988), Othmer, Dunbar and Alt used kinetic equations of Boltzmann type for the general modelling of moving biological entities, and also random walks with resting phases have been studied in this work. It has been shown that diffusive limits of those mesoscopic kinetic models lead to advection-diffusion equations on the macroscale. Rigorous results for the drift-diffusion limit of this kinetic model have later been found by Chalub, Markowich, Perthame and Schmeiser (Chalub et al., 2004b).

Othmer and Hillen (Hillen and Othmer, 2000; Othmer and Hillen, 2002) presented some rigorous limits for kinetic equations of the form

$$\partial_t p(t, \mathbf{x}, \mathbf{v}) + \mathbf{v} \cdot \nabla p(t, \mathbf{x}, \mathbf{v}) = -\lambda p(t, \mathbf{x}, \mathbf{v}) + \lambda \int_V T(\mathbf{v}, \mathbf{v}') p(t, \mathbf{x}, \mathbf{v}') d\mathbf{v}' \tag{4.12}$$

for symmetric turning kernels. The symmetry requirement

$$\int_V T(\mathbf{v}, \mathbf{v}') d\mathbf{v}' = \int_V T(\mathbf{v}, \mathbf{v}') d\mathbf{v} = 1$$

is obviously restrictive from the viewpoint of biological modelling, and it is still an open problem to derive rigorous scaling limits without this condition.

In (Hillen, 2003) the concept of transport equations with resting phases is picked up again. The idea leads to a possibility to derive proliferative reaction terms from the mesoscopic point of view.

Kinetic models with additional internal variables of the form (4.1) have been explored by (Chalub et al., 2004a) and (Dolak and Schmeiser, 2005) for the case of bacterial chemotaxis. In both cases the authors started with a kinetic equation with an additional drift term describing processes on the microscale, and derive corresponding drift-diffusion limits. However, the turning rates do not depend on the internal variable.

Othmer and Erban developed methods to derive macroscopic limits for kinetic equations with additional drift terms which are capable to deal with turning rates depending on the internal dynamics (Erban and Othmer, 2005b,a). In this approach the first step is to look at the moments with respect to the microscopic variable in order to use then scaling arguments for the passage to a macroscopic limit equation. We will adapt these methods later and will show how to use them in a cell biological background. These results apply to concentration fields which do not vary in time and have been extended to bacteria moving in time dependent fields in (Xue and Othmer, 2009).

Bellomo (Bellomo and Bianca, 2011; Bellomo, 2008) developed generalized kinetic models including both internal variables as well as the effects of external forces. He aims to provide a general mathematical theory of complex living systems using a kinetic equation approach. The corresponding *kinetic theory of active particles* (KTAP) provides a unified modelling framework based on particle interactions.

Part III.

Modelling

5. A multiscale model for glioma growth

Inequality is the cause of all local movements.

(Leonardo Da Vinci)

Contents

Section 5.1 - 5.3 of this chapter are mostly an extended version of the publication (Engwer et al., 2013) and provides a multiscale model for glioma growth. I start in section 5.1 on the microscale with an ordinary differential equation modelling the surface receptor dynamics of a cell and introduce then in section 5.3 a mesoscopic transport equation which describes cellular movement as velocity jump process (c.f. 4.2 and 4.4). Subsequently, we perform a parabolic scaling to yield an approximating macroscopic partial differential equation of advection diffusion type as an approximation for the cell density. Section 5.4 provides a possibility to include DTI data in the model by an appropriate choice of the directional distribution q, which uses the local values of the water diffusion tensor. Additionally, we present in section 5.5 a more general scaling result for symmetric turning kernels which works without the correlation of K and q, but is as a tradeoff not capable to include DTI data.

5.1. Dynamics on the microscale: cell surface receptor dynamics

As reviewed in section 2.4, cell surface adhesion molecules as integrins play a crucial role in cellular movement. They generate traction forces and are involved in a lot of signaling and communication processes between cells and their environment.
The following model for the integrin dynamics is built on the framework proposed in

(Kelkel and Surulescu, 2011, 2012), in which additionally the fibre residuals resulting by the action of matrix degrading enzymes were playing the role of a chemoattractant for the moving cells. Hence, the present model is a simplified version of the more general setting in (Kelkel and Surulescu, 2011, 2012).

For the internal dynamics we make the following assumptions:

1. The free receptors (integrins) on the cell surface bind to the underlying ECM fibre network. This process is described on the microscale by an ordinary differential equation for the density of bound receptors $y(t)$, leading to an additional transport term in our model on the mesoscopic level.

2. The turning rate of the cells depends on the receptor state on the cell surface. It is expected to increase if many receptors are occupied, since in that case the cell will need to change more often its direction in order to 'free' itself from the too densely packed fibres surrounding it.

3. The turning behaviour of the cells can be described by a *turning kernel* dictating the choice of the new moving direction upon conditioning on the previous velocity regime and/or the integrin dynamics.

Let $Q(\mathbf{x})$ denote the volume fraction of aligned tissue, including ECM fibres. Starting from simple mass action kinetics, the integrin dynamics on the cell surface is described by the ordinary differential equation

$$\dot{y} = k^+(R_0 - y)Q - k^- y,$$

where R_0 denotes the total number of receptors on the cell (we assume it is conserved), whereas $y(t)$ gives the density of integrins bound to ECM fibres. The constants k^+ and k^- denote the reaction rates for the reversible binding of integrins to the tissue fibres. The subsequent analysis follows the idea in (Erban and Othmer, 2005a).

The steady state of this equation is $y^* = \frac{k^+ Q R_0}{k^+ Q + k^-}$. Further, let us introduce a new microscale variable $z := y^* - y$ measuring deviations from the steady state. Next consider the path of a single cell starting in $\mathbf{x}_0$ and moving with velocity $\mathbf{v}$ through a time-invariant density field $Q(\mathbf{x})$. Then with the notations $\mathbf{x} = \mathbf{x}_0 + \mathbf{v}t$ and

$$f(Q(\mathbf{x})) = \frac{k^+ Q(\mathbf{x}) R_0}{k^+ Q(\mathbf{x}) + k^-} \tag{5.1}$$

it follows that for any t

$$\frac{d}{dt} f\big(Q(\mathbf{x}_0 + \mathbf{v}t)\big) = f'(Q(\mathbf{x}_0 + \mathbf{v}t))\ \mathbf{v} \cdot \nabla Q(\mathbf{x}_0 + \mathbf{v}t)$$

and hence z satisfies the equation

$$\begin{aligned} \dot{z} &= -(k^+ Q(\mathbf{x}) + k^-)z + f'(Q(\mathbf{x}))\mathbf{v} \cdot \nabla Q(\mathbf{x}) \\ &= -(k^+ Q(\mathbf{x}) + k^-)z + \frac{k^+ k^- R_0}{(k^+ Q(\mathbf{x}) + k^-)^2}\ \mathbf{v} \cdot \nabla Q(\mathbf{x}). \end{aligned} \tag{5.2}$$

This equation can be solved explicitly for z to yield

$$z(t) = (y^* - y_0)e^{-(k^+Q+k^-)t} + (1 - e^{-(k^+Q+k^-)t})\frac{k^+k^-R_0}{(k^+Q+k^-)^3}\ \mathbf{v}\cdot\nabla Q,$$

where $y_0 = y(0)$. Hence, z is bounded as long as ∇Q it is and its sign depends on the current orientation of the cell w.r.t. the gradient of the fibre volume fraction.

For the turning rate we choose $\lambda(z) = \lambda_0 - \lambda_1 z \geq 0$, where λ_0 and λ_1 are some positive constants with $\lambda_0 \geq \lambda_1 R_0(1 - \frac{1}{K_r Q(\mathbf{x})+1})$ and $K_r := k^+/k^-$. Note that this is equivalent to considering $\lambda(y) = \lambda_0 - \lambda_1 y^* + \lambda_1 y$, which becomes indeed larger when many receptors are bound to fibres. This choice corresponds to the one proposed in (Erban and Othmer, 2005a) for the turning rate of bacteria and -after a linearization- also to that chosen in (Grünbaum, 2000). Further, observe that z involves the spatial position $\mathbf{x}$ of the cell as a parameter and there exists $z_{\max} = \max_{\mathbf{x}\in\mathbb{R}^n} z > 0$. Choosing $\lambda_1 \leq \min\left\{\frac{\lambda_0}{z_{\max}}, \sup_{\mathbf{x}} \frac{K_rQ+1}{R_0K_rQ}\right\}$ ensures that $\lambda(z) \geq 0$.

5.2. Mesoscale dynamics: cellular movement

As in equation (4.1), one can introduce the dynamics on the microscale to the mesoscopic level. With the above model for the internal dynamics equation (4.1) reads

$$\begin{aligned}\partial_t p + \nabla_{\mathbf{x}}\cdot(\mathbf{v}p) + \partial_z\left(\left(-(k^+Q+k^-)z + f'(Q(\mathbf{x}))\ \mathbf{v}\cdot\nabla Q\right)p\right) = \\ -\lambda(z)p + \lambda(z)\int_V K(\mathbf{x},\mathbf{v},\mathbf{v}')p(\mathbf{v}')d\mathbf{v}'.\end{aligned}$$

In order to simplify the following analysis, we have to make some assumptions about the cell velocity, the cellular turning rate λ and the turning kernel K.
We now focus on the case where the cell speed is constant s, hence we have $V = s\mathbb{S}^{n-1}$. Furthermore, we choose $K(\mathbf{x},\mathbf{v},\mathbf{v}') = \frac{q(\hat{\mathbf{v}})}{\omega}$ with $\omega = \int_V q(\hat{\mathbf{v}})d\mathbf{v} = s^{n-1}$ a scaling constant, as proposed in (Hillen, 2005; Painter and Hillen, 2013) according to our assumption that cells choose new directions of movement due to contact guidance (compare also with section 4.4). Recall that q denotes the directional distribution of tissue fibres, thus we also assume the tissue to be undirected. Additionally, we choose a linear turning rate $\lambda(z) = \lambda_0 - \lambda_1 z$, and have hence the transport equation

$$\begin{aligned}\partial_t p + \nabla_{\mathbf{x}}\cdot(\mathbf{v}p) - \partial_z\left(\left((k^+Q+k^-)z - f'(Q(\mathbf{x}))\ \mathbf{v}\cdot\nabla Q\right)p\right) \\ = -\lambda_0 p + \lambda_1 z p + \lambda_0\frac{q}{\omega}\int_V p(\mathbf{v}')d\mathbf{v}' - \lambda_1\frac{q}{\omega}\int_V zp(\mathbf{v}')d\mathbf{v}'.\end{aligned} \tag{5.3}$$

In the following it is our goal to derive an approximating macroscopic partial differential equation for the glioma cell density. It will be shown that the resulting equation has the form of an advection diffusion equation as equation (4.4).

We first handle the z variable by calculating momentum equations with respect to z, and then perform a parabolic scaling. First of all, introduce the following moments:

$$m(t,\mathbf{x},\mathbf{v}) = \int_Z p(t,\mathbf{x},\mathbf{v},z)dz, \qquad M(t,\mathbf{x}) = \int_V\int_Z p(t,\mathbf{x},\mathbf{v},z)dzd\mathbf{v}$$
$$m^z(t,\mathbf{x},\mathbf{v}) = \int_Z zp(t,\mathbf{x},\mathbf{v},z)dz, \qquad M^z(t,\mathbf{x}) = \int_V\int_Z zp(t,\mathbf{x},\mathbf{v},z)dzd\mathbf{v},$$

where our new domain for the internal dynamics is $Z \subseteq [y^* - R_0, y^*]$. In the following we assume the data to be compactly supported in the $(\mathbf{x},\mathbf{v},z)$-space, which allows to perform the subsequent calculations.

Integration of equation (5.3) with respect to z yields

$$\partial_t m + \mathbf{v}\cdot\nabla m = -\lambda_0 m + \lambda_1 m^z + \lambda_0\frac{q}{\omega}M - \lambda_1\frac{q}{\omega}M^z. \tag{5.4}$$

Multiply (5.3) by z and integrate again to obtain

$$\partial_t m^z + \mathbf{v}\cdot\nabla m^z - \int_Z z\cdot\left[\partial_z\left(\left[(k^+Q+k^-)z - f'(Q(\mathbf{x}))\ \mathbf{v}\cdot\nabla Q\right]p\right)\right]dz$$
$$= -\lambda_0 m^z + \lambda_1 m^{zz} + \lambda_0\frac{q}{\omega}M^z - \lambda_1\frac{q}{\omega}M^{zz},$$

with

$$m^{zz}(t,\mathbf{x},\mathbf{v}) = \int_Z z^2 p(t,\mathbf{x},\mathbf{v},z)dz \quad \text{and} \quad M^{zz}(\mathbf{x},t) = \int_V\int_Z z^2 p(t,\mathbf{x},\mathbf{v},z)dzd\mathbf{v}.$$

Assume the internal dynamics equilibrates rapidly, so that the system is always close to the steady state. Hence, we neglect the second-order moments in z, so that the last equation becomes

$$\partial_t m^z + \mathbf{v}\cdot\nabla m^z = -(k^+Q+k^-)m^z + f'(Q(\mathbf{x}))\ \mathbf{v}\cdot\nabla Q\ m - \lambda_0 m^z + \lambda_0\frac{q}{\omega}M^z. \tag{5.5}$$

We will now work with equations (5.4) and (5.5) and perform a parabolic scaling of space and time.

5.3. From mesoscale to macroscale: formal diffusion approximation

In order to perform a parabolic scaling, we rescale the time and space variables by a dimensionless scaling parameter ε. We scale the time quatratically, $\hat{t} = \varepsilon^2 t$, and $\mathbf{x}$ linearly $\hat{\mathbf{x}} = \varepsilon\mathbf{x}$, then drop the hats on $\mathbf{x}$, t. As explained in section 4.2, this allows to

change the viewpoint of observation of our system and makes a simplified description possible. After scaling equations (5.4) and (5.5) we obtain

$$\varepsilon^2\partial_t m + \varepsilon\mathbf{v}\cdot\nabla m = -\lambda_0 m + \lambda_1 m^z + \lambda_0\frac{q}{\omega}M - \lambda_1\frac{q}{\omega}M^z \tag{5.6}$$

$$\varepsilon^2\partial_t m^z + \varepsilon\mathbf{v}\cdot\nabla m^z = -(k^+Q + k^-)m^z + \varepsilon f'(Q(\mathbf{x}))\ \mathbf{v}\cdot\nabla Q\ m - \lambda_0 m^z + \lambda_0\frac{q}{\omega}M^z. \tag{5.7}$$

As in (Hillen, 2006), we use Hilbert expansions for m, M, m^z and M^z of the form

$$\begin{aligned} m &= m_0 + \varepsilon m_1 + \varepsilon^2 m_2 + \dots \\ M &= M_0 + \varepsilon M_1 + \varepsilon^2 M_2 + \dots \\ m^z &= m_0^z + \varepsilon m_1^z + \varepsilon^2 m_2^z + \dots \\ M^z &= M_0^z + \varepsilon M_1^z + \varepsilon^2 M_2^z + \dots \end{aligned}$$

After plugging these expansions into equations (5.6) and (5.7) one can compare terms of equal order in ε of each side and collect terms of equal order:

ε^0:

$$0 = -\lambda_0 m_0 + \lambda_1 m_0^z + \lambda_0\frac{q}{\omega}M_0 - \lambda_1\frac{q}{\omega}M_0^z \tag{5.8}$$

$$0 = -(k^+Q + k^-)m_0^z - \lambda_0 m_0^z + \lambda_0\frac{q}{\omega}M_0^z. \tag{5.9}$$

ε^1:

$$\mathbf{v}\cdot\nabla m_0 = -\lambda_0 m_1 + \lambda_1 m_1^z + \lambda_0\frac{q}{\omega}M_1 - \lambda_1\frac{q}{\omega}M_1^z \tag{5.10}$$

$$\mathbf{v}\cdot\nabla m_0^z = -(k^+Q + k^-)m_1^z + f'(Q(\mathbf{x}))\ \mathbf{v}\cdot\nabla Q\ m_0 - \lambda_0 m_1^z + \lambda_0\frac{q}{\omega}M_1^z. \tag{5.11}$$

ε^2:

$$\partial_t m_0 + \mathbf{v}\cdot\nabla m_1 = -\lambda_0 m_2 + \lambda_1 m_2^z + \lambda_0\frac{q}{\omega}M_2 - \lambda_1\frac{q}{\omega}M_2^z. \tag{5.12}$$

We are now interested to derive an evolution equation for the macroscopic quantity M_0. Hence, we have to find explicite forms of the other moments which depend just on this quantity. This is possible by the following 'backward solving' strategy which will be performed below.

By integrating with respect to $\mathbf{v}$ it follows from (5.8)-(5.12):

ε^0:

$$\begin{aligned} &\text{From eq.(5.9)}: \quad M_0^z = 0,\ m_0^z = 0. \\ &\text{From eq.(5.8)}: \quad m_0 = \frac{q}{\omega}M_0. \end{aligned}$$

ε^1 (recall the assumption of undirected tissue):

$$\begin{aligned}
&\text{From eq.(5.11)}: \quad M_1^z = 0, \quad m_1^z = (k^+Q + k^- + \lambda_0)^{-1}\, m_0\, f'(Q(\mathbf{x}))\, \mathbf{v}\cdot\nabla Q(\mathbf{x}) \\
&\text{From eq.(5.10)}: \quad M_1 = 0,\ m_1 = -\frac{1}{\lambda_0}\left(\mathbf{v}\cdot\nabla m_0 - \lambda_1 m_1^z\right).
\end{aligned}$$

We used here the properties of the operator $\mathcal{L}[\lambda_0](m_1) := -\lambda_0 m_1 + \lambda_0 \frac{q}{\omega} M_1$ defined on $L^2_q(V)$ which have been collected in lemma 1 and lemma 2 in section 4.4. For the kernel of $\mathcal{L}[\lambda_0]$ we have

$$\mathcal{L}[\lambda_0](m_1) = 0 \qquad \Longleftrightarrow \qquad m_1 = \frac{\hat{q}(\hat{\mathbf{v}})}{\omega} M_1.$$

The mapping $\mathcal{L}[\lambda_0]$ is a compact Hilbert-Schmidt operator (see also (Hillen and Othmer, 2000)) whose kernel is given by the linear space $\langle q\rangle$, denoting the subspace of $L^2_q(V)$ spanned by q.

Then (see again (Hillen and Othmer, 2000)) on $\langle q\rangle^\perp$ we can find the pseudo-inverse of $\mathcal{L}[\lambda_0]$. Consider for this a given function $\psi \in \langle q\rangle^\perp$ and solve

$$\mathcal{L}[\lambda_0](m_1) = \psi.$$

Since $m_1 \in \langle q\rangle^\perp$ we have $M_1 = 0$ and the rest follows immediately.

Now, we can collect known expressions and write them w.r.t. M_0 and find

$$\begin{aligned}
m_0 &= \frac{q}{\omega} M_0, \\
m_1^z &= \left(k^+Q + k^- + \lambda_0\right)^{-1} f'(Q(\mathbf{x}))\, \mathbf{v}\cdot\nabla Q \frac{q}{\omega} M_0, \\
m_1 &= -\frac{1}{\lambda_0}\left[\mathbf{v}\cdot\nabla\left(\frac{q}{\omega}M_0\right) - \lambda_1\left(k^+Q + k^- + \lambda_0\right)^{-1} f'(Q(\mathbf{x}))\, \mathbf{v}\cdot\nabla Q\frac{q}{\omega}M_0\right].
\end{aligned}$$

In order to obtain an evolution equation we integrate equation (5.12) w.r.t. $\mathbf{v}$ and obtain

$$\int_V \left(\partial_t \frac{q}{\omega} M_0 + \mathbf{v}\cdot\nabla m_1\right) d\mathbf{v} = 0. \tag{5.13}$$

We have already found an explicit expression for m_1 in terms of the observation quantity M_0, and plug this term now into equation (5.13), which gives imediately

$$\partial_t M_0 + \int_V \mathbf{v}\cdot\nabla\left[-\frac{1}{\lambda_0}\left(\mathbf{v}\cdot\nabla\left(\frac{q}{\omega}M_0\right) - \lambda_1\left(k^+Q + k^- + \lambda_0\right)^{-1} f'(Q(\mathbf{x}))\, \mathbf{v}\cdot\nabla Q\frac{q}{\omega}M_0\right)\right] d\mathbf{v} = 0,$$

what is equivalent to

$$\begin{aligned}
\partial_t M_0 &- \frac{1}{\lambda_0}\int_V \mathbf{v}\cdot\nabla\left(\mathbf{v}\cdot\nabla\left(\frac{q}{\omega}M_0\right)\right) d\mathbf{v} \\
&+ \frac{\lambda_1}{\lambda_0}\int_V \mathbf{v}\cdot\nabla\left((k^+Q + k^- + \lambda_0)^{-1} f'(Q(\mathbf{x}))\, \mathbf{v}\cdot\nabla Q\, \frac{q}{\omega}M_0\right) d\mathbf{v} = 0.
\end{aligned}$$

Now, we rearrange the expressions to bring this equation into a classical advection-diffusion form and end up with an evolution equation for M_0, given by

$$\partial_t M_0 - \frac{1}{\lambda_0}\nabla\cdot\left(\int_V \mathbf{v}\otimes\mathbf{v}\nabla\frac{q}{\omega}d\mathbf{v}\ M_0\right) - \frac{1}{\lambda_0}\nabla\cdot\left(\int_V \mathbf{v}\otimes\mathbf{v}\frac{q}{\omega}d\mathbf{v}\ \nabla M_0\right) + \frac{\lambda_1}{\lambda_0}\int_V \mathbf{v}\cdot\nabla\left((k^+Q+k^-+\lambda_0)^{-1}f'(Q(\mathbf{x}))\ \mathbf{v}\cdot\nabla Q\ \frac{q}{\omega}\ M_0\right)d\mathbf{v} = 0.$$

This leads to the evolution equation

$$\partial_t M_0 - \nabla\cdot(\mathbb{D}_T(\mathbf{x})\nabla M_0) + \nabla\cdot([g(Q(\mathbf{x}))\mathbb{D}_T(\mathbf{x})\nabla Q(\mathbf{x}) - \mathbf{u}(\mathbf{x})]\ M_0) = 0 \tag{5.14}$$

with the tumor diffusion tensor

$$\mathbb{D}_T(\mathbf{x}) = \frac{1}{\lambda_0\omega}\int_V \mathbf{v}\otimes\mathbf{v}q\,d\mathbf{v}, \tag{5.15}$$

a function $g(Q)$ representing the influence of the receptor dynamics given by

$$g(Q(\mathbf{x})) = \lambda_1(k^+Q(\mathbf{x})+k^-+\lambda_0)^{-1}f'(Q(\mathbf{x})), \tag{5.16}$$

and a tumor drift velocity which can be written as

$$\mathbf{u}(\mathbf{x}) = \frac{1}{\lambda_0\omega}\int_V \mathbf{v}\otimes\mathbf{v}\nabla q\,d\mathbf{v}. \tag{5.17}$$

Obviously, the receptor dynamics on the microscale leads to an additional advective term on the macroscale, which has the direction of the aligned tissue gradient ∇Q. This makes sense from the biological point of view, since cellular movement has usually a haptotactic component. Notice, that the distribution function q still has to be determined. We will consider this point in the next section.

5.4. Determination of the coefficients

5.4.1. Choice of the fibre distribution function

In order to determine an explicit form for the coefficients $\mathbb{D}_T(\mathbf{x})$ and $\mathbf{u}(\mathbf{x})$ we need to characterize the fibre distribution $q(\mathbf{x},\theta)$. As already mentioned, the aim is to embed DTI data into our model equations. Thereby, a possible choice can be

$$q(\mathbf{x},\theta) = \frac{n}{|\mathbb{S}^{n-1}|\,\mathrm{tr}\,\mathbb{D}_W(\mathbf{x})}\theta^t\mathbb{D}_W(\mathbf{x})\theta. \tag{5.18}$$

The *water diffusion tensor* $\mathbb{D}_W(\mathbf{x})$ can be obtained for each voxel $\mathbf{x}$ by measurements, hence the above formula allows for computing the fibre distribution function for each voxel. The tumor diffusion tensor can be calculated explicitly, as we show below. In (Painter and Hillen, 2013) it has been argued that this choice for the relationship between

fibre orientation and water diffusion data encompasses some significant shortcomings. Hence, instead of (5.18), a bimodal von Mises-Fisher distribution of the form

$$q(\mathbf{x},\theta) = \frac{k(\mathbf{x})}{8\pi \sinh(k(\mathbf{x}))} \left(e^{k\phi\cdot\theta} + e^{-k\phi\cdot\theta}\right) \tag{5.19}$$

has been chosen, with $k(\mathbf{x}) = \kappa \cdot \mathrm{FA}(\mathbf{x})$, where $\mathrm{FA}(\mathbf{x})$ denotes the fractional anisotropy and ϕ represents the leading eigenvector of the diffusion tensor for each voxel. In this approach, the concentration parameter κ has to be determined[1] and it can be interpreted as the sensitivity of the cells to the orientation of the underlying fibre structure.

In order to avoid introducing more parameters for which the identification is still unclear in practice, we will keep the form (5.18) for q. However, in chapter 9.1.3 we will also consider the alternative fibre distribution (5.19) and compare the results obtained for both choices.

5.4.2. The peanut distribution

In this section we will show how to calculate the explicit form of q for the peanut distribution (5.18). The following lemma is used a number of times to calculate specific integral moments of θ:

Lemma 3 (Hillen (2005) (Hillen, 2005)). *1. If $k \in \mathbb{N}$ is odd, then*

$$\int_{\mathbb{S}^{n-1}} \theta^{i_1} \cdots \theta^{i_k} \, d\theta = 0.$$

2. If $k \in \mathbb{N}$ is even, then

$$\int_{\mathbb{S}^{n-1}} \theta^{i_1} \cdots \theta^{i_k} \, d\theta = c_k \left(\sum_{\mathcal{P}(i_1,\ldots,i_k)} \delta^{i_{j_1} i_{j_2}} \ldots \delta^{i_{j_{k-1}} i_{j_k}} \right),$$

where the set

$$\mathcal{P}(i_1,\ldots,i_k) := \{\big((i_{j_1}, i_{j_2}), \ldots, (i_{j_{k-1}} i_{j_k})\big) : \{j_1,\ldots,j_k\} = \{1,\ldots,k\}\}$$

is the set of all pairs of indices. The constant c_k is given by

$$c_0 = |\mathbb{S}^{n-1}|, \quad c_2 = \frac{|\mathbb{S}^{n-1}|}{n} \quad \text{and } c_k = \frac{c_{k-2}}{k-2+n} \text{ for } k \geq 4.$$

[1] the larger the value of κ, the higher the concentration of distribution around the mean direction

With this tool its is now possible to determine the tumor diffusion tensor (see also (Painter and Hillen, 2013)).

$$
\begin{aligned}
\lambda_0\omega\mathbb{D}_T(\mathbf{x}) &= \frac{ns^{n+1}}{\omega_n \mathrm{tr}\,\mathbb{D}_W(\mathbf{x})}\int_{\mathbb{S}^{n-1}}\theta\theta^t\theta^t\mathbb{D}_W(\mathbf{x})\theta d\theta \\
&= \frac{ns^{n+1}}{\omega_n \mathrm{tr}\,\mathbb{D}_W(\mathbf{x})}\left(\int_{\mathbb{S}^{n-1}}\left(\theta^i\theta^j\sum_{k,l=1}^{n} d_w^{kl}(\mathbf{x})\theta^k\theta^l\right)d\theta\right)_{(1\le i,j,n)} \\
&= \frac{ns^{n+1}}{\omega_n \mathrm{tr}\,\mathbb{D}_W(\mathbf{x})}\left(\sum_{k,l=1}^{n}\left(d_w^{kl}(\mathbf{x})\int_{\mathbb{S}^{n-1}}\theta^i\theta^j\theta^k\theta^l d\theta\right)\right)_{(1\le i,j,n)} \\
&= \frac{ns^{n+1}}{\omega_n \mathrm{tr}\,\mathbb{D}_W(\mathbf{x})}\left(\sum_{k,l=1}^{n} d_w^{kl}(\mathbf{x})\left(\frac{\omega_n}{n(n+2)}\left(\delta^{ij}\delta^{kl}+\delta^{ik}\delta^{jl}+\delta^{il}\delta^{jk}\right)\right)\right)_{(1\le i,j,n)} \\
&\quad \text{(by using Lemma 3} \\
&= \frac{s^{n+1}}{(n+2)\mathrm{tr}\,\mathbb{D}_W(\mathbf{x})}\left(\sum_{k,l=1}^{n} d_w^{kl}(\mathbf{x})\delta^{ij}\delta^{kl}+\sum_{k,l=1}^{n} d_w^{kl}(\mathbf{x})\delta^{ik}\delta^{jl}+\sum_{kl=1}^{n} d_w^{kl}(\mathbf{x})\delta^{il}\delta^{jk}\right)_{(1\le i,j,n)} \\
&= \frac{s^{n+1}}{(n+2)\mathrm{tr}\,\mathbb{D}_W(\mathbf{x})}(\mathrm{tr}\,\mathbb{D}_W(\mathbf{x})\cdot\mathbb{I}_n+\mathbb{D}_W(\mathbf{x})+\mathbb{D}_W(\mathbf{x})) \\
&= \frac{s^{n+1}}{(n+2)}\left(\mathbb{I}_n+2\frac{\mathbb{D}_W(\mathbf{x})}{\mathrm{tr}\,\mathbb{D}_W(\mathbf{x})}\right).
\end{aligned}
$$

with constants $\omega_n = |\mathbb{S}^{n-1}|$. Hence we obtain for the tumor diffusion tensor the expression

$$
\mathbb{D}_T(\mathbf{x}) = \frac{s^2}{\lambda_0(n+2)}\left(\mathbb{I}_n+2\frac{\mathbb{D}_W(\mathbf{x})}{\mathrm{tr}\,\mathbb{D}_W(\mathbf{x})}\right). \tag{5.20}
$$

Analogously, we can calculate the drift velocity (5.17) using the expression (5.18) for q again. Plugging the expression (5.18) in equation (5.17) yields

$$
\mathbf{u}(\mathbf{x}) = \frac{s^{n+1}}{\lambda_0\omega}\frac{n}{\omega_n}\int_{\mathbb{S}^{n-1}}\theta\theta^t\nabla\left(\frac{1}{\mathrm{tr}\,\mathbb{D}_W(\mathbf{x})}\theta^t\mathbb{D}_W(\mathbf{x})\theta\right)d\theta.
$$

First, we have

$$\begin{aligned}
&\nabla_{\mathbf{x}}\left(\frac{1}{\operatorname{tr}\mathbb{D}_W(\mathbf{x})}\theta^T\mathbb{D}_W(\mathbf{x})\theta\right)\\
&=\nabla_{\mathbf{x}}\left(\frac{1}{\operatorname{tr}\mathbb{D}_W(\mathbf{x})}\right)\theta^T\mathbb{D}_W(\mathbf{x})\theta+\frac{1}{\operatorname{tr}\mathbb{D}_W(\mathbf{x})}\nabla_{\mathbf{x}}\left(\theta^T\mathbb{D}_W(\mathbf{x})\theta\right)\\
&=-\nabla_{\mathbf{x}}(\operatorname{tr}\mathbb{D}_W(\mathbf{x}))\cdot(\operatorname{tr}\mathbb{D}_W(\mathbf{x}))^{-2}\theta^T\mathbb{D}_W(\mathbf{x})\theta+(\operatorname{tr}\mathbb{D}_W(\mathbf{x}))^{-1}\cdot\nabla_{\mathbf{x}}\left(\sum_{k,l=1}^n d_w^{kl}(\mathbf{x})\theta^k\theta^l\right)\\
&=\frac{-1}{\operatorname{tr}\mathbb{D}_W(\mathbf{x})}\left[\begin{pmatrix}\partial_{x_1}(\operatorname{tr}\mathbb{D}_W(\mathbf{x}))\\ \vdots\\ \partial_{x_n}(\operatorname{tr}\mathbb{D}_W(\mathbf{x}))\end{pmatrix}(\operatorname{tr}\mathbb{D}_W(\mathbf{x}))^{-1}\theta^T\mathbb{D}_W(\mathbf{x})\theta-\begin{pmatrix}\sum_{k,l=1}^n\partial_{x_1}d_w^{kl}(\mathbf{x})\theta^k\theta^l\\ \vdots\\ \sum_{k,l=1}^n\partial_{x_n}d_w^{kl}(\mathbf{x})\theta^k\theta^l\end{pmatrix}\right]
\end{aligned}$$

So this is a vector $\gamma(\mathbf{x})=(\gamma_1(\mathbf{x}),\dots,\gamma_n(\mathbf{x}))^t$ with

$$\gamma_i(\mathbf{x})=\frac{-1}{(\operatorname{tr}\mathbb{D}_W(\mathbf{x}))^2}\partial_{x_i}(\operatorname{tr}\mathbb{D}_W(\mathbf{x}))\ \theta^T\mathbb{D}_W(\mathbf{x})\theta+\frac{1}{\operatorname{tr}\mathbb{D}_W(\mathbf{x})}\sum_{k,l=1}^n\partial_{x_i}d_w^{kl}(\mathbf{x})\theta^k\theta^l.$$

From this observe that

$$\int_V\theta\theta^t\nabla\left(\frac{1}{\operatorname{tr}\mathbb{D}_W(\mathbf{x})}\theta^t\mathbb{D}_W(\mathbf{x})\theta\right)d\theta$$

is a vector $\alpha(\mathbf{x})=\big(\alpha_1(\mathbf{x}),\dots,\alpha_n(\mathbf{x})\big)^t$ with components

$$\begin{aligned}
\alpha_c(\mathbf{x})&=\int_V\sum_{d=1}^n\theta^c\theta^d\Bigg(\frac{-1}{(\operatorname{tr}\mathbb{D}_W(\mathbf{x}))^2}\partial_{x_d}\big(\operatorname{tr}\mathbb{D}_W(\mathbf{x})\big)\sum_{a,b=1}^n\theta^a\theta^b d_w^{ab}(\mathbf{x})\\
&\quad+\frac{1}{\operatorname{tr}\mathbb{D}_W(\mathbf{x})}\sum_{a,b=1}^n\partial_{x_d}d_w^{ab}(\mathbf{x})\theta^a\theta^b\Bigg)d\theta\\
&=-\frac{1}{(\operatorname{tr}\mathbb{D}_W(\mathbf{x}))^2}\Bigg(\sum_{d,a,b=1}^n\partial_{x_d}\big(\operatorname{tr}\mathbb{D}_W(\mathbf{x})\big)d_w^{ab}(\mathbf{x})\int_V\theta^c\theta^d\theta^a\theta^b d\theta\Bigg)\\
&\quad+\frac{1}{\operatorname{tr}\mathbb{D}_W(\mathbf{x})}\Bigg(\sum_{d,a,b=1}^n\partial_{x_d}d_w^{ab}(\mathbf{x})\int_V\theta^c\theta^d\theta^a\theta^b d\theta\Bigg)\\
&:=\alpha_c^1(\mathbf{x})+\alpha_c^2(\mathbf{x}).
\end{aligned}$$

Now we evaluate the two terms above. For this recall that

$$\int_V\theta^c\theta^d\theta^a\theta^b d\theta=\frac{\omega_n}{n(n+2)}\big(\delta^{cd}\delta^{ab}+\delta^{ca}\delta^{db}+\delta^{cb}\delta^{da}\big),$$

hence

$$\begin{aligned}
\alpha_c^1(\mathbf{x}) &= -\frac{1}{(\operatorname{tr}\mathbb{D}_W(\mathbf{x}))^2}\frac{\omega_n}{n(n+2)}\Bigg(\sum_{d,a,b=1}^{n}\partial_{x_d}\big(\operatorname{tr}\mathbb{D}_W(\mathbf{x})\big)d_w^{ab}(\mathbf{x})\big(\delta^{cd}\delta^{ab}+\delta^{ca}\delta^{db}+\delta^{cb}\delta^{da}\big)\Bigg)\\
&= -\frac{1}{(\operatorname{tr}\mathbb{D}_W(\mathbf{x}))^2}\frac{\omega_n}{n(n+2)}\Bigg(\sum_{d,a,b=1}^{n}\partial_{x_d}\big(\operatorname{tr}\mathbb{D}_W(\mathbf{x})\big)d_w^{ab}(\mathbf{x})\delta^{cd}\delta^{ab}\\
&+\sum_{d,a,b=1}^{n}\partial_{x_d}\big(\operatorname{tr}\mathbb{D}_W(\mathbf{x})\big)d_w^{ab}(\mathbf{x})\delta^{ca}\delta^{db}+\sum_{d,a,b=1}^{n}\partial_{x_d}\big(\operatorname{tr}\mathbb{D}_W(\mathbf{x})\big)d_w^{ab}(\mathbf{x})\delta^{cb}\delta^{da}\Bigg)\\
&= -\frac{1}{(\operatorname{tr}\mathbb{D}_W(\mathbf{x}))^2}\frac{\omega_n}{n(n+2)}\Bigg(\sum_{d=1}^{n}\partial_{x_d}\big(\operatorname{tr}\mathbb{D}_W(\mathbf{x})\big)\delta^{cd}\operatorname{tr}\mathbb{D}_W(\mathbf{x})\\
&+\sum_{d=1}^{n}\partial_{x_d}\big(\operatorname{tr}\mathbb{D}_W(\mathbf{x})\big)d_w^{cd}(\mathbf{x})+\sum_{d=1}^{n}\partial_{x_d}\big(\operatorname{tr}\mathbb{D}_W(\mathbf{x})\big)d_w^{dc}(\mathbf{x})\Bigg).
\end{aligned}$$

Hence, we obtain for the vector $\alpha^1(\mathbf{x})$:

$$-\frac{1}{(\operatorname{tr}\mathbb{D}_W(\mathbf{x}))^2}\frac{\omega_n}{n(n+2)}\Bigg(\operatorname{tr}\mathbb{D}_W(\mathbf{x})\mathbb{I}_n+2\mathbb{D}_W(\mathbf{x})\Bigg)\cdot\nabla\operatorname{tr}\mathbb{D}_{\mathbf{W}}(\mathbf{x}).$$

Analogously, we obtain for $\alpha_c^2(\mathbf{x})$:

$$\begin{aligned}
\alpha_c^2(\mathbf{x}) &= \frac{1}{\operatorname{tr}\mathbb{D}_W(\mathbf{x})}\frac{\omega_n}{n(n+2)}\Bigg(\sum_{d,a,b=1}^{n}\partial_{x_d}d_w^{ab}(\mathbf{x})\big(\delta^{cd}\delta^{ab}+\delta^{ca}\delta^{db}+\delta^{cb}\delta^{da}\big)\Bigg)\\
&= \frac{1}{\operatorname{tr}\mathbb{D}_W(\mathbf{x})}\frac{\omega_n}{n(n+2)}\Bigg(\sum_{d,a,b=1}^{n}\partial_{x_d}d_w^{ab}(\mathbf{x})\delta^{cd}\delta^{ab}+\sum_{d,a,b=1}^{n}\partial_{x_d}d_w^{ab}(\mathbf{x})\delta^{ca}\delta^{db}+\sum_{d,a,b=1}^{n}\partial_{x_d}d_w^{ab}(\mathbf{x})\delta^{cb}\delta^{da}\Bigg)\\
&= \frac{1}{\operatorname{tr}\mathbb{D}_W(\mathbf{x})}\frac{\omega_n}{n(n+2)}\Bigg(\sum_{a=1}^{n}\partial_{x_c}d_w^{aa}(\mathbf{x})+\sum_{d=1}^{n}\partial_{x_d}d_w^{cd}(\mathbf{x})+\sum_{d=1}^{n}\partial_{x_d}d_w^{dc}(\mathbf{x})\Bigg),
\end{aligned}$$

and this means

$$\alpha^2(\mathbf{x}) = \frac{1}{\operatorname{tr}\mathbb{D}_W(\mathbf{x})}\frac{\omega_n}{n(n+2)}\Bigg(\nabla\operatorname{tr}\mathbb{D}_W(\mathbf{x})+2\nabla\cdot\mathbb{D}_W(\mathbf{x})\Bigg).$$

Altogether, this yields

$$\begin{aligned}
\mathbf{u}(\mathbf{x}) &= \frac{s^2}{\lambda_0(n+2)}\Bigg[-\frac{1}{(\operatorname{tr}\mathbb{D}_W(\mathbf{x}))^2}\Bigg(\operatorname{tr}\mathbb{D}_W(\mathbf{x})\mathbb{I}_n+2\mathbb{D}_W(\mathbf{x})\Bigg)\cdot\nabla\operatorname{tr}\mathbb{D}_{\mathbf{W}}(\mathbf{x}) \qquad (5.21)\\
&+\frac{1}{\operatorname{tr}\mathbb{D}_W(\mathbf{x})}\Bigg(\nabla\operatorname{tr}\mathbb{D}_W(\mathbf{x})+2\nabla\cdot\mathbb{D}_W(\mathbf{x})\Bigg)\Bigg]\\
&= \frac{2s^2}{\lambda_0(n+2)}\left(\frac{\nabla\cdot\mathbb{D}_W(\mathbf{x})}{\operatorname{tr}\mathbb{D}_W(\mathbf{x})}-\frac{\mathbb{D}_W(\mathbf{x})\cdot\nabla\operatorname{tr}\mathbb{D}_{\mathbf{W}}(\mathbf{x})}{(\operatorname{tr}\mathbb{D}_W(\mathbf{x}))^{\mathbf{2}}}\right). \qquad (5.22)
\end{aligned}$$

With these explicit forms for the tumor diffusion tensor and its drift velocity, numerical simulations for equation (5.14) can be performed, what will be done in part IV.

5.4.3. Von Mises-Fisher distribution

In (Painter and Hillen, 2013) the authors argued that the peanut distribution encompasses some significant shortcomings and proposed a bimodal von Mises-Fisher distribution of the form

$$q(\mathbf{x},\theta) = \frac{\delta}{4\pi} + (1-\delta)\frac{k(\mathbf{x})}{8\pi\sinh(k(\mathbf{x}))}\left(e^{k\phi\cdot\theta} + e^{-k\phi\cdot\theta}\right) \tag{5.23}$$

instead, where the parameter $\delta \in [0,1]$ is related to inherent random turning (uniform turning kernel).
In three spatial dimensions, this leads to the tumor tensor

$$\begin{aligned}\mathbb{D}_T(\mathbf{x}) = \frac{s^2}{3\lambda_0}\Bigg[&\left(\delta + (1-\delta)\left(\frac{\coth k(\mathbf{x})}{k(\mathbf{x})} - \frac{1}{k(\mathbf{x})^2}\right)\right)\mathbb{I} \\ &+ (1-\delta)\left(1 - \frac{3\coth k(\mathbf{x})}{k(\mathbf{x})} + \frac{3}{k(\mathbf{x})^2}\right)\phi\phi^t\Bigg],\end{aligned}$$

where k and ϕ have been defined above. The corresponding drift correction term reads

$$\begin{aligned}\mathbf{u}(\mathbf{x}) = (1-\delta)\Bigg[&\nabla\left(\frac{\coth(k(\mathbf{x}))}{k(\mathbf{x})} - \frac{1}{k(\mathbf{x})^2}\right)\mathbb{I} - \left(\nabla\left(\frac{3\coth(k(\mathbf{x}))}{k(\mathbf{x})} + \frac{3}{k(\mathbf{x})2}\right)\phi\phi^t\right) \\ &+ \left(1 - \frac{3\coth(k(\mathbf{x}))}{k(\mathbf{x})} + \frac{3}{k(\mathbf{x})^2}\right)\nabla\cdot\phi\phi^t\Bigg].\end{aligned} \tag{5.24}$$

Recall, that in (Painter and Hillen, 2013) k has been proposed to be $k(\mathbf{x}) = \kappa\,\mathrm{FA}(\mathbf{x})$, where the constant $\kappa > 0$ is a measure for the sensitiveity of the cells to environmental clues. It is interesting to look at two limits for the tumor diffusion tensor: first, what happens in highly anisotrope regions with FA $\neq 0$ for really large sensitivity values $\kappa \to \infty$ and hence $k \to \infty$, and second, what happens in isotrope areas, where we have FA $\to 0$ and hence $k \to 0$. For the first case observe that

$$\lim_{k\to\infty}\left(\frac{\coth k}{k} - \frac{1}{k^2}\right) = 0$$

and

$$\lim_{k\to\infty}\left(1 - \frac{3\coth k}{k} + \frac{3}{k^2}\right) = 1.$$

This leads to the diffusion tensor

$$\mathbb{D}_T(\mathbf{x}) = \frac{s^2}{3\lambda_0}\left(\delta\mathbb{I} + (1-\delta)\phi\phi^t\right).$$

Since the parameter δ is typically very small, the influence of the isotrope part is neglegible and the influence of the $\phi\phi^t$ term is maximal. For the second case consider the limtis

$$\lim_{k\to 0}\left(\frac{\coth k}{k} - \frac{1}{k^2}\right) = \frac{1}{3}$$

and

$$\lim_{k\to 0}\left(1-\frac{3\coth k}{k}+\frac{3}{k^2}\right)=0$$

to obtain the tensor

$$\mathbb{D}_T(\mathbf{x})=\frac{s^2}{3\lambda_0}\left(\frac{1}{3}+\frac{2}{3}\delta\right)\mathbb{I}.$$

In this case the anisotropic part vanishes and the tumor diffusion tensor becomes isotrope and even constant since there is no spatial dependency.

5.5. A more general scaling result for symmetric turning kernels

The analysis in the previous sections was based on a relationship between the turning behaviour of the cells and the directional distribution of the underlying fibre network. This led to the choice $K(\mathbf{x},\mathbf{v},\mathbf{v}')=\frac{q(x,\hat{\mathbf{v}})}{\omega}$ for the turning kernel, which was independent of the incoming velocity $\mathbf{v}'$. In this section, I will present a more general result for symmetric turning kernels which works without this assumption. Though, this approach is not capable to involve DTI data and hence more theoretically interesting. Furthermore, it is in general not possible to compute explicit expressions for the inverse of the turning operator, and so one has to employ some arguments from functional analysis, respectively operator theory.
We start again with an evolution equation for the cell density $p(t,x,v,z)$ of the form

$$\partial_t p+\nabla_{\mathbf{x}}\cdot(\mathbf{v}p)+\nabla_z\cdot(Gp)=-\lambda(z)p+\int_V\lambda(z)K(\mathbf{x},\mathbf{v},\mathbf{v}')p(\mathbf{v}')d\mathbf{v}'. \tag{5.25}$$

Employing the same model and analysis for the dynamics on the microscale as in section 5.1, we obtain the kinetic equation

$$\partial_t p+\nabla\cdot(\mathbf{v}p)+\partial_z\left(\left(-(k^+Q+k^-)z-f'(Q(\mathbf{x}))\nabla Q\cdot\mathbf{v}\right)p\right)=\mathcal{L}[\lambda(z)]p. \tag{5.26}$$

For a positive turning rate λ we defined the *turning operator* $\mathcal{L}$ by

$$\mathcal{L}[\lambda]p=-\lambda p+\lambda\int_V K(\mathbf{v},\mathbf{v}')p(\mathbf{v}')d\mathbf{v}'=\lambda(-\mathcal{I}+\mathcal{T})p. \tag{5.27}$$

Choosing again a linear turning rate of the form $\lambda(z)=\lambda_0-\lambda_1 z$, one obtains the equation

$$\begin{aligned}\partial_t p+\nabla\cdot(\mathbf{v}p)+\partial_z\left(\left(-(k^+Q+k^-)z-f'(Q(\mathbf{x}))\mathbf{v}\cdot\nabla Q\right)p\right)&\\ =-\lambda_0 p+\lambda_0\int_V K(\mathbf{v},\mathbf{v}')p(\mathbf{v}')d\mathbf{v}'+\lambda_1 zp-\lambda_1\int_V K(\mathbf{v},\mathbf{v}')zp(\mathbf{v}')d\mathbf{v}'&\\ =\mathcal{L}[\lambda_0]p-\mathcal{L}[\lambda_1]zp&\qquad(5.28)\\ &\qquad(5.29)\end{aligned}$$

We follow now the strategy presented in section 5.3, and compute as a first step the z moments in order to prepare our system for a parabolic scaling as a next step. Introduce the following moments:

$$m(t,\mathbf{x},\mathbf{v}) = \int_Z p(t,\mathbf{x},\mathbf{v},z)dz, \qquad M(t,\mathbf{x}) = \int_V\int_Z p(t,\mathbf{x},\mathbf{v},z)dzd\mathbf{v}$$
$$m^z(t,\mathbf{x},\mathbf{v}) = \int_Z zp(t,\mathbf{x},\mathbf{v},z)dz, \qquad M^z(t,\mathbf{x}) = \int_V\int_Z zp(t,\mathbf{x},\mathbf{v},z)dzd\mathbf{v}$$
$$m^{zz}(t,\mathbf{x},\mathbf{v}) = \int_Z z^2p(t,\mathbf{x},\mathbf{v},z)dz.$$

Integration of (5.28) with respect to z yields

$$\partial_t m + \nabla\cdot(\mathbf{v}m) = \mathcal{L}[\lambda_0]m - \mathcal{L}[\lambda_1]m^z. \tag{5.30}$$

Multiply (5.28) with z and integrate again to obtain

$$\begin{aligned}\partial_t m^z + \nabla\cdot(\mathbf{v}m^z) + \int_Z z\partial_z\left[\left(-(k^+Q+k^-)z - f'\big(Q(\mathbf{x})\big)\mathbf{v}\cdot\nabla Q\right)p\right]dz \\ = \mathcal{L}[\lambda_0]m^z - \mathcal{L}[\lambda_1]m^{zz}.\end{aligned} \tag{5.31}$$

Assume, that we are close to the steady state and neglect second order moments in z. Then, (5.31) becomes

$$\partial_t m^z + \nabla\cdot(\mathbf{v}m^z) = -(k^+Q+k^-)m^z + f'\big(Q(\mathbf{x})\big)\big(\nabla Q\cdot\mathbf{v}\big)m + \mathcal{L}[\lambda_0]m^z. \tag{5.32}$$

Now, use a parabolic scaling $\hat{t} = \varepsilon^2 t$, $\hat{\mathbf{x}} = \varepsilon\mathbf{x}$, then drop the hats for notational simplification. This yields two equations:

$$\varepsilon^2\partial_t m + \varepsilon\nabla\cdot(\mathbf{v}m) = \mathcal{L}[\lambda_0]m - \mathcal{L}[\lambda_1]m^z, \tag{5.33}$$
$$\varepsilon^2\partial_t m^z + \varepsilon\nabla(\mathbf{v}m^z) = -(k^+Q+k^-)m^z + \varepsilon f'\big(Q(\mathbf{x})\big)\big(\nabla Q\cdot\mathbf{v}\big)m + \mathcal{L}[\lambda_0]m^z. \tag{5.34}$$

Use Hilbert expansions for m and m^z of the form

$$m = m_0 + \varepsilon m_1 + \varepsilon^2 m_2 + \dots \tag{5.35}$$
$$m^z = m_0^z + \varepsilon m_1^z + \varepsilon^2 m_2^z + \dots \tag{5.36}$$

After plugging these expressions into equations (5.33) and (5.34), one can collect terms of equal order in ε.

ε^0:

$$0 = \mathcal{L}[\lambda_0]m_0 - \mathcal{L}[\lambda_1]m_0^z, \tag{5.37}$$
$$0 = \mathcal{L}[\lambda_0]m_0^z - (k^+Q+k^-)m_0^z. \tag{5.38}$$

ε^1:

$$\nabla \cdot (\mathbf{v} m_0) = \mathcal{L}[\lambda_0] m_1 - \mathcal{L}[\lambda_1] m_1^z, \tag{5.39}$$
$$\nabla \cdot (\mathbf{v} m_0^z) = -(k^+ Q + k^-) m_1^z + f'\big(Q(\mathbf{x})\big)\big(\nabla Q \cdot \mathbf{v}\big) m_0 + \mathcal{L}[\lambda_0] m_1^z. \tag{5.40}$$

ε^2:

$$\partial_t m_0 + \nabla \cdot (\mathbf{v} m_1) = \mathcal{L}[\lambda_0] m_2 - \mathcal{L}[\lambda_1] m_2^z. \tag{5.41}$$

To solve this system of equations, we need some results for the behaviour of the turning operator $\mathcal{L}$, which are collected in the following lemma. For more details see (Hillen and Othmer, 2000).

Lemma 4 (Properties of the turning operator (Othmer and Hillen (2000))). *Make the following assumptions about the turning kernel K and the operators $\mathcal{T}$ from above:*

(T1) $K(\mathbf{v}, \mathbf{v}') \geq 0, \quad \int_V K(\mathbf{v}, \mathbf{v}') d\mathbf{v} = 1, \quad \int_V \int_V K^2(\mathbf{v}, \mathbf{v}') d\mathbf{v}' d\mathbf{v} < \infty$

(T2) There are functions u_0, ϕ and ψ such that $u_0 \neq 0$ which fulfill

$$u_0(\mathbf{v})\psi(\mathbf{v}') \leq K(\mathbf{v}, \mathbf{v}') \leq u_0(\mathbf{v})\psi(\mathbf{v}').$$

(T3) $\|\mathcal{T}\|_{\langle 1 \rangle^\perp} < 1$.

(T4) $\int_V K(\mathbf{v}, \mathbf{v}') d\mathbf{v}' = 1$.

Then, the operator $\mathcal{L}$ has the following properties:

1. *0 is a simple eigenvalue of $\mathcal{L}$ with eigenfunction $\phi_0 = 1$.*
2. *There are no positive eigenvalues.*
3. *$\mathcal{L}$ restricted to $\langle 1 \rangle^\perp$ has a linear inverse.*

Now, come back to the equation system above. Since the operator $\mathcal{L}$ has no positive eigenvalues, it follows from (5.38) that $m_0^z = 0$.
Then, we have from (5.37) ($0 = \mathcal{L}[\lambda_0] m_0$) that $m_0 = m_0(\mathbf{x}, t)$ is independent of $\mathbf{v}$.
Equation (5.40) then gives

$$0 = -(k^+ Q + k^-) m_1^z + f'\big(Q(\mathbf{x})\big)\big(\mathbf{v} \cdot \nabla Q\big) m_0 + \mathcal{L}[\lambda_0] m_1^z, \tag{5.42}$$

which means

$$\frac{f'\big(Q(\mathbf{x})\big)}{k^+ Q + k^-}\big(\mathbf{v} \cdot \nabla Q\big) m_0 = \left(\frac{-1}{k^+ Q + k^-}\mathcal{L}[\lambda_0] + \mathcal{I}\right) m_1^z. \tag{5.43}$$

From this, we now obtain that m_1^z has the form

$$m_1^z = \left(\frac{-1}{k^+ Q + k^-}\mathcal{L}[\lambda_0] + \mathcal{I}\right)^{-1} \left(\frac{f'\big(Q(\mathbf{x})\big)}{k^+ Q + k^-}\big(\mathbf{v} \cdot \nabla Q\big) m_0\right). \tag{5.44}$$

Equation (5.39) is the same as $\mathbf{v}\cdot\nabla m_0 = \mathcal{L}[\lambda_0]m_1 - \mathcal{L}[\lambda_1]m_1^z$, so we obtain as an explicit expression for m_1

$$m_1 = (\mathcal{L}[\lambda_0])^{-1}\left((\mathbf{v}\cdot\nabla m_0 + \mathcal{L}[\lambda_1]m_1^z)\right) \tag{5.45}$$

$$= (\mathcal{L}[\lambda_0])^{-1}\left(\left(\mathbf{v}\cdot\nabla m_0 + \mathcal{L}[\lambda_1]\left(\left(\frac{1}{k^+Q+k^-}\mathcal{L}[\lambda_0] - \mathcal{I}\right)^{-1}\left(\frac{f'\big(Q(\mathbf{x})\big)}{k^+Q+k^-}\big(\mathbf{v}\cdot\nabla Q\big)m_0\right)\right)\right)\right), \tag{5.46}$$

which only depends on the quantity m_0. Integration of (5.41) with respect to $\mathbf{v}$ gives

$$\int_V \partial_t m_0 + \mathbf{v}\cdot\nabla m_1 d\mathbf{v} = 0. \tag{5.47}$$

Since the inverse $(\mathcal{L}[\lambda_0])^{-1}$ is linear, we have

$$|V|\partial_t m_0 + \nabla\cdot\int_V \mathbf{v}(\mathcal{L}[\lambda_0])^{-1}\mathbf{v}d\mathbf{v}\nabla m_0 + \nabla\cdot\left(\frac{f'\big(Q(\mathbf{x})\big)}{k^+Q+k^-}\int_V \mathbf{v}\mathcal{L}[\lambda_0]^{-1}\left(\mathcal{L}[\lambda_1]\left(\frac{-1}{kQ+k^-}\mathcal{L}[\lambda_0]+\mathcal{I}\right)^{-1}\mathbf{v}\right)d\mathbf{v}\ \nabla Q m_0\right) = 0.$$

We can write this macroscopic evolution equation as

$$\partial_t m_0 = \nabla\cdot(\mathbb{D}(\mathbf{x})\nabla m_0 + \chi\nabla Q m_0), \tag{5.48}$$

with diffusion tensor

$$\mathbb{D}(\mathbf{x}) = \frac{1}{|V|}\int_V \mathbf{v}\otimes(\mathcal{L}[\lambda_0])^{-1}\mathbf{v}d\mathbf{v} \tag{5.49}$$

and drift velocity

$$\chi(\mathbf{x}) = \frac{1}{|V|}\frac{f'(Q(\mathbf{x}))}{k^+Q+k^-}\left(\int_V \mathbf{v}\otimes\left((\mathcal{L}[\lambda_0])^{-1}\mathcal{L}[\lambda_1]\left(\frac{-1}{k^+Q+k^-}\mathcal{L}[\lambda_0]+\mathcal{I}\right)\mathbf{v}\right)d\mathbf{v}\right). \tag{5.50}$$

Comparing with equation (5.14), we notice that the dynamics on the microscale leads to an additional haptotactic drift term for the movement.
The concrete choice of the turning kernel K influences singnificantly the behaviour of equation (5.48). Since K has to fullfill the assumptions of lemma 4, the choice is strongly limited because of the symmetry requirement. One possible choice is the trivial kernel $K(\mathbf{x},\mathbf{v},\mathbf{v}') = \frac{1}{|V|}$, where $|V|$ denotes the volume of the set of admissible velocities. This corresponds to a pure random motion of the cells, and leads hence to constant diffusion, what is less interesting from the biological viewpoint. The main issue in the choice of K is the assumption $(T)4$, which demands that K has to be a distribution with respect to the incoming velocity. However, this is not justified from the biological point of view.

6. Movement with resting phases: including proliferation

Strength and growth come only through continuous effort and struggle.

(Napoleon Hill)

Contents

6.1. Transport equations with resting phases

In the following sections a multiscale model for glioma spread will be proposed which includes proliferation and interactions of cells with the underlying tissue network. It has been shown, that the *go or grow* hypothesis (Hatzikirou et al., 2012) is a good starting point in modeling proliferative effects on the cell scale. The basic assumption there is, that cells can either move or stop and proliferate but not both at once. We use the approach in (Hillen, 2003) as our starting point and propose a similar model which is expanded by a model for the cell receptor dynamics on the microscale as in (Engwer et al., 2013). The go or grow assumption leads to a system of two coupled equations including a kinetic transport equation for the moving cells as well as an ordinary differential equation for the resting and hence proliferating cells.

We hence want to observe the density functions $p(t, \mathbf{x}, \mathbf{v}, \mathbf{y})$ of moving cells which are at time t at position $\mathbf{x} \in \mathbb{R}^n$ with velocity $\mathbf{v} \in V \subset \mathbb{R}^n$ and microscopic state $\mathbf{y} \in Y \subset \mathbb{R}^l$ and of resting (and hence proliferating) cells $r(t, \mathbf{x}, \mathbf{y})$. This leads to a system of equations of the form

$$\partial_t p + \nabla_{\mathbf{x}} \cdot (\mathbf{v}p) + \nabla_{\mathbf{y}} \cdot (\mathbf{G}(\mathbf{y})p) = \mathcal{L}[\lambda]p - \alpha(\mathbf{x})p + \frac{\beta q}{\omega} r - l(N)p, \tag{6.1}$$

$$\partial_t r = \alpha(\mathbf{x}) \int_V p d\mathbf{v} - \beta r + g(N)r - l(N)r. \tag{6.2}$$

Here $\mathcal{L}[\lambda]p := -\lambda(\mathbf{y})p + \lambda(\mathbf{y})\frac{q(\mathbf{x},\hat{\mathbf{v}})}{\omega}\int_V p(\mathbf{v}')d\mathbf{v}'$ is the *turning operator* modeling the cell velocity innovations due to contact guidance, environmental cues etc, and $\lambda(\mathbf{y})$ denotes the *turning rate* of cells. The vector $\mathbf{y}$ stands for the microscopic state of a cell. Its components can be, for instance, concentrations of proteins involved in some intracellular signaling network or -as will be the case throughout this work- concentrations of integrins bound to soluble and/or insoluble components of the cell environment. Its dynamics is characterized by a system of ordinary differential equations

$$\frac{d}{dt}\mathbf{y}(t) = \mathbf{G}(\mathbf{y}(t), Q), \tag{6.3}$$

where the right hand side is involving an insoluble environmental component as input. We will specify the function G in the next section.
The N in equations (6.1) and (6.2) denotes the total cell density and is here given by

$$N(t,\mathbf{x}) = \int_V \int_Y p(t,\mathbf{x},\mathbf{v},\mathbf{y})d\mathbf{y}\ d\mathbf{v} + \int_Y r(t,\mathbf{x},\mathbf{y})d\mathbf{y}, \tag{6.4}$$

and $g(N)$ and $l(N)$ are functions representing *gain* and *loss* due to cell death and proliferation. α and β are the rates in which cells stop and proliferate, respectively start moving again after a resting phase.

6.2. Cell surface receptor dynamics

As in chapter 5, we focus on the cell surface receptor dynamics of the cells. Transmembrane adhesion proteins bind to collagen fibres and other proteins in the extracellular matrix (ECM). In this work we focus on the class called *integrins* of those proteins and want to study the impact of this microscopic process on the macroscopic movement behaviour on the tissue scale. Let $Q(\mathbf{x})$ denote the volume fraction of ECM fibres which the integrins can bind to. Starting from simple mass action kinetics, the integrin dynamics on the cell surface is described by the following ordinary differential equation:

$$\dot{y} = k^+(R_0 - y)Q - k^- y, \tag{6.5}$$

where R_0 denotes the total number of receptors on the cell (we assume it is conserved), whereas $y(t)$ gives the density of integrins bound to ECM fibres. The constants k^+ and k^- denote the reaction rates for the reversible binding of integrins to the tissue fibres. The steady state of equation (6.5) is given by$y^* = \frac{k^+QR_0}{k^+Q+k^-}$.
We follow the ideas from section 5.1 and hence the ideas from (Erban and Othmer, 2005a) and introduce a new internal variable $z := y^* - y$ measuring deviations from the steady state. Looking again at a path of a single cell starting in $\mathbf{x}_0$ and moving with velocity $\mathbf{v}$ through a time-invariant density field $Q(\mathbf{x})$ we obtain with the notations $\mathbf{x} = \mathbf{x}_0 + \mathbf{v}t$ and

$$f(Q(\mathbf{x})) = \frac{k^+Q(\mathbf{x})R_0}{k^+Q(\mathbf{x}) + k^-} \tag{6.6}$$

that for any t

$$\frac{d}{dt} f\big(Q(\mathbf{x}_0 + \mathbf{v}t)\big) = f'(Q(\mathbf{x}_0 + \mathbf{v}t))\ \mathbf{v} \cdot \nabla Q(\mathbf{x}_0 + \mathbf{v}t).$$

For more details see also chapter 5. We choose again a turning rate of the form $\lambda(z) = \lambda_0 - \lambda_1 z \geq 0$, where λ_0 and λ_1 are some positive constants with $\lambda_0 \geq \lambda_1 R_0(1 - \frac{1}{K_r Q(\mathbf{x})+1})$ and $K_r := k^+/k^-$. In the next section we formulate our mesoscopic model for the cells.

6.3. The mesoscopic transport equation and its scaling

With the above analysis for the dynamics on the microscale, we obtain now a system of evolution equations for the density $p(t, \mathbf{x}, \mathbf{v}, z)$ of moving cells and the density $r(t, \mathbf{x}, z)$ of resting cells. The system reads

$$\begin{aligned} \partial_t p + \mathbf{v} \cdot \nabla p + \partial_z \left(\left(-(k^+ Q + k^-)z + f'(Q)\mathbf{v} \cdot \nabla Q \right) p \right) = \\ \mathcal{L}[\lambda_0]p + \mathcal{L}[\lambda_1]zp - \alpha(\mathbf{x})p + \frac{q\beta}{\omega} r - l(N)p \end{aligned} \tag{6.7}$$

$$\partial_t r = \alpha(\mathbf{x}) \int_V p d\mathbf{v} - \beta r + (g(N) - l(N))\, r. \tag{6.8}$$

Introduce the notation

$$m(t, \mathbf{x}, \mathbf{v},) = \int_Z p(t, \mathbf{x}, \mathbf{v}, z) dz, \quad w(t, \mathbf{x}) = \int_Z r(t, \mathbf{x}, z) dz \tag{6.9}$$

$$m^z(t, \mathbf{x}, \mathbf{v}) = \int_Z z p(t, \mathbf{x}, \mathbf{v}, z) dz, \quad w^z(t, \mathbf{x}) = \int_Z z r(t, \mathbf{x}, z) dz \tag{6.10}$$

$$M(t, \mathbf{x}) = \int_V m d\mathbf{v}, \quad M^z(t, \mathbf{x}) = \int_V m^z d\mathbf{v}. \tag{6.11}$$

Integration of the equations (6.7) and (6.8) with respect to z gives

$$\partial_t m + \mathbf{v} \cdot \nabla m = \mathcal{L}[\lambda_0]m + \mathcal{L}[\lambda_1]m^z - \alpha m + \frac{\beta q}{\omega} w - l(N)m, \tag{6.12}$$

$$\partial_t w = \alpha(\mathbf{x})M - \beta w + (g(N) - l(N))\, w. \tag{6.13}$$

Multiply equations (6.7) and (6.8) by z and integrate again with resp. to z. As in (Engwer et al., 2013) we neglect moments of higher order in z and obtain

$$\begin{aligned} \partial_t m^z + \mathbf{v} \cdot \nabla m^z = -(k^+ Q + k^-)m^z + f'(Q)\mathbf{v} \cdot \nabla Q m + \mathcal{L}[\lambda_0]m^z \\ - \alpha m^z + \frac{\beta q}{\omega} w^z - l(N)m^z, \end{aligned} \tag{6.14}$$

$$\partial_t w^z = \alpha M^z - \beta w^z + g(N)w^z - l(N)w^z. \tag{6.15}$$

Now, we use a parabolic scaling $\hat{t} \to \varepsilon^2 t$, $\hat{\mathbf{x}} \to \varepsilon \mathbf{x}$, then drop the hats for notational simplification. In addition, scale the birth-death dynamics as in (Hillen, 2003) by

$$g(N) \to \varepsilon^2 \hat{g}(\hat{N}) \tag{6.16}$$
$$l(N) \to \varepsilon^2 \hat{l}(\hat{N}), \tag{6.17}$$

then drop hats again. From equations (6.12), (6.13), (6.14) and (6.15) we obtain the equations

$$\varepsilon^2 \partial_t m + \varepsilon \mathbf{v} \cdot \nabla m = \mathcal{L}[\lambda_0] m + \mathcal{L}[\lambda_1] m^z - \alpha m + \frac{\beta q}{\omega} w - \varepsilon^2 l(N) m, \tag{6.18}$$
$$\varepsilon^2 \partial_t w = \alpha(\mathbf{x}) M - \beta w + \varepsilon^2 \left(g(N) - l(N)\right) w, \tag{6.19}$$
$$\begin{aligned} \varepsilon^2 \partial_t m^z + \varepsilon \mathbf{v} \cdot \nabla m^z &= -(k^+ Q + k^-) m^z + \varepsilon f'(Q) \mathbf{v} \cdot \nabla Q m \\ &\quad + \mathcal{L}[\lambda_0] m^z - \alpha m^z + \frac{\beta q}{\omega} w^z - \varepsilon^2 l(N) m^z, \end{aligned} \tag{6.20}$$
$$\varepsilon^2 \partial_t w^z = \alpha M^z - \beta w^z + \varepsilon^2 \left(g(N) - l(N)\right) w^z. \tag{6.21}$$

Now, we use Hilbert expansions for m, m^z, w, w^z, M, M^z of the form

$$\begin{aligned} m &= m_0 + \varepsilon m_1 + \varepsilon^2 m_2 + \ldots, \quad & M &= M_0 + \varepsilon M_1 + \varepsilon^2 M_2 + \ldots \\ m^z &= m_0^z + \varepsilon m_1^z + \varepsilon^2 m_2^z + \ldots, \quad & M^z &= M_0^z + \varepsilon M_1^z + \varepsilon^2 M_2^z + \ldots \\ w &= w_0 + \varepsilon w_1 + \varepsilon^2 w_2 + \ldots, \quad & w^z &= w_0^z + \varepsilon w_1^z + \varepsilon^2 w_2^z + \ldots \\ N &= N_0 + \varepsilon N_1 + \varepsilon^2 N_2 + \ldots \end{aligned}$$

and compare terms of equal order in ε.

ε^0:

$$0 = \mathcal{L}[\lambda_0] m_0 + \mathcal{L}[\lambda_1] m_0^z - \alpha m_0 + \frac{\beta q}{\omega} w_0, \tag{6.22}$$
$$0 = \alpha M_0 - \beta w_0, \tag{6.23}$$
$$0 = -(k^+ Q + k^-) m_0^z - \alpha m_0^z + \frac{\beta q}{\omega} w_0^z + \mathcal{L}[\lambda_0] m_0^z, \tag{6.24}$$
$$0 = \alpha M_0^z - \beta w_0^z. \tag{6.25}$$

ε^1 :

$$\mathbf{v} \cdot \nabla m_0 = \mathcal{L}[\lambda_0] m_1 + \mathcal{L}[\lambda_1] m_1^z - \alpha m_1 + \frac{\beta q}{\omega} w_1, \tag{6.26}$$
$$0 = \alpha M_1 - \beta w_1, \tag{6.27}$$
$$\mathbf{v} \cdot \nabla m_0^z = -(k^+ Q + k^-) m_1^z + f'(Q) \mathbf{v} \cdot \nabla Q m_0 + \mathcal{L}[\lambda_0] m_1^z - \alpha m_1^z + \frac{\beta q}{\omega} w_1^z, \tag{6.28}$$
$$0 = \alpha M_1^z - \beta w_1^z. \tag{6.29}$$

ε^2 :

$$\partial_t m_0 + \mathbf{v} \cdot \nabla m_1 = \mathcal{L}[\lambda_0] m_2 + \mathcal{L}[\lambda_1] m_2^z - \alpha m_2 + \frac{\beta q}{\omega} w_2 - l(N_0) m_0, \tag{6.30}$$

$$\partial_t w_0 = \alpha M_2 - \beta w_2 + (g(N_0) - l(N_0))\, w_0. \tag{6.31}$$

It is our goal now to derive an evolution equation for the macroscopic cell density

$$N_0(t, \mathbf{x}) = w_0 + M_0 = \left(1 + \frac{\alpha}{\beta}\right) M_0. \tag{6.32}$$

We start with the ε^0-equations. First of all, we obtain from (6.25) that $w_0^z = \frac{\alpha}{\beta} M_0^z$. Integration of (6.24) with respect to $\mathbf{v}$ yields

$$0 = -(k^+ Q + k^-) M_0^z - \alpha M_0^z + \beta w_0^z, \tag{6.33}$$

which implies $M_0^z = 0$, $m_0^z = 0$ and $w_0^z = 0$. Equation (6.23) gives

$$w_0 = \frac{\alpha}{\beta} M_0. \tag{6.34}$$

Finally, we obtain from (6.22)

$$0 = \mathcal{L}[\lambda_0] m_0 - \alpha m_0 + \frac{q\alpha}{\omega} M_0, \text{ what implies } m_0 = \frac{q}{\omega} M_0. \tag{6.35}$$

Analyzing the ε^1 equations yields the following. Starting with eq. (6.29) we obtain

$$w_1^z = \frac{\alpha}{\beta} M_1^z. \tag{6.36}$$

From equation (6.28) we obtain after integration w.r.t. $\mathbf{v}$ that $M_1^z = 0$ and hence also $w_1^z = 0$. Here, we used the assumption $\int_V \mathbf{v} q \; d\mathbf{v} = 0$ for undirected tissue. Then, again from (6.28) we obtain the following expression for m_1^z

$$m_1^z = \frac{1}{k^+ Q + k^- + \lambda_0 + \alpha} f'(Q) \mathbf{v} \cdot \nabla Q m_0. \tag{6.37}$$

Equation (6.26) leads to the expression

$$m_1 = -\frac{1}{\lambda_0 + \alpha} \left(\mathbf{v} \cdot \nabla m_0 + \lambda_1 m_1^z\right), \tag{6.38}$$

where we used that the inverse $\mathcal{L}[\lambda_0 + \alpha]^{-1}_{|<q>^\perp}$ of the operator $\mathcal{L}[\lambda_0 + \alpha]$ is just the multiplication by the factor $-\frac{1}{\lambda_0 + \alpha}$.
Using equations (6.30) and (6.31) we can derive an evolution equation for the macroscopic cell density (6.32). From (6.31) we have

$$\frac{\beta}{\omega} w_2 = \frac{1}{\omega} \left(\alpha M_2 + (g(N_0) - l(N_0))\, w_0 - \partial_t w_0\right), \tag{6.39}$$

and plugging this term into equation (6.30) we obtain

$$\partial_t m_0 + \mathbf{v}\cdot\nabla m_1 = \mathcal{L}[\lambda_0]m_2 + \mathcal{L}[\lambda_1]m_2^z - \alpha m_2 + \frac{\alpha q}{\omega}M_2 + \frac{q}{\omega}\left(g(N_0) - l(N_0)\right)\frac{\alpha}{\beta}M_0 - \frac{q}{\omega}\partial_t\left(\frac{\alpha}{\beta}M_0\right) - l(N_0)m_0. \tag{6.40}$$

After integrating again with respect to $\mathbf{v}$ this yields

$$\partial_t M_0 + \int_V \mathbf{v}\cdot\nabla m_1 \, d\mathbf{v} = \left(g(N_0) - l(N_0)\right)\frac{\alpha}{\beta}M_0 - \frac{\alpha}{\beta}\partial_t M_0 - l(N_0)M_0. \tag{6.41}$$

Rearranging gives

$$\partial_t\left(1+\frac{\alpha}{\beta}\right)M_0 + \nabla\cdot\int_V \mathbf{v}m_1 \, d\mathbf{v} = \frac{\alpha}{\beta}g(N_0)M_0 - \left(1+\frac{\alpha}{\beta}\right)M_0 l(N_0). \tag{6.42}$$

With the defined macroscopic quantity

$$N_0 = \left(1+\frac{\alpha}{\beta}\right)M_0 \tag{6.43}$$

we obtain

$$\partial_t N_0 + \nabla\cdot\int_V \mathbf{v}m_1 \, d\mathbf{v} = \frac{\alpha}{\alpha+\beta}g(N_0)N_0 - N_0 l(N_0). \tag{6.44}$$

Now, we evaluate $\int_V \mathbf{v}m_1 d\mathbf{v}$. Recall

$$m_1 = -\frac{1}{\lambda_0+\alpha}\left(\mathbf{v}\cdot\nabla\left(\frac{q}{\omega}M_0\right) + \lambda_1 m_1^z\right). \tag{6.45}$$

Writing $g(\mathbf{x}) = \frac{1}{k^+Q+k^-+\lambda_0+\alpha}$ and hence $m_1^z = g(\mathbf{x})f'(Q)\mathbf{v}\cdot\nabla Q m_0$ we have

$$m_1 = -\frac{1}{\lambda_0+\alpha}\left(\mathbf{v}\cdot\nabla\left(\frac{q}{\omega}M_0\right) + \lambda_1 g(\mathbf{x})f'(Q)\mathbf{v}\cdot\nabla Q\frac{q}{\omega}M_0\right). \tag{6.46}$$

It follows

$$\begin{aligned}\nabla\cdot\int \mathbf{v}m_1 \, d\mathbf{v} &= \nabla\cdot\left(-\frac{1}{\lambda_0+\alpha}\int_V \mathbf{v}\mathbf{v}^t\nabla\left(\frac{q}{\omega}M_0\right)d\mathbf{v}\right) \\ &\quad + \nabla\cdot\left(\frac{\lambda_1}{\lambda_0+\alpha}\int_V \mathbf{v}\mathbf{v}^t\frac{q}{\omega}\, d\mathbf{v}g(\mathbf{x})f'(Q)\nabla Q M_0\right) \qquad (6.47)\\ &= \nabla\cdot\left(-\frac{1}{\lambda_0+\alpha}\nabla\left(\frac{1}{\omega}\int_V \mathbf{v}\mathbf{v}^t q \, d\mathbf{v}M_0\right)\right) \\ &\quad + \nabla\cdot\left(\frac{\lambda_1}{\lambda_0+\alpha}g(\mathbf{x})f'(Q)\frac{1}{\omega}\int_V \mathbf{v}\mathbf{v}^t q \, d\mathbf{v}\cdot\nabla Q M_0\right). \qquad (6.48)\end{aligned}$$

Finally, we obtain with

$$M_0 = \frac{\beta}{\alpha+\beta}N_0 \text{ and } \mathbb{D}_T(\mathbf{x}) = \frac{1}{\omega}\int_V \mathbf{v}\mathbf{v}^t q \, d\mathbf{v}$$

the evolution equation

$$\begin{aligned}\partial_t N_0 &= \nabla \cdot \left(\frac{1}{\lambda_0 + \alpha} \nabla \cdot \left(\frac{\beta}{\alpha + \beta} \mathbb{D}_T(\mathbf{x}) N_0 \right) \right) - \nabla \cdot \left(\frac{\lambda_1}{\lambda_0 + \alpha} \frac{\beta}{\alpha + \beta} g(\mathbf{x}) f'(Q) \mathbb{D}_T(\mathbf{x}) \cdot \nabla Q N_0 \right) \\ &= \frac{\alpha}{\alpha + \beta} g(N_0) N_0 - N_0 l(N_0). \end{aligned} \tag{6.49}$$

Note, that the diffusion tensor compared to the tensor (5.20) is scaled by the factor $\frac{\beta}{\alpha+\beta}$, which gives the ratio of moving cells. This makes sense from the viewpoint of biology, since proliferating cells should not move at all and hence not diffuse. Analogously, the factor $\frac{\alpha}{\alpha+\beta}$ corresponds to a ratio of resting cells, since only these are able to proliferate. Recall, that we still have to determine the form of q in order to obtain explicit expressions for the tumor diffusion tensor $\mathbb{D}_T(\mathbf{x})$.

6.4. Determination of the coefficients

The determination of explicit forms for the coefficients works analogously to section 5.4. For the relation of the distribution function q and DTI data we choose again the normalized *peanut*

$$q(\mathbf{x}, \theta) = \frac{n}{|\mathbb{S}^{n-1}| \operatorname{tr} \mathbb{D}_W(\mathbf{x})} \theta^t \mathbb{D}_W(\mathbf{x}) \theta. \tag{6.50}$$

This leads to the tumor diffusion tensor

$$\mathbb{D}_T(\mathbf{x}) = \frac{s^2}{(n+2)} \left(\mathbb{I}_n + 2 \frac{\mathbb{D}_W(\mathbf{x})}{\operatorname{tr} \mathbb{D}_W(\mathbf{x})} \right). \tag{6.51}$$

The values for the rates α and β have to be estimated from biological considerations and expereiments, see also chapter 8 for a more detailed discussion.

Part IV.

Numerical simulation

7. Discretization

The purpose of computing is insight, not numbers.

(Richard Hamming)

Contents

7.1. General remarks

In chapter 9 some numerical simulation results for the tumor growth models derivedin chapters 5 and 6 will be presented. The simulations have been performed in cooperation with Christian Engwer[1], and without his expertize in numerical treatment of complex systems these simulations would not have been possible.
All simulations have been performed DTI data based on 2D brain slices, where the pre-processed data has been provided by courtesy of Carsten Wolters [2].
Recall that we obtained an advection-diffusion equation respectively an advection-diffusion-reaction equation as macroscopic limits with coefficients depending pointwise on the data. The tumor diffusion tensor and the tumor drift velocity are precalculated in the MATLAB[3] numerics software. The simulations of the macroscopic evolution equation are implemented using the DUNE framework (Bastian et al., 2008).
In this chapter we will start with the description of our discretization method, and subsequently in chapter 8 I will collect the arguments for the extraction of the model parameters from the data. The following section is based on the publication (Engwer et al., 2013).

7.2. Numerical method

Both the diffusion coefficient as well as the drift coefficient in the model equations are sptially dependent, and we expect regions in space where the system is diffusion dominated and regions where it is drift dominated. This can be expressed by the spatially dependent Péclet number $\mathrm{PE} = \frac{\|\mathbf{v}(\mathbf{x})\mathbf{L}\|}{\|\mathbb{D}_T(\mathbf{x})\|}$, where the norm in the denomerator is the L^2

[1] Prof.Dr. Christian Engwer, Institut für Numerische und Angewandthe Mathematik
[2] PD Dr. Carsten Wolters, Institut für Biomagentismus und Biosignalanalys, Universität Münster
[3] MATLAB Release 2012b, The MathWorks, Inc., Natick, Massachusetts, United States.

norm, while we take in the denominator the Frobenius norm of $\mathbb{D}$. L is a macroscopic characteristic length scale (2 mm, in our present setting and simulations). For PE $\ll$ 1 we have a diffusion dominated case, and classical methods for parabolic equations will apply, while for PE $\gg$ 1 the equation behaves like a hyperbolic equation, and hyperbolic methods need to be used. In Figure 8.2(d) we illustrate the behavior of the Frobenius norm of $\mathbb{D}_T(\mathbf{x})$ and of the Péclet number in 4(b) and 4(d), respectively. A large Peclet number along the white matter tracks is clearly observed. The numerical scheme needs to be able to handle degenerated anisotropic parabolic equations and full tensors. Furthermore it should be locally mass conservative. For these reasons we decided to employ a first order discontinuous Galerkin (dG) scheme in space and an implicit Euler scheme in time. This method is overall first order accurate. For the simulation we use a structured mesh $\mathcal{M}(\Omega) = \{E_i\}$, which is a subset of the voxel mesh of the DTI data. Since our mesh is Cartesian with mesh-width h, the sets E_i are simply the grid cells that belong to the brain tissue. We define the skeleton of M as the boundary between those grid cells,

$$\Gamma = \{\gamma_{e,f} = \partial E_e \cap \partial E_f \mid E_e, E_f \in \mathcal{M},\ E_e \neq E_f, \text{ and } |\gamma_{e,f}| > 0\}.$$

We first discuss the spatial discretization. We use a symmetric interior penalty discontinuous Galerkin method (SIPG) (Wheeler, 1978) as implemented in DUNE (Bastian et al., 2008). We denote with V_h the discontinuous Galerkin Ansatz-space, which is in our case the space of piecewise bilinear polynomials

$$V_h = \left\{ \nu_h \in L^2(\Omega) \,:\, \nu_h|_E \in Q_1(E), E \in \mathcal{M}(\Omega) \right\},$$

where $Q_1(E)$ denotes the set of affine linear functions on E. We test the above equation with these ansatz functions, use a weak formulation, and express coupling conditions along the skeleton through jumps $[\![\cdot]\!]$ and averages $\{\cdot\}$ in a similar notation as in (Arnold et al., 2002). We use weighted averages, as proposed in (Ern et al., 2009). Omitting the computational details, which can be found for example in (Arnold et al., 2002), the resulting semi-discrete problem reads:
Find $M_{0h}(t) \in V_h$ such that

$$\partial_t M_{0h}(t) + a_h\big(M_{0h}(t), \nu_h\big) + J_h\big(M_{0h}(t), \nu_h\big) = 0 \qquad \forall \nu_h \in V_h, \tag{7.1}$$

with the bilinear form a_h and a penalty term J_h given by

$$\begin{aligned} a_h\big(M_{0h}(t), \nu_h\big) = &\int_\Omega \mathbb{D}_T \nabla M_{0h}(t) \cdot \nabla \nu_h \, dx - \int_\Gamma [\![M_{0h}(t)]\!] \cdot \{ \mathbb{D}_T \nabla \nu_h \} \\ &+ [\![\nu_h]\!] \cdot \{ \mathbb{D}_T \nabla M_{0h}(t) \} \, ds - \int_\Omega \mathbf{v} \, M_{0h}(t) \, \nabla \nu_h \, dx \\ &+ \int_\Gamma [\![\nu_h]\!] \cdot \mathbf{v} \, M_{0h}^{\uparrow}(t) ds. \end{aligned} \tag{7.2}$$

and

$$J_h\big(M_{0h}(t), \nu_h\big) = \eta h^{-1} \int_\Gamma [\![M_{0h}]\!] [\![\nu_h]\!] \, ds \,, \tag{7.3}$$

where $\eta > 0$ denotes the penalty factor. For a good choice of η we refer to (Ern et al., 2009).

Note that we require the normal velocity to be continuous, i.e. $\mathbf{v}|_{\partial E_n}\mathbf{n}_n = -\mathbf{v}|_{\partial E_m}\mathbf{n}_m$, where $\mathbf{n}_n$ denotes the outer normal vector of grid cell E_n. To ensure this, we use a Raviart-Thomas RT0 approximation of the velocity field. On an internal edge with two adjacent cells E_n and E_m we define

$$[\![x]\!] = x|_{\partial E_n}\mathbf{n}_n + x|_{\partial E_m}\mathbf{n}_m \;\text{ and }\; \{ x \} = \omega_n x|_{\partial E_n} + \omega_m x|_{\partial E_m},$$

with weights ω_n, ω_m and the unit outer normal vectors $\mathbf{n}_n, \mathbf{n}_m$. To be robust with respect to heterogeneous diffusion coefficients, we use the weights

$$\omega_n = \frac{\mathbf{n}_n^t \mathbb{D}_{Tn}\mathbf{n}_n}{\mathbf{n}_n^t(\mathbb{D}_{Tn} + \mathbb{D}_{Tm})\mathbf{n}_n} \text{ and } \omega_m = \frac{\mathbf{n}_m^t \mathbb{D}_{Tm}\mathbf{n}_m}{\mathbf{n}_m^t(\mathbb{D}_{Tn} + \mathbb{D}_{Tm})\mathbf{n}_m}$$

respectively, where $\mathbb{D}_{Tn}$ denotes the tumour diffusion tensor computed in E_n. Note that due to $\mathbf{n}_n = -\mathbf{n}_m$ the relation $\omega_n + \omega_m = 1$ holds.

The advective term is stabilized using an upwind formulation with the upwind reconstruction $M_{0h}^{\uparrow}$ of the cell density. For the time discretization of M_{0h} we used an implicit Euler scheme and time steps τ such that we fulfill a CFL condition of 1.

8. Extraction of the model parameters

> If you have a procedure with 10 parameters, you probably missed some.
>
> *(Alan Perlis)*

Contents

8.1. Parameter extraction from DTI data

The coefficients in the macroscopic model equations (5.14) and (6.49) as well as the computational domain Ω are obtained from 3d DTI data. In this section I will describe how to obtain these values from given data and will also give some background information about sources of biological model parameters. To get a first impression of the data consider the T1 image in figure 8.1(a) which shows on a horizontal slice grey and white matter regions of a human brain. Figure 8.1(b) shows the according image segmentation and also yields the actual computational domain Ω as the union of these tissues, depicted in yellow and light red color. Figure 8.1(c) shows a fractional anisotropy map computed from the eigenvalues of the water diffusion tensor for each voxel and finally figure 8.1(d) visualizes the largest eigenvector, i.e., the main direction of diffusion.

Coefficients of the macroscopic equations have been calculated for each voxel of the brain with the known values of the water diffusion tensor $\mathbb{D}_W$. As shown in section 5.4, the form of the coefficients depends on the chosen relationship between values of the measured apparent water diffusion tensor and the fibre distribution function q. Two possible choices have been considered, the *peanut distribution* and a *von Mises-Fisher distribution*, both leading to different tumor diffusion tensors.

For the peanut distribution

$$q(\mathbf{x}, \theta) = \frac{n}{|\mathbb{S}^{n-1}| \operatorname{tr} \mathbb{D}_W(\mathbf{x})} \theta^t \mathbb{D}_W(\mathbf{x}) \theta. \tag{8.1}$$

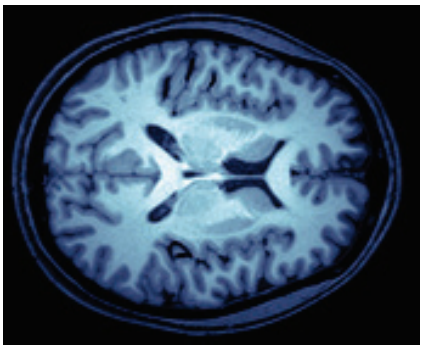

(a) T1 weighted picture of a brain slice.

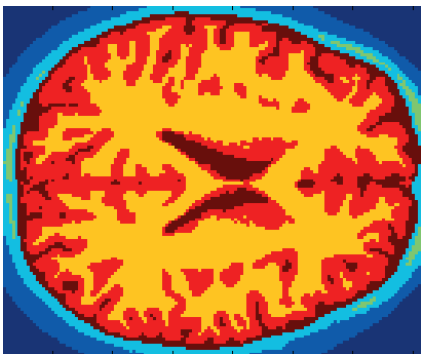

(b) Segmentation of the brain slice.

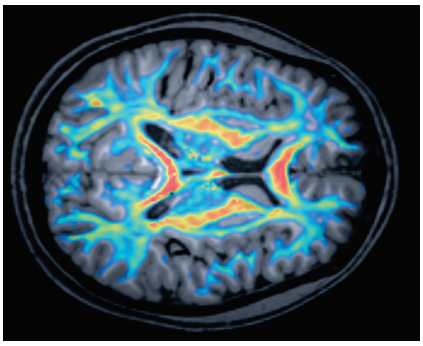

(c) Overlay of fractional anisotropy and T1 picture.

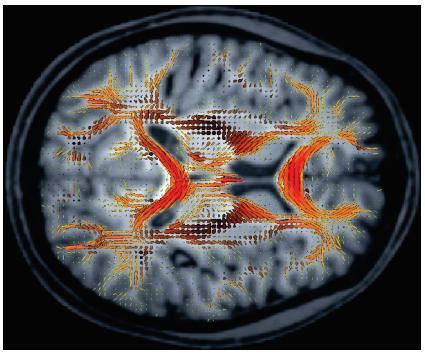

(d) Visualization of the main direction of diffusion by a vector pointing in the direction of the tensor's leading eigenvalue.

Figure 8.1.: Scanned and processed MRI brain data of a healthy young male subject.

it has been shown that the tumor diffusion tensor is explicitly given by

$$\mathbb{D}_T(\mathbf{x}) = \frac{s^2}{\lambda_0(n+2)} \left(\mathbb{I}_n + 2\frac{\mathbb{D}_W(\mathbf{x})}{\operatorname{tr} \mathbb{D}_W(\mathbf{x})} \right), \tag{8.2}$$

and depends on the values of the apparent water diffusion tensor. The tumor diffusion tensor has been calculated in Matlab, where derivatives involved in the corresponding drift correction term $\mathbf{u}(\mathbf{x}) = \nabla \cdot \mathbb{D}_T(\mathbf{x})$ have been evaluated with a finite difference scheme. For the simulations these quantities were then projected onto the 2D simulation slice.

Because the peanut distribution did not sufficiently reflect the anisotropy of the process in the mesoscale framework (Painter and Hillen, 2013), a von Mises-Fisher distribution of the form

$$q(\mathbf{x}, \theta) = \frac{\delta}{8\pi} + (1-\delta)\frac{k(\mathbf{x})}{4\pi \sinh(k(\mathbf{x}))} \left(e^{k\phi\cdot\theta} + e^{-k\phi\cdot\theta} \right) \tag{8.3}$$

has been alternatively been proposed in (Painter and Hillen, 2013). Recall that $k(\mathbf{x}) = \kappa \cdot \mathrm{FA}(\mathbf{x})$ and that $\mathrm{FA}(\mathbf{x})$ denotes the fractional anisotropy index for each voxel. ϕ

represents the leading eigenvector of the diffusion tensor for each voxel and κ can be interpreted as the sensitivity of the cells to the orientation of the underlying fibre structure. δ reflects the influence of stochastic effects. For a δ close to 0 stochasticity will also tend to zero. This leads to the alternative tumor diffusion tensor

$$\mathbb{D}_T(\mathbf{x}) = \frac{s^2}{3\lambda_0}\left[\left(\delta + (1-\delta)\left(\frac{\coth k}{k} - \frac{1}{k^2}\right)\right)\mathbb{I} + (1-\delta)\left(1 - \frac{3\coth k}{k} + \frac{3}{k^2}\right)\phi\phi^t\right]. \tag{8.4}$$

Given the eigenvalues of $\mathbb{D}_W$, the fractional anisotropy index has been computed for each voxel in `Matlab`. Additionally, the leading eigenvector was known, hence one obtains $\mathbb{D}_T$ by direct computations.

Both choices have their inherent advantages and disadvantages and the actual relation between $\mathbb{D}_W$ and q is still unclear. I will come back to this point in the discussion. Sadly, DTI is not capable to directly provide information about the local tissue structure on the scale of proteins within the ECM. The size of a voxel lies within a range of a millimeter whereas proteins to which cell surface receptors can bind have just a size of several microns. We hence assumed, that the quantity Q is the volume fraction of aligned tissue fibres and correlated it to the fractional anisotropy index to estimate the volume fraction Q of aligned ECM tissue. Hence, we computed $Q(\mathbf{x}) = \mathrm{FA}(\mathbf{x})$ for each point in the simulation domain. The computational domain Ω has been chosen as the union of white and grey matter regions.

8.2. Parameters obtained from biological experiments

Several other parameters can directly be related to biologically observable quantities. As far as this was possible, experimental sources for those parameters have been cited in table 8.1. The following list summarizes our model parameters and their biological meaning.

- The **number of receptors per cell**, R_0, is crucial for the binding dynamics. It denotes the average number of transmembrane adhesion molecules per cell which bind to surrounding proteins as well as to other cells. Although this number varies from cell type to cell type, it can be estimated from biological experiments that an average value of several ten thousand up to hundred thousand receptors per cell is realistic.

- The **cell turning rate** λ_0 is a measure for how often cells choose new directions of movement and is defined as the inverse of the **mean run time**. Especially for kinetic models this quantity is crucial for the modelling. However, estimations for average turnig rates can be obtained from biological experiments and have unit $[1/s]$.

- The **cell speed** s gives the absolute speed of a moving cell measured in $[m/s]$. Of course, these values differ between cell types, but since we observed that the choice

of s results only in time scaling of the simulation this parameter is not crucial. We chose an average value which reflects the rough biophysical dimension.

- The **receptor binding rates** k^+ and k^- measure the binding and dissociation of cell surface receptors to surrounding proteins. Note, that since the rate k^+ is not a classical second order reaction rate but a measure for how many receptors per cell bind to ligands per unit time, it has the same unit as k^- (which is $\frac{1}{s}$). Since no appropriate data were available, we assumed that $k^+ \approx k^-$ because the surface dynamics should always be close to its steady state.

- The **cell stopping rate** α denotes the rate in which cells stop their movement to pass into a resting phase. Accordingly, the **cell moving rate** is a measure for how cells start moving again after resting. Both rates have unit $\frac{1}{s}$.

- The **proliferation rate** r_g is a measure for how often cells devide and grow. In this work it has been related to the duration of a cell cycle. Accordingly, the **apoptosis rate** r_l is related to the mean life span of a cell and a measure for the frequency of cell death.

We tested variations of these parameters by $\pm 50\%$ and found very similar simulation behavior for the parameters.

Parameter	Interpretation	Dimension	Source
R_0	Receptors	$10^4 - 10^5$	(Belkin et al., 2005)
s	Cell speed	$10^{-6}\frac{\mathrm{m}}{\mathrm{s}}$	(Sidani et al., 2007)
λ_0	Turning rate	$10^{-1}\frac{1}{s}$	(Sidani et al., 2007)
λ_1	Deviation turning rate	$10^{-2}\frac{1}{s}$	estimated
k^+	Binding constant	$10^{-1}\frac{1}{s}$	estimated
k^-	Dissociation parameter	$10^{-1}\frac{1}{s}$	(Lauffenburger and Lindermann, 1993)
α	Stopping rate	$10^{-2}\frac{1}{s}$	estimated
β	Moving rate	$10^{-2}\frac{1}{s}$	estimated
r_g	Proliferation rate	$10^{-5}\frac{1}{s}$	source
r_l	Cell death rate	$10^{-7}\frac{1}{s}$	source

Table 8.1.: Choice of parameters which cannot be obtained from MRI data.

8.3. Visualization of the coefficients

Since the coefficients depend on DTI data, the understanding of their spatial variation is interesting. Figure 8.2 shows a visualization of the coefficients for a part of the simulation domain (see figure 8.2(a)). In figure 8.2(b) the Frobenius norm of the tumor diffusion tensor has been plotted for each voxel. Obviously, its behavior varies significantly between grey and white matter regions. This makes sense from the viewpoint of

biology, since diffusion along highly aligned tissue structure (as in white matter) is faster than in an isotropic structure, where barrieres in all directions occur (as in grey matter). The diffusive transport of cells is hence faster in white matter regions. Figure 8.2(c)

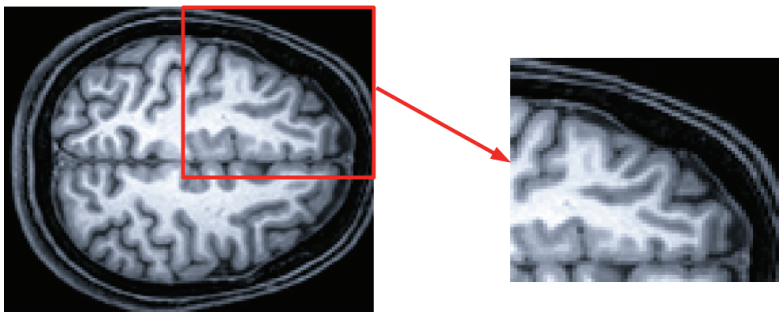

(a) For the visualization we focus on the selected right upper part of the brain slice.

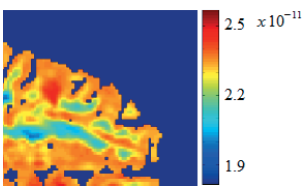

(b) Local Frobenius norm of the tumor diffusion tensor.

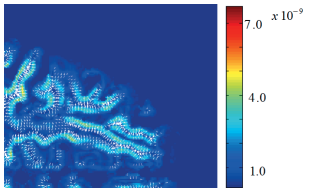

(c) Quiver plot of the drift term resulting from internal dynamics.

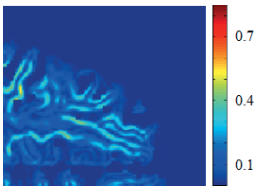

(d) Local Péclet number

Figure 8.2.: Visualization of the local invasive behavior.

shows a quiver plot for the drift term as well as the magnitude of the velocity. Again, a significant difference between regions of grey and white matter is visible. Enlarged velocities occur within the highly aligned regions, since it is easier for cells to move along fibre tracts than through an isotropic network, hence white matter regions with a high anisotropy lead to higher velocities.
Figure 8.2(d) shows the Péclet number $\mathrm{PE} = \frac{\|\mathbf{v}(\mathbf{x})\|\mathbf{L}}{\|\mathbb{D}_T(\mathbf{x})\|}$, where the norm in the denumerator is the L^2 norm and the norm in the denominator the Frobenius norm of $\mathbb{D}$. L is a macroscopic characteristic length scale (2 mm, in our present setting and simulations). The Péclet number indicates where the migration is dominated by diffusion and where by advection. It can be seen, that white matter regions are drift dominated, which corresponds to an active movement of cells along the tissue structure, while grey matter regions are diffusion dominated since cells have no preferred directon of movement in this case.

9. Simulation results

> The purpose of computing is insight, not numbers.
>
> *(Richard Hamming)*

Contents

9.1. Simulation Results for the advection-diffusion model

In this section some numerical simulations for the macroscopic evolution equation from chapter 5 will be presented. Recall that we obtained the equation

$$\partial_t M_0 - \nabla \cdot (\mathbb{D}_T(\mathbf{x}) \nabla M_0) + \nabla \cdot ([g(Q(\mathbf{x}))\mathbb{D}_T(\mathbf{x}) \nabla Q(\mathbf{x}) - \mathbf{u}(\mathbf{x})]\ M_0) = 0. \tag{9.1}$$

As shown in section 5.4, the coefficients depend of the explicit form of the distribution function q. Simulation results will be shown for both the peanut distribution function in section 9.1.1 and for the von Mises-Fisher form in section 9.1.2. Section 9.1.3 is then concerned with a numerical comparison of both cases. Table 9.1 shows how the model parameters have been chosen for the simulation.

Parameter	Interpretation	Value	Source
R_0	Number of receptors	10^5	(Belkin et al., 2005)
s	Cell speed	$10^{-6}\frac{\mathrm{m}}{\mathrm{s}}$	(Sidani et al., 2007)
λ_0	Turning rate	$0.1\frac{1}{\mathrm{s}}$	(Sidani et al., 2007)
λ_1	Deviation turning rate	$0.01\frac{1}{\mathrm{s}}$	estimated
k^+	Binding rate	$0.1\frac{1}{\mathrm{s}}$	estimated
k^-	Unbinding rate	$0.1\frac{1}{\mathrm{s}}$	(Lauffenburger and Lindermann, 1993)

Table 9.1.: Choice of parameters for the simulations.

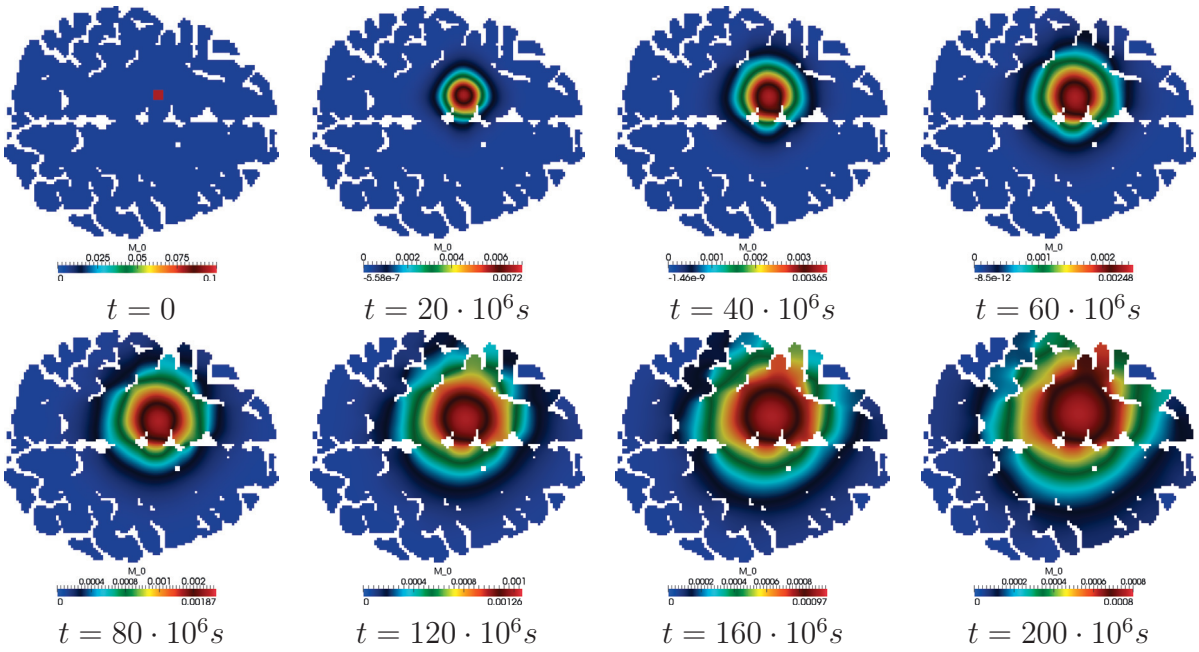

Figure 9.1.: Spread of cancer cells in the brain: case not involving subcellular dynamics.

9.1.1. Peanut distribution

The coefficients have been explicitly computed for the peanut distribution yield the expression

$$\mathbb{D}_T(\mathbf{x}) = \frac{s^2}{\lambda_0(n+2)} \left(\mathbb{I}_n + 2\frac{\mathbb{D}_W(\mathbf{x})}{\operatorname{tr} \mathbb{D}_W(\mathbf{x})} \right) \tag{9.2}$$

for the tumor diffusion tensor as well as

$$\mathbf{u}(\mathbf{x}) = \frac{2s^2}{\lambda_0(n+2)} \left(\frac{\nabla \cdot \mathbb{D}_W(\mathbf{x})}{\operatorname{tr} \mathbb{D}_W(\mathbf{x})} - \frac{\mathbb{D}_W(\mathbf{x}) \cdot \nabla \operatorname{tr} \mathbb{D}_\mathbf{W}(\mathbf{x})}{(\operatorname{tr} \mathbb{D}_W(\mathbf{x}))^\mathbf{2}} \right) \tag{9.3}$$

for the tumor drift velocity. The function $g(Q)$ represents the influence of the receptor dynamics and is given by

$$g(Q(\mathbf{x})) = \lambda_1 (k^+ Q(\mathbf{x}) + k^- + \lambda_0)^{-1} f'(Q(\mathbf{x})). \tag{9.4}$$

In the following, simulations with and without the additional advection term resulting from the receptor dynamics will be compared. Figure 9.1 illustrates the numerical simulation of the evolution equation for cancer cells for the pure diffusive case, which have been performed on a horizontal brain slice and have been started with a binary distribution where a small initial tumor is located in the left hemisphere of the brain. Although we expected highly anisotropic diffusion there is no significant dependence on the direction visible. Obviously, the isotropic part of the tumor diffusion tensor dominates the anisotropic one and disables the emergence of anisotropic patterns. From viewpoint of biology it is thus questionable if diffusion is the dominating transport process in the

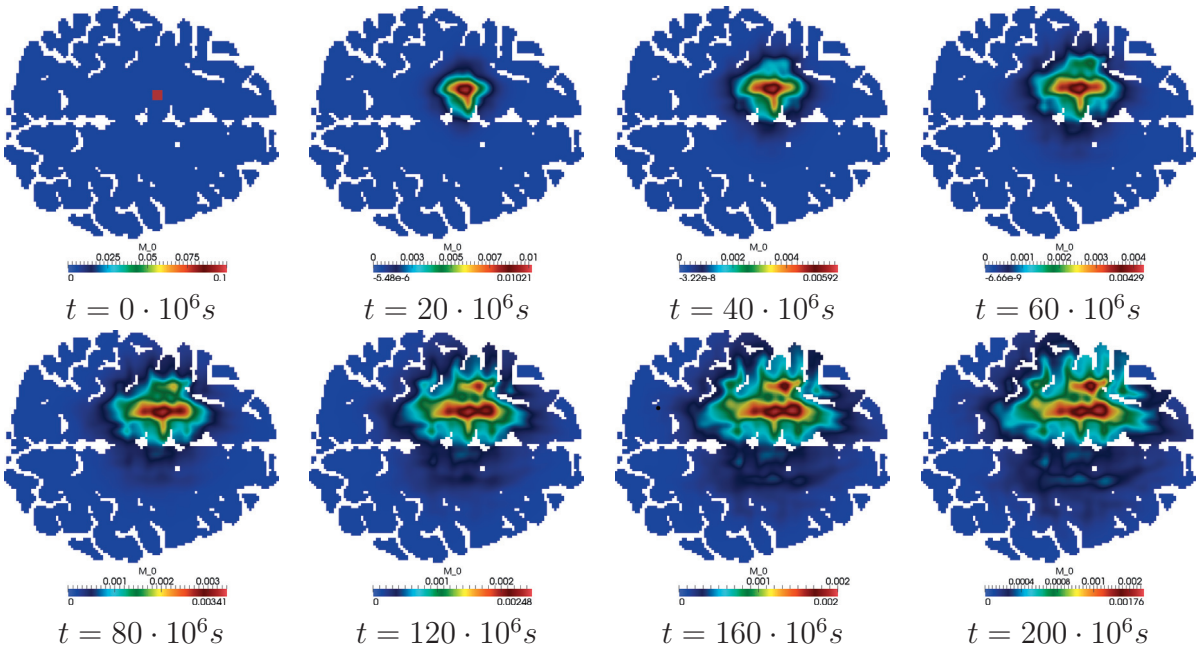

Figure 9.2.: Spread of cancer cells in the brain: advection dominated case (subcellular dynamics involved). For parameters see Table 8.1.

evolution of tumors. However, figure 9.1 shows some slight anisotropies, but these seem to be caused by the geometry of the simulation domain.

Figure 9.2 illustrates the simulation of the full system 9.1 including haptotactic drift. The emerging patterns show a high anisotropy caused by the haptotaxis term resulting from cell receptor dynamics. The sign of this additional drift term is converse to diffusion. While diffusion leads to a simple spread of the cells, haptotaxis pushes them into the white matter structure via a cellular binding process and generates the anisotropic pattern. The results differ significantly from diffusion dominated spread and the underlying tissue structure is visible. This observation supports the conjecture that directed cellular movement plays a crucial role in the cancer invasion processes, while diffusion seems to be of secondary interest. This makes sense from the biological point of view, since haptotactic and chemotactic movement of cells are assumed to be the major transport mechanisms on the cellular scale. As a consequence the question arises whether simple, classical diffusion-reaction models for cellular movement are justified in this context. We will return to this point later in the discussions.

9.1.2. Von Mises-Fisher distribution

Choosing a von Mises-Fisher distribution instead of the peanut for the distribution function q leads to different forms for the coefficients. The corresponding tumor diffusion

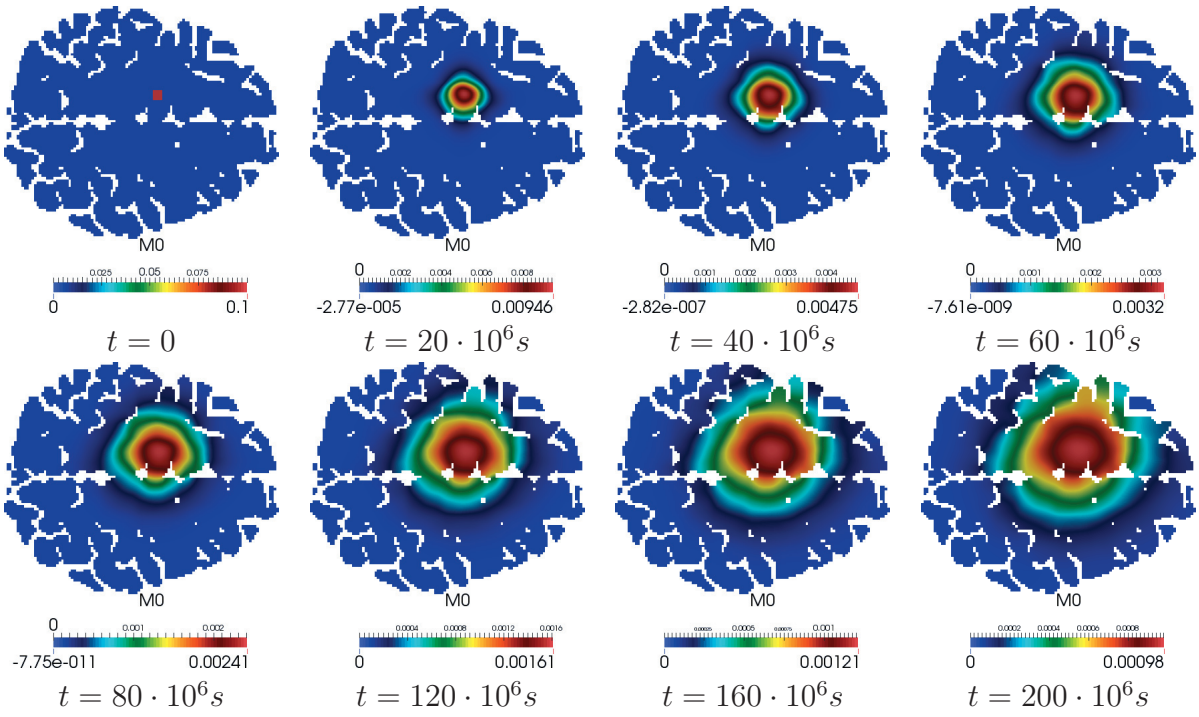

Figure 9.3.: Simulation of the evolution equation: case not involving subcellular dynamics with von Mises distribution with $\kappa = 10$ and $\delta = 0.05$.

tensor reads (Painter and Hillen, 2013)

$$\mathbb{D}_T(\mathbf{x}) = \frac{s^2}{3\lambda_0}\left[\left(\delta + (1-\delta)\left(\frac{\coth k}{k} - \frac{1}{k^2}\right)\right)\mathbb{I} + (1-\delta)\left(1 - \frac{3\coth k}{k} + \frac{3}{k^2}\right)\phi\phi^t\right], \tag{9.5}$$

with $k(\mathbf{x}) = \kappa \cdot \mathrm{FA}(\mathbf{x})$ and $\mathrm{FA}(\mathbf{x})$ denoting the fractional anisotropy index for each voxel. ϕ represents the leading eigenvector of the diffusion tensor for each voxel. κ can be interpreted as the sensitivity of the cells (Painter and Hillen, 2013) to the orientation of the underlying fibre structure and δ reflects the influence of stochastic effects. Figures 9.3-9.6 below show the evolution of the macroscopic equation (9.1) for the case $\kappa = 10$ and $\kappa = 20$ for both the pure diffusion case and the full system. Simulations have again been performed on a horizontal brain slice and have been started with a binary distribution where a small initial tumor is located in the left hemisphere of the brain as in the previous simulations. Figure 9.3 shows the results for the pure diffusion case for $\kappa = 10$, figure 9.4 shows the simulation for the corresponding full system including the advective terms. Additionally, simulations have been performed for $\kappa = 20$ in figures 9.5 and 9.6. As expected, the pure diffusive cases show higher anisotropies than the corresponding simulations based on the peanut distribution. This effect ist due to the artifical preference of the main direction of water diffusion within the von Mises-Fisher distribution. The larger κ ist chosen, the higher is the effect on the anisotropy.
However, simulation results for the corresponding full systems (figures 9.4 and 9.6) including the haptotactic drift term show the same qualitative behaviour as the simulations

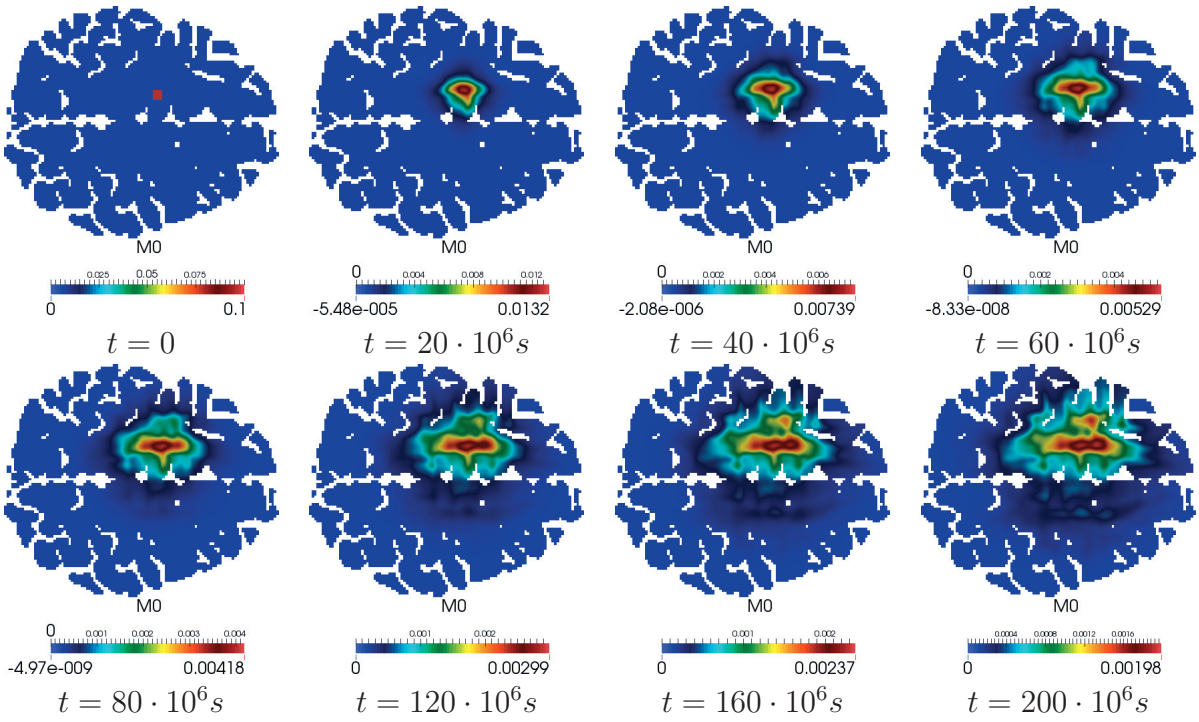

Figure 9.4.: Simulation of the evolution equation: case involving subcellular dynamics with von Mises distribution with $\kappa = 10$ and $\delta = 0.05$.

for the peanut distribution in figure 9.2. A detailed comparison of the form of the fibre distribution function will be presented in the next section.

9.1.3. Influence of the fibre distribution function

The choice of the fibre distribution function q involves diffusion tensor imaging data and determines the structure of the tumor diffusion tensor. As argued in section 5.4 the choice is not unique and the question arises how to mathematically relate $\mathbb{D}_W$ and q. As a first choice the *peanut* distribution

$$q(\mathbf{x}, \theta) = \frac{n}{|\mathbb{S}^{n-1}| \operatorname{tr} \mathbb{D}_W(\mathbf{x})} \theta^t \mathbb{D}_W(\mathbf{x}) \theta \tag{9.6}$$

has been proposed. In (Painter and Hillen, 2013) this choice has been criticised, and alternatively usage of a von Mises-Fisher distribution of the form

$$q(\mathbf{x}, \theta) = \frac{k(\mathbf{x})}{8\pi \sinh(k(\mathbf{x}))} \left(e^{k\phi \cdot \theta} + e^{-k\phi \cdot \theta} \right) \tag{9.7}$$

has been proposed with $k(\mathbf{x}) = \kappa \cdot \mathrm{FA}(\mathbf{x})$. Here, $\mathrm{FA}(\mathbf{x})$ denotes the fractional anisotropy index and the parameter κ can be interpreted as the sensitivity of the cells to the orientation of the underlying fibre structure.

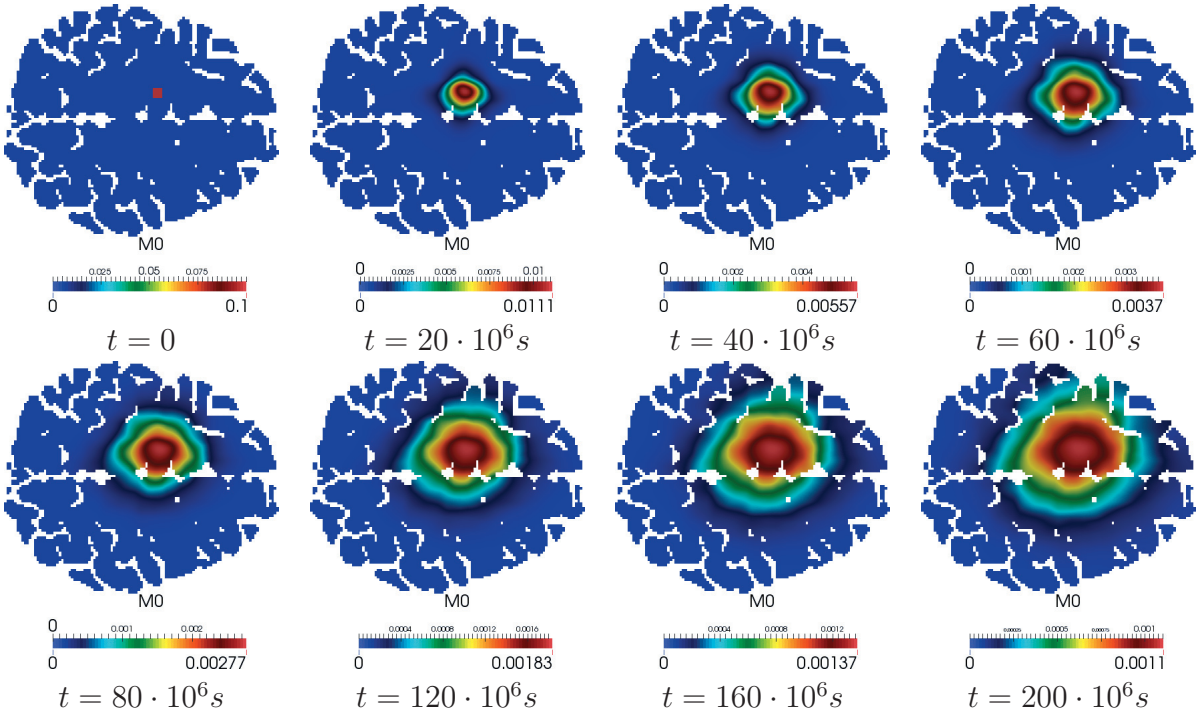

Figure 9.5.: Simulation of the evolution equation: case not involving subcellular dynamics with von Mises distribution with $\kappa = 20$ and $\delta = 0.05$.

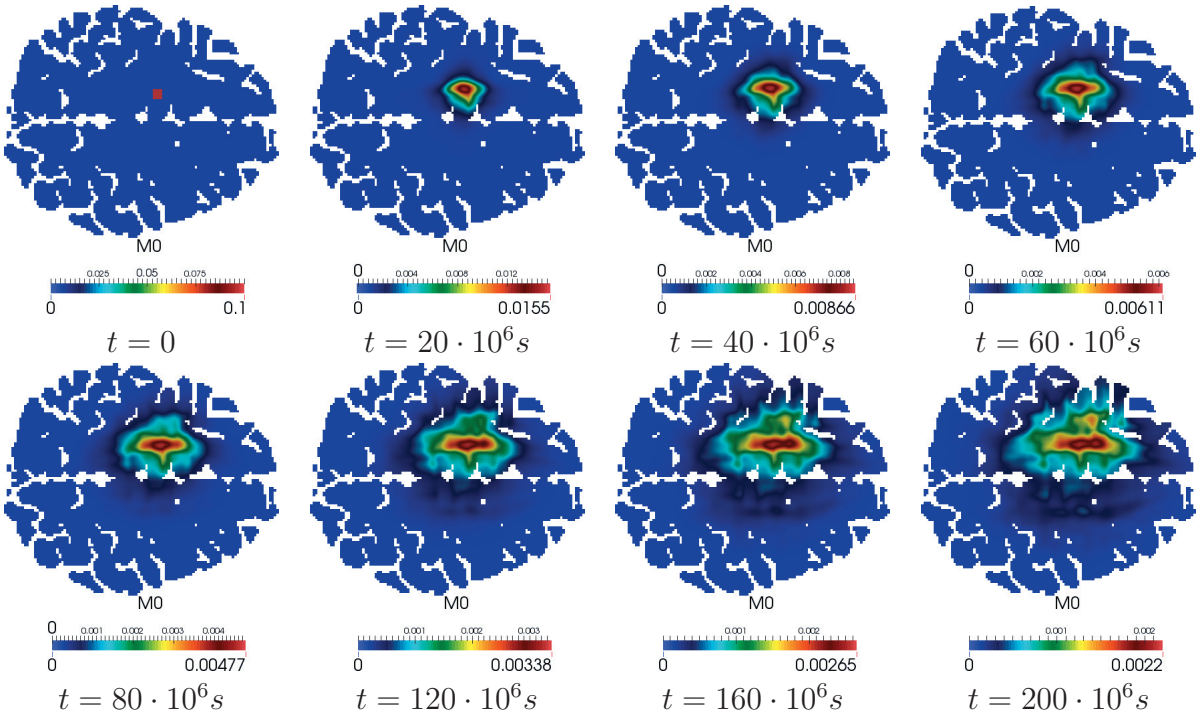

Figure 9.6.: Simulation of the evolution equation: case involving subcellular dynamics with von Mises distribution with $\kappa = 20$ and $\delta = 0.05$.

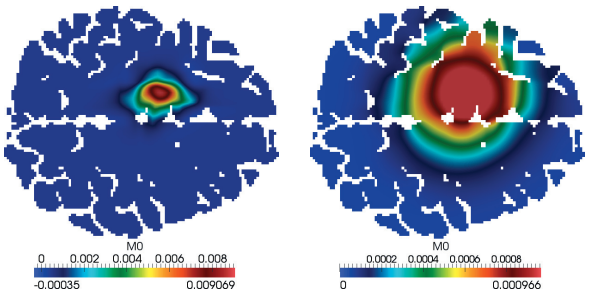

Figure 9.7.: Extreme cases of the von Mises-Fisher distribution for $\kappa \to \infty$ (left) and $\kappa \to 0$ (right).

Figure 9.8 shows simulation results of the tumor evolution at the endstep $t = 200 \cdot 10^6 s$ for the two suggested choices (5.18) and (5.19) for the fibre distribution function q. The upper row shows the results for the pure diffusive cases, the lower row the corresponding simulations including the haptotactic drift term.
As expected, an increased κ leads to a higher degree of anisotropy in the spread. Nevertheless, the results for the tumor evolution look quite similar when compared to each other. This suggests that the additional drift term resulting from the integrin dynamics predominantly causes the patterning effect, and the particular type of diffusion plays a minor role in generating anisotropic growth patterns.

In section 5.4 it has been shown that two limit tensors exist which reflect the minimal and maximal degree of anisotropy contained in the proposed distribution. This lead to the tensors

$$\mathbb{D}_T(\mathbf{x}) = \frac{s^2}{3\lambda_0}\left(\frac{1}{3} + \frac{2}{3}\delta\right)\mathbb{I}$$

and

$$\mathbb{D}_T(\mathbf{x}) = \frac{s^2}{3\lambda_0}\left(\delta\mathbb{I} + (1-\delta)\phi\phi^t\right).$$

Figure 9.7 shows the simulation end steps for both cases.

While the peanut distribution is parameter free and involves only values of the water diffusion tensor, the von Mises-Fisher distribution relies on an additional biological model parameter κ. Although its interpretation as cellular sensitivity seems intuitive, there is no biological data available and one has to rely on an educated guess for the choice. Furthermore, several other distributions are potential candidates, and there is little agreement which is the best choice at all. From this point of view it seems reasonable to keep the peanut distribution as a first choice for further calculations, as long as the relation between values of the water diffusion tensor and the choice of the distribution function has been investigated in detail. We will come back to these aspects in section 10.2, where we will discuss some ideas for future work.

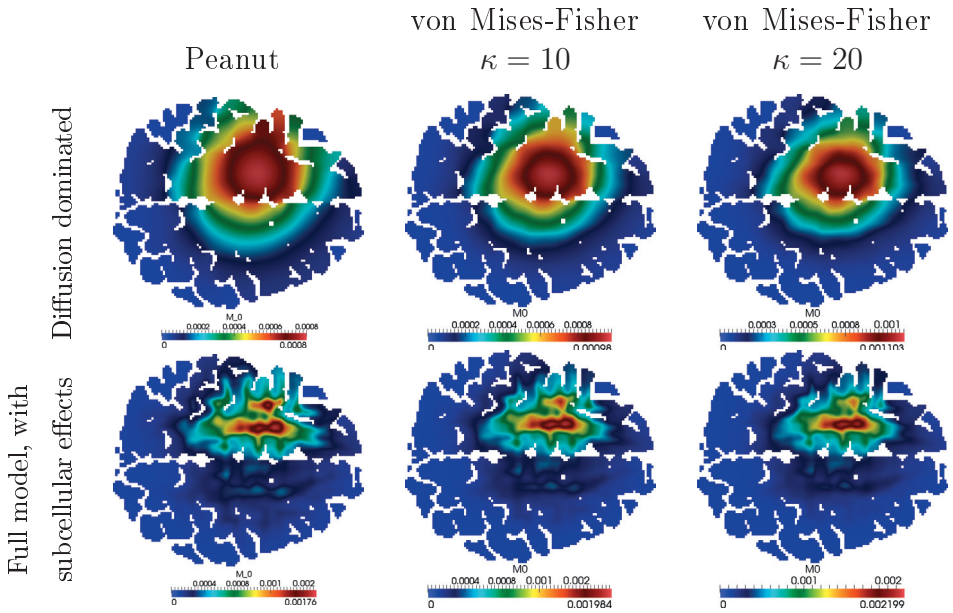

Figure 9.8.: Comparison of the spread of cancer cells in the brain for the peanut distribution and the bimodal von Mises-Fisher distribution at the endstep $t = 200 \cdot 10^6 s$. For the parameters see Table 8.1.

9.2. Simulation Results for the model including proliferation

In this section simulation results for the macroscopic evolution equation obtained in chapter 6.3 will be presented. Recall that the equation for the macroscopic cell density reads

$$\begin{aligned} \partial_t N_0 &= \nabla \cdot \left(\frac{1}{\lambda_0 + \alpha} \nabla \cdot (\mathbb{D}_T(\mathbf{x}) N_0) \right) \\ &\quad - \nabla \cdot \left(\frac{\lambda_1}{\lambda_0 + \alpha} h(\mathbf{x}) f'(Q) \mathbb{D}_T(\mathbf{x}) \cdot \nabla Q N_0 \right) = \frac{\alpha}{\alpha + \beta} g(N_0) N_0 - N_0 l(N_0), \end{aligned} \tag{9.8}$$

where the diffusion tensor is given by

$$\mathbb{D}_T(\mathbf{x}) = \frac{\beta}{\alpha + \beta} \frac{s^2}{\lambda_0 (n+2)} \left(\mathbb{I}_n + 2 \frac{\mathbb{D}_W(\mathbf{x})}{\operatorname{tr} \mathbb{D}_W(\mathbf{x})} \right). \tag{9.9}$$

It is still open to find appropriate terms for the gain and loss functions g and l. We assume that cellular proliferation behaves like logistic growth, and choose hence $g(N_0) = r_g$ to be constant for the proliferation rate $r_g \in \mathbb{R}^+$ and $l(N_0) = r_l N_0$ for $r_l \in \mathbb{R}^+$. Altogether this leads to the reaction term

$$\frac{\alpha}{\alpha + \beta} r_g N_0 - r_l N_0^2 = \left(\frac{\alpha}{\alpha + \beta} r_g - r_l N_0 \right) N_0.$$

Parameter	Interpretation	Value	Source
R_0	Number of receptors	10^5	(Belkin et al., 2005)
s	Cell speed	$10^{-6}\frac{\mathrm{m}}{\mathrm{s}}$	(Sidani et al., 2007)
λ_0	Turning rate	$0.1\frac{1}{\mathrm{s}}$	(Sidani et al., 2007)
λ_1	Deviation turning rate	$0.01\frac{1}{\mathrm{s}}$	estimated
k^+	Binding rate	$0.1\frac{1}{\mathrm{s}}$	estimated
k^-	Unbinding rate	$0.1\frac{1}{\mathrm{s}}$	(Lauffenburger and Lindermann, 1993)
α	Stopping rate	$10^{-2}\frac{1}{s}$	estimated
β	'Run again' rate	$10^{-2}\frac{1}{s}$	estimated
r_g	Proliferation rate	$10^{-5}\frac{1}{s}$	estimated
r_l	Cell death rate	$10^{-7}\frac{1}{s}$	estimated

Table 9.2.: Choice of parameters for the simulations.

Simulations of this model have been perfomed on a horizontal brain slice with a inital tumor placed in the left hemisphere. Figures 9.9 and 9.10 show simulations for the pure diffusion case and for the full system including haptotactic drift. Table 9.2 shows the paramter values chosen in the simulations.

As expected, proliferation causes sharper gradients compared to the advection-diffusion model without proliferative effects. The corresponding tumor growth patterns evolve faster than the patterns without proliferation because an increased amount of cells as cellular growth speeds up the diffusive spread. However, for the pure diffusion case the patterns do not differ significantly from the models without proliferation and again one cannot observe significant anisotropies caused by diffusion. Adding the haptotactic drift terms leads to branched structures, as figure 9.10 shows. Obviously, the tumor spreads predominatly in brain white matter and from the viewpoint of biology these finger-like patterns are quite more realistic than an isotropic spread. As in the previous section this is the expected result since the drift term acts contrary to diffusion and pushes the cells back into the anisotropic structure. Responsibe for this behaviour is, from the biological point of view, the increased gradients of Q near the interface regions between grey and white matter. In this regions the gradients are steep because of the transition, what is reflected by the fractional anisotropy index which is close to zero in grey matter and rapidly increases if it reaches anisotropic white matter zones.

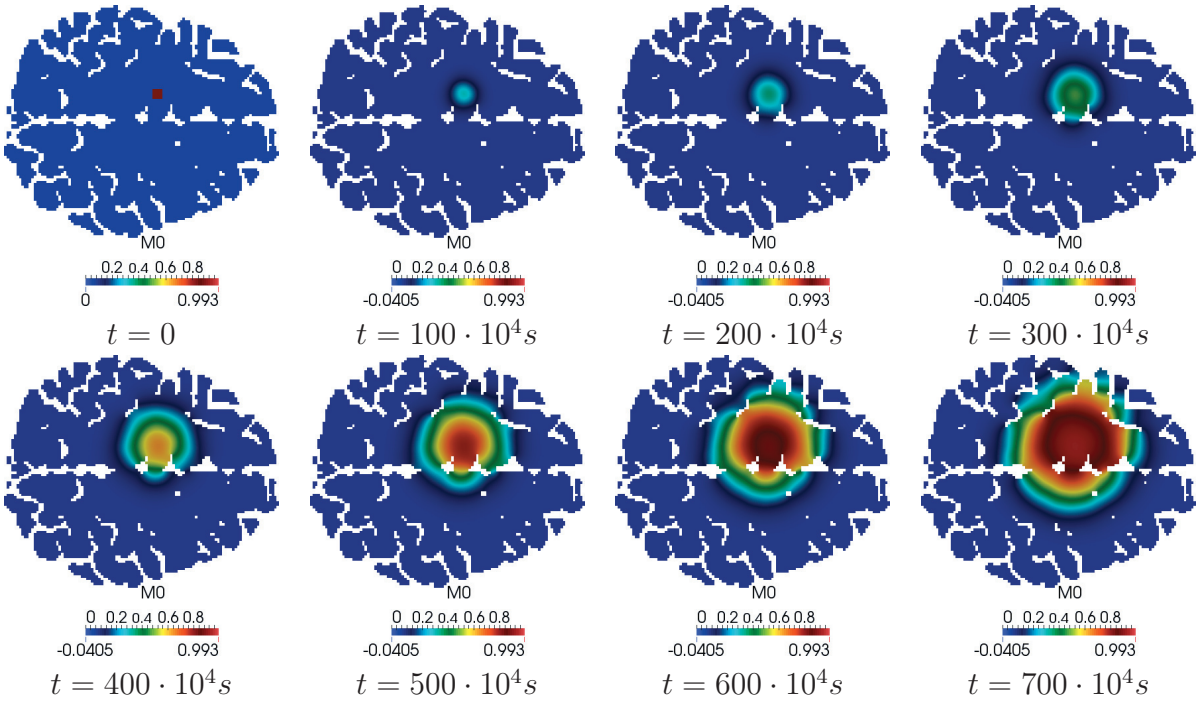

Figure 9.9.: Simulation of the evolution equation including prolferation: pure diffusive case.

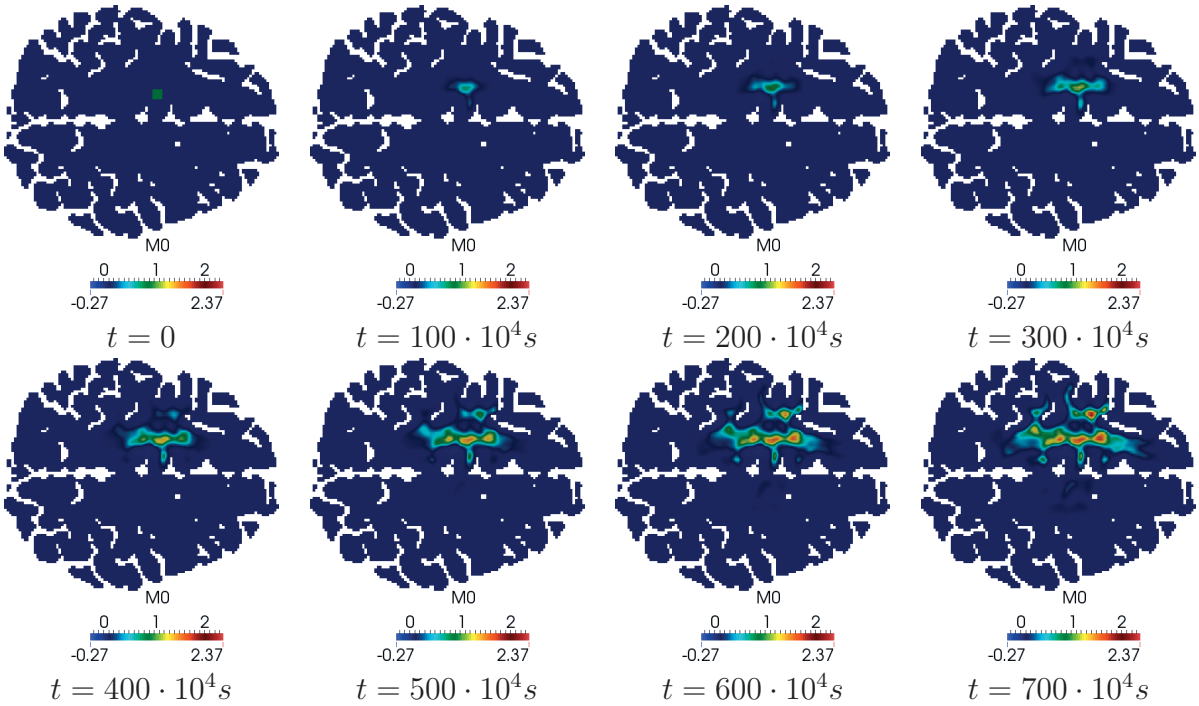

Figure 9.10.: Simulation of the evolution equation including prolferation: full system including haptotactic drift.

Part V.

Conclusion

10. Conclusion

I beat a brain tumor.

(Arlen Specter)

Contents

10.1. Discussion

10.1.1. General remarks

Brain tumors in general and particularly gliomas are not completely understood yet and offer a wide range of open questions. Interdisciplinary research has given a lot of meaningful insight during the last decades and especially mathematical multiscale modelling makes it possible to understand tumor growth and spread in greater detail. In this work a bottom up multiscale modelling approach has been proposed which starts with a model for binding processes of receptors on the cell surface on the microscale. Two models based on kinetic transport equations on the cell scale (mesoscale) describe the movement of cells in tissue networks. The first model in chapter 5 focuses on cellular movement itself while the second approach based on a *go or grow* mechanism in chapter 6 focusses on proliferative effects. Formal diffusion limits, obtained by parabolic scaling, lead to approximating macroscopic evolution equations for the macroscopic cell density. A special choice of the function q, as described in section 5.4, allows to take DTI data into account what makes patient specific modelling possible. For each voxel the coefficients can be evaluated depending on the values of the water diffusion tensor $\mathbb{D}_W$. Hence, one obtains personalized coefficients for the macroscopic evolution equations which take the patients' neural tissue structure into account. This is a great benefit compared to common models which do not use any specific data but provide tumor evolution equations on much simplified 'mathematical' domains.

10.1.2. Scaling limits

Macroscopic limit equations have been obtained in chapters 5 and 6. A challenging question was how to deal with the microscale variable which affects the system in two ways: first, via an additional drift term in the mesoscale description of the system and second

with respect to the dependence of the turning rate on this quantity. A momentum expansion with respect to the microscale variable made it possible to reduce the degrees of freedom and to focus on the $\mathbf{v}$ dependence to perform a formal parabolic scaling of the space and time variable. Sadly, this two-step approach makes rigorous results including error estimates for the approximation difficult to obtain.
The model in chapter 5 focusses on the influence of the cell receptor dynamics on the population behaviour and shows that it leads to haptotactic movement on the macroscale. The resulting evolution equations are of advection-diffusion type, where the coefficients contain the information from the micro- and mesoscale. The receptor binding model on the microscale leads to an additional drift term on the population level. Since we assumed that the cells' surface receptors bind to nonsoluble fibre stucture this corresponds to a haptotactic drift term causing directed movement of cells in direction of the gradient of binding substance.
The effect of cell growth and division has been studied in chapter 6. The model was based on a go or grow hypothesis allowing cells to either move or proliferate. The corresponding macroscopic model was of advection-diffusion-reaction type including a similar haptotaxis term as obtained in chapter 5 as well as a reaction term representing cell growth and death.
Both macroscopic evolution equations are of parabolic type. The existence of a solution for such equations is covered by theorem 4.1 in (Showalter, 1997), where existence has been shown for general nonlinear parabolic equations.

10.1.3. Simulation results

In chapter 9 simulations for the macroscopic equations illustrate their behaviour and their dependence on the data. Section 9.1 shows the behaviour of the advection-diffusion equation obtained in chapter 5.3. It comes out, that the additional transport term is crucial for the emergence of anisotropic patterns. Without this advective term the evolution is diffusion dominated and does not show any significant anisotropies, against first expectations. Obviously, diffusion and the haptotaxis term have different signs and can hence act in contrary directions. While diffusion seems to be responsible for the spread of the cells (for instance due to interspecific stress), the haptotactic terms lead to an active movement of the cells towards the gradient of aligned tissue. With respect to biological aspects because of two reasons. First, cells move easier through aligned networks because there is no need for frequent reorientation. This saves a lot of energy and leads to a faster movement. Second, the surface binding process is also easier in aligned tissue because of an enlarged directional persistence which leads also to a faster cellular movement.
Section 9.1.3 compares simulation results for two different choices of q. Obviously, the grade of anisotropy varies for different choices of q and is by trend larger in the case of a von Mises-Fisher distribution. This is not really remarkable, since the parameter κ artificially amplifies the grade of anisotropy. However, this effect is predominantly observable for the pure diffusive case and seems negligible if we add the haptotactic drift term. For the full system the anisotropies are mainly caused by the transport term and

not by anisotropic diffusion.
Chapter 9.2 contains simulation results for the equation including proliferation derived in section 6.3. Compared to the simulations without these effects, the growth speed of the tumor is increased significantly. A possible cause is the circumstance that proliferation sharpens the gradients which leads to an increased spread speed. The corresponding spread patterns have a finger like structure, show the expected anisotropic behaviour and can be related to the underlying fibre network. Glioma cells spread predominantly in anisotropic tissue areas with aligned fibre tracts which corresponds to the white matter areas in the brain. This biological hypothesis could also be observed in the simulations. Though, this is not surprising. The assumption that cells choose new directions corresponding to the underlying fibre network is the mathematical basis for this behaviour and is hence, in some sense, already contained in the modelling. However, from this point of view the anisotropy should have been caused by the diffusive part of the model equation, what was not the case at all. A key point for the emergence of patterns was the relation of Q to the fractional anisotropy index, which produced a haptotactic drift term becoming large in the interface regions of grey and white matter.

10.1.4. Model relevance and possibility of validation

Comparison of simulation results presented in this thesis with clinical data is desirable but not trivial because of several factors. First of all, medical imaging time series of glioma growth are usually not available. Diagnosis of a glioma happens usually due to symptoms as headache, vomiting and seizures emerging in a relatively late state. Once a glioma has been diagnosed, treatment strategies are initiated within relatively short time, including typically surgical resection. Models describing glioma growth in early stages can therefore not rely an appropriate clinical data. Second, imaging methods do not show the whole tumor with its infiltrative boundary but just core regions with a high progression in the destruction of healthy tissue. The proposed modelling is interested in the infiltrative boundary itself, which ist not directly visible. I will present some ideas for future work concerned with model validation in the next section.

10.2. Future work

In this section I present some ideas for future work. For the sake of clarity, I divided these issues in four categories. The first one is concerned with modelling aspects, the second one with the used data and their structure, the third one with mathematical analysis and the last one with validation.

10.2.1. Modelling

- **Tissue interaction**
  Neoplasms in the brain cause heavy mechanical deformations. The models studied in this thesis neglect this effect, but for future work it seems necessary to take

this effect into account. From the modelling perspective one should focus both on cell-cell interactions of glioma cells among themselves as well as the displacement of the neuronal structure by glioma cells. In the first case these effects have already been studied in (Chauviere et al., 2007), which can be seen as an extension of the M^5 paper (Hillen, 2006), where the authors derived a mechanical model including a physical stress tensor. In order to take also interactions with the underlying neuronal fibre network into account it seems interesting to couple the kinetic transport equation of moving glioma cells to an elasticity equation for the evolution of the neuronal fibre distribution q, describing the deformative evolution.

- **Turning rates**
  The turning rates in this work depend on a microscopic variable representing cell receptor occupancy. From the modelling viewpoint it could also be interesting to investigate the case for turning rates which depend on the local tissue density, since cells vary their reorientation rate depending on the surrounding tissue.

- **Proteases**
  It has been shown that several proteases play a crucial role in glioma invasion (Rao, 2003) since they work as chemoattractant for the tumor cells. Although this effect has been neglected in this work it has already been studied in more complex models in (Kelkel and Surulescu, 2011) and (Kelkel and Surulescu, 2012). Cell surface receptors can also be occupied by proteolytic rests which come from degredation of extracellular matrix components by glioma cells. An additional variable on the microscale can be used to model this binding process and probably this leads to another transport term on the macroscale which corresponds to a classic Keller-Segel chemotaxis term.

- **Therapy**
  As summarized in section 2.3, the three major treatment approaches for brain tumors are surgery, radiotherapy and chemotherapy. The effects of these therapy approaches could be studied within this modelling approach from a numerical perspective. For instance, setting the tumor cell concentration to zero within a specific part of the simulation domain and continuing the simulations would correspond to a surgical removal, reducing the concentration by a specific fraction could model the effects of radiotherapy.

10.2.2. Data

- **Relation of q and DTI data**
  The derivation of coefficients in the macroscopic evolution equations in sections 5.4 and 6.4 was based on the assumption that the apparent diffusion tensor and the neural fibre distribution function q can be related by a simple mathematical expression. This hypothesis is not validated at all, and as already explained in section 3.5 the field of tractography is concerned with this question. However, it is unclear which grade of exactness for this correlation is necessary for the class of

models used in this thesis. It would be interesting to find a minimal approximating expression in form of a mathematical distribution for the relation of DTI data and the orientation distribution function. While the peanut distribution (5.18) proposed in section 5.4 is the easiest educated guess and probably to simple, more specific distributions as the von Mises-Fisher class need additional parameters which are in many cases hard to derive from biological experiments.

- **High angular resolution diffusion imaging**
  A second point concerning the exactness of q is the fact that DTI data is based on a tensor model of diffusion, which has just six degrees of freedom. Neuronal fibre tracts can, however, have a complex structure within each voxel with multiple orientations. High angular resolution diffusion imaging methods make it possible to resolve fibre crossings within a single voxel in a greater detail since they measure the diffusion behaviour of water molecules for up to several hundred gradient directions. It would be interesing to study the influence of this more complex information on the model class used in this thesis.

10.2.3. Analysis

- **Rigorous limits**
  All scalings in this thesis have been performed formally without rigorous estimates. It is desirable to obtain rigorous error estimates in order to gain information on the goodness of the approximation.

- **Turning kernel**
  The turning behaviour of the cells is assumed to be independent of the local cell density, which leads to linear turning operators which have intensively been studied. In fact, the turning behaviour of cells is influenced by the numbers, respectively the density of sourrunding cells. This could be introduced into the models by turning kernels which depend on the cell density. This leads to nonlinear turning operators which need new mathematical instruments.

10.2.4. Validation

- **Biological experiments for cellular movement**
  In this thesis it has been shown that cellular binding processes on the microscale lead to drift dominated movement of cell populations on the macroscale. It would be a great benefit for this class of multiscale models if this behaviour could be validated in biological experiments. For this purpose a cooperation project has been initiated, where cellular movement on directed collagen substrate will be studied. One of the main goals of the project is to validate if receptor binding processes are responsible for drift dominated movement. Knock-down experiments, which disable most of a cells' surface receptors, will hopefully clarify this question.

- **Comparison with clinical studies**
  Although I already argued that comparison with clinical data seems to be hard, there are some possible approaches for a validation from my point of view. Usually, there is no early stage data of gliomas, but with appropriate initial conditions it would be possible to perform simulations from any stadium of the tumor. These appropriate initial conditions could possibly be found in T1 pictures, where the intensity indicates the type of tissue within the brain. As a first step one could correlate the intensity of such a T1 picture to a corresponding initial tumor concentration for each voxel, and then perform the simulations.
  Furthermore, it is clear that the simulation results do not correspond one-to-one to the real tumors, because most of the invasive boundary shown in the simulations is not visible on T1 pictures.

Bibliography

L. Abrey. *Fast Facts: Brain Tumors*. Health Press, 2011.

W. Alt. Biased random walk models for chemotaxis and related diffusion approximations. *Journal of Mathematical Biology*, 9:147–177, 1980.

W. Alt. Singular perturbation of differential integral equations describing biased random walks. *Journal für Reine und Angewandte Mathematik*, 322:15–41, 1981.

D. N. Arnold, F. Brezzi, B. Cockburn, and L.D. Marini. Unified Analysis of Discontinuous Galerkin Methods for Elliptic Problems. *SIAM Journal on Numerical Analysis*, 39(5):1749–1779, 2002.

M. Aubert, M. Badoual, S. Fereol, C. Christov, and B. Grammaticos. A cellular automaton model for the migration of glioma cells. *Physical Biology*, 3(2):93–100, 2006.

P. Basser, J. Matielleo, and D. LeBihan. Diagonal and off-diagonal components of the self-diffusion tensor: their relation to and estimation from the NMR spin-echo signal. *11th Society of Magnetic Resonance in Medicine Meeting*, 1222, 1992.

P. Basser, J. Matiello, R. Turner, and D. LeBihan. Diffusion tensor echo-planar imaging of human brain. *Proceedings of the SMRM*, 584, 1993.

P. Bastian, M. Blatt, A. Dedner, C. Engwer, R. Klöfkorn, R. Kornhuber, M. Ohlberger, and O. Sander. A generic grid interface for parallel and adaptive scientific computing. Part II: Implementation and tests in DUNE. *Computing*, 82(2–3):121–138, 7 2008. doi: 10.1007/s00607-008-0004-9.

A.M. Belkin, G. Tsurupa, E. Zemskov, Y. Veklich, J.W. Weisel, and L. Medved. Transglutaminase-mediated oligomerization of the fibrin(ogen) αC domains promotes integrin-dependent cell adhesion and signaling. *Blood*, 105(9):3561–3568, 2005.

N. Bellomo. *Towards a Mathematical Theory of Complex Biological Systems*. Birkhäuser, 2008.

N. Bellomo and C. Bianca. *Modelling Complex Living Systems*. World Scientific, 2011.

T. Beppu, T. Inoue, Y. Shibata, A. Kurose, H. Arai, K. Ogasawara, A. Ogawa, S. Nakamura, and H. Kabasawa. Measurement of fractional anisotropy using diffuson tensor MRI in supratentorial astrocytic tumors. *Journal of Neuro-Oncology*, 63:109–116, 2003.

J. A. Berube and M. Dessureault. Morphological characterization of armillaria ostoyae and armillaria sinapina sp.nov. *Canadian Journal of Botany*, 66(10):2027–2034, 1988.

D.K. Binder and M.S. Berger. Proteases and the biology of glioma invasion. *Journal of Neuro-Oncology*, 56:149–158, 2002.

H. Blumenfeld. *Neuroanatomy through Clinical Cases*. Palgrave Macmillan, 2010.

P.Y. Bondiau, O. Clatz, M. Sermesant, P.Y. Marcy, H. Delingette, M. Frenay, and N. Ayache. Biocomputing: numerical simulation of glioblastoma growth using diffusion tensor imaging. *Physics in Medicine and Biology*, 53:879–893, 2008.

A. Caccone, G. Gentile, T.H. Gibbs, J.P.and Fritts, H.L. Snell, J. Betts, and J. Powell. Phylogeography and history of the giant galapagos tortoises. *Evolution*, 56(10):2052–2066, 2002.

F. Chalub, P.A. Markovich, B. Perthame, and C. Schmeiser. Kinetic models for chemotaxis and their drift-diffusion limits. *Monatshefte für Mathematik*, 142(1-2):123–141, 2004a.

F. Chalub, P. Markowich, B. Perthame, and C. Schmeiser. Kinetic models for chemotaxis and their drift-diffusion limits. *Monatshefte für Mathematik*, 141(1):123–141, 2004b.

A. Chauviere, T. Hillen, and L. Preziosi. Modeling cell movement in anisotropic and heterogeneous network tissues. *Networks heterogeneous media*, 2:333–357, 2007.

O. Clatz, M. Sermesant, P.Y. Bondiau, H. Delignette, S.K. Warfield, G. Malandain, and N. Ayache. Realistic simulation of the 3D growth of brain tumors in MRI images coupling diffusion with biomechanical deformation. *IEEE Trans. Med. Imag.*, 24(10): 1334–1346, 2005.

G.C. Cruywagen, D.E. Woodward, P. Tracqui, G.T. Bartoo, J.D. Murray, and E.C. Alvord. The modeling of diffusive brain tumours. *Journal of Biological Systems*, 3(4): 937–945, 1995.

L.M. DeAngelis. Brain tumors. *The New Englad Journal of Medicine*, 344(114–123), 2001.

T.S. Deisboeck and G.S. Stamatakos. *Multiscale Cancer Modeling.* Chapman & Hall, 2010.

T. Demuth and M.E. Berens. Molecular mechanisms of glioma cell invasion and migration. *Journal of Neuro-Oncology*, 70:217–228, 2004.

M. Descoteaux. *High Angular Resolution Diffusion MRI:from Local Estimation to Segmentation and Tractography.* Ph.D. thesis, Université Nice-Sophia Antipolis, 2008.

M. Descoteaux, R. Deriche, T. Knische, and A. Anwander. Deterministic and probabilistic tractography based on complex fibre orientation distribution. *IEEE Transactions of Medical Imaging*, 28(2):269–286, 2009.

J.S. Desgrosellier and D.A. Cheresh. Integrins and cancer:biological implications and therapeutic opportunities. *Nature Reviews Cancer*, 10:9–23, 2010.

A. Deutsch and S. Dormann. *Cellular Automaton Modeling of Biological Pattern Formation.* Birkhauser, 2005.

Y. Dolak and C. Schmeiser. Kinetic models for chemotaxis: Hydrodynamic limits and spatio-temporal mechanisms. *Journal of Mathematical Biology*, 51(6):595–615, 2005.

C. Engwer, T. Hillen, Knappitsch M., and Surulescu C. A DTI-based multiscale model for glioma spread including cell-ECM interactions. *submitted*, 2013.

R. Erban and H. Othmer. From signal transduction to spatial pattern formation in *e. coli*: a paradigm for multiscale modeling in biology. *Multiscale Modeling and Simulation*, 3(2):362–394, 2005a.

R. Erban and H. Othmer. From individual to collective behaviour in bacterial chemotaxis. *SIAM Journal for applied mathematics*, 65(2):361–391, 2005b.

A. Ern, A.F. Stephansen, and P. Zunino. A discontinuous galerkin method with weighted averages for advection-diffusion equations with locally small and anisotropic diffusivity. *IMA Journal of Numerical Analysis*, 29(2):235–256, 2009. doi: 10.1093/imanum/drm050.

J.C. Fernandez-Miranda, S. Pathak, J. Engh, K. Jarbo, T. Verstynen, F.-C. Yeh, Y. Wang, A. Mitz, F. Boada, W. Schneider, and R. Friedlander. High-definition fiber tractography of the human brain: Neuroanatomical validation and neurosurgical applications. *Neurosurgery*, 71:430–453, 2012.

P. Friedl and E.B. Broecker. The biology of cell locomotion within three-dimensional extracellular matrix. *Cellular and Molecular Life Sciences*, 57(41–64), 2000.

D.H. Geho, R.W. Bandle, T. Clair, and L.A. Liotta. Physiological mechanisms of tumor-cell invasion and migration. *Physiology*, 20:194–200, 2005.

A. Giese and M. Westphal. Glioma invasion in the central nervous system. *Neurosurgery*, 39:235–252, 1996.

A. Giese, R. Bjerkvig, R. Berens, and M. Westphal. Cost of migration: invasion of malignant gliomas and implications for treatment. *Journal for Clinical oncology*, 21: 1624–1636, 2003.

R.H. Goldbrunner, J.J. Bernstein, and J.-C. Tonn. Cell-extracellular matrix interaction in glioma invasion. *Acta Neurochirurgica*, 141(2):97–109, 1999.

Grünbaum. Advection-diffusion equations for internal state-mediated random walks. *SIAM Journal for Applied Mathemtics.*, 61:43–73, 2000.

P. Hagman, L. Jonasson, P. Maeder, J.-P. Thiran, V.J. Wedeen, and R. Mueli. Understanding diffusion mr imaging techniques: From scalar diffusion-weightred imaging to diffusion tensor imaging and beyond. *RadioGraphics*, 26:205–223, 2006.

D. Hanahan and R.A. Weinberg. Hallmarks of cancer: the next generation. *Cell*, 144 (4):646–674, 2011.

H. Hatzikirou, A. Deutsch, K. Schaller, M. Simon, and K. Swanson. Mathematical modelling of glioblastoma tumor development: a review. *Mathematical Models and Methods in Applied Sciences*, 15(11):1779–1794, 2005.

H. Hatzikirou, D. Basanta, M. Simon, K. Schaller, and A. Deutsch. Go or grow: the key to the emergence of invasion in tumor progression? *Mathematical medicine and biology*, 29:49–65, 2012.

T. Hillen. Transport equations with resting phases. *European Journal of Applied Mathematics*, 14:613–636, 2003.

T. Hillen. On the L^2-moment closure of transport equations: the general case. *Discrete and Continuous Dynamical Systems - Series B*, 5(2):299–318, 2005.

T. Hillen. M^5 mesoscopic and macroscopic models for mesenchymal motion. *Journal of Mathematical Biology*, 53:585–616, 2006.

T. Hillen and H. Othmer. The diffusion limit of transport equations derived from velocity jump processes. *SIAM Journal on Applied Mathematics*, 61(3):751–775, 2000.

T. Hillen and K.J. Painter. Transport and anisotropic diffusion models for movement in oriented habitats. *In:Lewis,M.,Maini,P.,Petrovskii,S. (Eds.), Dispersal, Individual Movement and Spatial Ecology: A Mathematical Perspective. Springer,Heidelberg.*, 2013.

R. Hynes. Integrins: bidirectional, allosteric signaling machines. *Cell*, 110:673–687, 2002.

S. Jbabdi, E. Mandonnet, H. Duffau, L. Capelle, K.R. Swanson, M. Pelegrini-Isaac, R. Guillevin, and H. Benali. Simulation of anisotropic growth of low-grad gliomas using diffusion tensor imaging. *Magnetic Resonance in Medicine*, 54:616–624, 2005.

B.J. Jellison, A.S. Field, J. Medow, M. Lazar, M.S. Salamat, and A.L. Alexander. Diffusion tensor imaging of cerebral white matter: A pictorial review of physics, fiber tract anatomy, and tumor imaging patterns. *American Journal of Neuroradiology*, 25: 356–369, 2004.

S.H. Kaufmann and W.C. Earnshaw. Induction of apoptosis by cancer chemotherapy. *Experimental Cell Research*, 256(1):42–49, 2000.

J. Kelkel and C. Surulescu. On some models for cancer cell migration through tissue networks. *Mathematical Biosciences and Engineering*, 8(2):575–589, 2011.

J. Kelkel and C. Surulescu. A multiscale approach to cell migration in tissue networks. *Mathematical Models and Methods in Applied Sciences*, 23(3), 2012.

G. Kindlmann and C.F. Westin. Diffusion tensor visualization with glyph packing. *IEEE TRANSACTIONS ON VISUALIZATION AND COMPUTER GRAPHICS*, 12 (5):1329–1336, 2006.

E. Konukoglu, O. Clatz, P.Y. Bondiau, H. Delignette, and N. Ayache. Extrapolation glioma invasion margin in brain magnetic resonance images: Suggesting new irradiation margins. *Medical Image Analysis*, 14:111–125, 2010.

N. Laperriere, L. Zuraw, and G. Cairncross. Radiotherapy for newly diagnosed malignant glioma in adults: a systematic review. *Radiotherapy & Oncology*, 64:259–273, 2002.

D.A. Lauffenburger and J.L. Lindermann. *Receptors. Models for binding, trafficing and signaling.* Oxford University Press, 1993.

D. LeBihan, E. Breton, D. Lallemand, P. Grenier, E. Cabanis, and M.L. Jeanet. Mr imaging on intravoxel incoherent motions: application to diffusion and perfusion in neurologic disorders. *Radiology*, 61:401–407, 1986.

C. Lenglet, J.S.W. Campbell, M. Descoteaux, G. Haro, P. Savadjiev, D. Wassermann, A. Anwander, G.B. Pike, K. Sapiro, and P.M. Thompson. Mathematical methods for diffusion MRI processing. *Neuroimage*, 45:111–122, 2009.

T. Lorenz and C. Surulescu. On a class of multiscale cancer migration models: Well-posedness in less regular function spaces. *Mathematical Models and Methods in Applied Sciences*, 24(10), 2014.

V. Cristini & J. Lowengrub. *Multiscale Modeling of Cancer: An Integrated Experimental and Mathematical Modeling Approach.* Cambridge University Press, 2010.

L. Marner, J.R. Nyengaard, Y. Tang, and B. Pakkenberg. Marked loss of myelinated nerve fibers in the human brain with age. *The Journal of comparative neurology*, 462 (2):144–152, 2003.

J. Matiello and D. LeBihan. Estimation of the effective self-diffusion tensor from the NMR spin echo. *Journal of Magnetic Resonance*, 103:247–254, 1994a.

J. Matiello and D. LeBihan. Mr diffusion tensor spectroscopy and imaging. *Biophysical Journal*, 66(1):259–267, 1994b.

G. Moore, B. Kershner, Craig T., Daniel M., Gil N., R. Spellenberg, J.W. Thieret, Terry P., and A. Block. *National Wildlife Federation Field Guide to Trees of North America*. New York Press, 2008.

S.J. Moschos, L.M. Drogowski, S.I. Reppert, and J.M. Kirkwood. Integrins and cancer. *Oncology*, 21(9):13–20, 2007.

M. Moseley, J. Kucharczyk, Y. Cohen, J. Mitorovitch, H.S. Asgari, M.F. Wendland, J. Tsuruda, and D. Norman. Diffusion-weighted mr imaging of anisotropic water diffusion in cat central nervous system. *Radiology*, 172(2):439–450, 1990.

H. Ohgaki and P. Kleihues. Epidemiology end etiology of gliomas. *Acta Neuropathologica*, 109:93–108, 2005.

H.G. Othmer and T. Hillen. The diffusion limit of transport equations ii: Chemotaxis equations. *SIAM Journal for Applied Mathematics*, 62:1222–1250, 2002.

H.G. Othmer, S.R. Dunbar, and W. Alt. Models of dispersal in biological systems. *Journal of Mathematical Biology*, 26:263–298, 1988.

K.J. Painter and T. Hillen. Mathematical modelling of glioma growth: the use of diffusion tensor imaging (DTI) data to predict the anisotropic pathways of cancer invasion. *J. Theoretical Biol.*, 323:25–39, 2013.

B.J. Park, H.K. Kim, B. Sade, and J.H. Lee. *Meningiomas: Diagnosis, Treatment, and Outcome.* Springer, 2009.

C.S. Patlak. Random walk with persistence and external bias. *Bulletin of Mathematical Biophysics*, 15:311–338, 1953.

C. Pierpaoli and P.J. Basser. Toward a quantitative assessment of diffusion anisotropy. *Magnetic Resonance in Medicine*, 36(6):893–906, 1996.

M.C. Preul. History of brain tumor surgery. *Journal of Neurosurgery*, 18(4):1–1, 2005.

J.S. Rao. Molecular mechanisms of glioma invasiveness: the role of proteases. *Nature Reviews Cancer*, 3:489–501, 2003.

R.E. Showalter. *Monotone Operators in Banach Spaces and Nonlinear Partial Differential Equations.* American Mathematical Society, 1997.

M. Sidani, D. Wessels, G. Mouneimne, M. Ghosh, S. Goswami, C. Sarmiento, W. Wang, S. Kuhl, M. El-Sibai, J.M. Backer, R. Eddy, D. Soll, and J. Condeelis. Cofilin determines the migration behavior and turning frequency of metastatic cancer cells. *The Journal of Cell Biology*, 179(4):777–791, 2007.

R. Stupp, W.P. Mason, M.J. Van den Bent, M. Weller, B. Fisher, M.J. Taphoorn, K. Belanger, A.A. Brandes, C. Marosi, U. Bogdahn, J. Curschmann, R.C. Janzer, S.K. Ludwin, T. Gorlia, A. Allgeier, D. Lacombe, J.G. Cairncross, E. Eisenhauer, and R.O. Mirimanoff. Radiotherapy plus concomitant and adjuvant temozolomide for glioblastoma. *New England Journal of medicine*, 352:987–996, 2005.

C. Suarez, F. Maglietti, M. Colonna, K. Breitburd, and G. Marshall. Mathematical modeling of human glioma growth based on brain topological structures: Study of two clinical cases. *Mathematical Models and Methods in Applied Sciences*, 7(6):1–11, 2012.

P.C. Sundgren, Q. Dong, D. Gomez-Hassan, S.K. Mukherji, P. Maly, and R. Welsh. Diffusion tensor imaging of the brain: review of clinical applications. *Neurocarciology*, 46:339–350, 2004.

K.R. Swanson. *Mathematical modelling of growth and control of tumors*. PhD thesis, University of Washington, 1999.

K.R. Swanson, E. Alvord, and J.D. Murray. A quantitative model for differential motility of gliomas in grey and white matter. *Cell Proliferation*, 33:317–329, 2000.

K.R. Swanson, C. Bridge, J.D: Murray, C. Ellsworth, and J. Alvord. Virtual and real brain tumors: using mathematical modelling to quantify glioma growth and invasion. *Journal of the Neurological Sciences*, 216:1–10, 2003.

P. Tracqui. From passive diffusion to active cellular migration in mathematical models of tumour invasion. *Acta Biotheoretica*, 43:443–464, 1995.

P. Tracqui, G.C. Cruywagen, D.E. Woodward, G.T. Bartoo, J.D. Murray, and E.C. Alvord. A mathematical model of glioma growth: the effect of chemotherapy on spatio-temporal growth. *Proliferation*, 28:17–31, 1995.

D.S. Tuch. *Diffusion MRI of complex Tissue Structure.* Ph.D. thesis, University of Chicago, 1996.

D.S. Tuch. Q-ball imaging. *Magnetic resonance in Medicine*, 52(6):1358–1372, 2004.

D.S. Tuch, T.G. Reese, M.R. Wiegell, and V.J. Wedeen. Diffusion MRI of complex neural architecture. *Neuron*, 40:885–895, 2003.

T. Visted, P.O. Enger, M. Lund-Johansen, and R. Bjerkvig. Mechanisms of tumor cell invasion and angiogenesis in the central nervous system. *Frontiers in Biosciences*, 8: 289–304, 2003.

Y. Wang and T. Jiang. Understanding high grade glioma: molecular mechanism, therapy and comprehensive management. *Cancer letters*, 331:139–146, 2013.

M.L. Ware, M.S. Berger, and D.K. Binder. Molecular biology of glioma tumorgenesis. *Histology and Histopathology*, 18:207–216, 2003.

G.E. Wesbey, M. Moseley, and R. Ehmann. Translational molecular self-diffusion in magenitc resonance imaging. i. effects on observed spin-spin relaxation. *Inverstigative Radiology*, 19:484–490, 1984a.

G.E. Wesbey, M. Moseley, and R. Ehmann. Translational molecular self-diffusion in magenitc resonance imaging. ii. measurement of the self-diffusion coefficient. *Inverstigative Radiology*, 19:491–498, 1984b.

Mary Fanett Wheeler. An Elliptic Collocation-Finite Element Method with Interior Penalties. *SIAM Journal on Numerical Analysis*, 15(1):152–161, 1978.

M. Wrensch, Y. Minn, T. Chew, M. Bondy, and M.S. Berger. Epidemiology of primary brain tumors: Current concepts and review of the literature. *Neuro-Oncology*, 4(4): 278–299, 2002.

C. Xue and H. Othmer. Multiscale models of taxis driven patterning in bacterial populations. *SIAM Journal for Applied Mathematics*, 70(1):133–169, 2009.

List of Figures

Index